Graduate Theses and Dissertations   Graduate School

3-22-2017

Effects of Microstructure and Alloy Concentration on the Corrosion and Tribocorrosion Resistance of Al-Mn and WE43 Mg Alloys

Hesham Y. Saleh Mraied
University of South Florida, hesham@mail.usf.edu

Effects of Microstructure and Alloy Concentration on the Corrosion and Tribocorrosion

Resistance of Al-Mn and WE43 Mg Alloys

by

Hesham Mraied

A dissertation submitted in partial fulfillment
of the requirements for the degree of
Doctor of Philosophy in Mechanical Engineering
Department of Mechanical Engineering
College of Engineering
University of South Florida

Major Professor: Wenjun Cai, Ph.D.
Delcie Durham, Ph.D.
Nathan Crane, Ph.D.
Alberto Sagüés, Ph.D.
Shengqian Ma, Ph.D.

Date of Approval:
March 8, 2017

Keywords: Aluminum alloy, Magnesium alloy, PVD, EIS, SEM

DEDICATION

This work is dedicated to my parents, Dalal Benslimane and Youssef Mraied, for their sacrifices and believing in me. To my best friend and beloved wife, Asma Sharfeddin, for her support and encouragement. To my beautiful children, Abdulmajid, Maryam, and Aamena, the joy of this journey.

ACKNOWLEDGMENTS

TABLE OF CONTENTS

LIST OF TABLES

LIST OF FIGURES

ABSTRACT

The design of new engineering materials resistant to both wear damage and corrosion degradation becomes increasingly demanding in complex service conditions. Unfortunately, there is typically a tradeoff between wear and corrosion resistance, even for important passive metals such as Al alloys. This is because the presence of precipitates hardens the material but at the same time lead to unfavorable galvanic coupling between the precipitates and the matrix, resulting in accelerated corrosion. This work showed that Al (or Mg) supersaturated solid solution formed using non-equilibrium methods exhibited enhanced corrosion resistance without compromising strength. For Al, alloying with Mn up to ~ 20.at.% simultaneously increased the wear resistance of Al as well as the protectiveness of the passive layer, thus improving the overall tribocorrosion resistance. For Mg, alloying with Y (4.67 wt.%), Zr (0.45 wt%), and Nd (1.79 wt%) in solid solution led to ~ 8 fold increment in corrosion resistance in physiological environment.

Magnetron-sputtered aluminum (Al) and aluminum–manganese (Al-Mn) films with structures ranging from nanocrystalline to amorphous were obtained by tuning the Mn% up to 20.5 at.%. Corrosion behavior of the films was investigated in 0.6 M and 0.01 M NaCl aqueous solutions by potentiodynamic polarization (PD) and electrochemical impedance spectroscopy (EIS). Pitting corrosion was found to be strongly affected by alloy composition. The amorphous Al–20.5 at.% Mn exhibited the best pitting resistance during short term exposure. However, over longer immersion in 0.01 M NaCl up to 108 hrs, nanocrystalline Al–5.2 at.% Mn showed the

highest corrosion resistance. The dual-phase Al-11.5 at % Mn alloy was found to have higher nominal corrosion rate compared to its nanocrystalline or amorphous counterparts.

The effects of Mn alloying on the tribocorrosion behavior of magnetron-sputtered Al-Mn thin films with 5.2 at.% and 20.5 at.% Mn were investigated in 0.6 M NaCl aqueous solution. Tribocorrosion resistance of Al-Mn was found to be strongly affected by the alloying composition and applied potential. Higher Mn content increased H/E ratio and promoted the formation of denser and more compact passive film, hence improving tribocorrosion resistance of Al. In particular, alloying with 20.5 at.% Mn led to an increase of the corrosion resistance by ~ 10 times and the hardness ~ 8 times compared to pure Al. The total material loss during tribocorrosion was found to increase with applied potential. When the applied potential was increased from cathodic to anodic, simultaneous contribution of the mechanical and the electrochemical wear leads to accelerated material loss. A galvanic cell model was used to investigate the depassivation-repassivation kinetics during tribocorrosion. It was found that alloying with 5.2 at.% Mn led to more than 10-fold reduction in the current density required to re-passivate similar worn areas compared to pure Al. The origin of wear-corrosion synergy was discussed based on these observations.

Magnesium alloys such as WE43 are considered for biomedical applications including cardiovascular stents and bone implants due to their biocompatibility, good cell adhesion, and mechanical properties close to that of bones. Unfortunately, their high degradation rate and subsequent loss of structural integrity in physiological environments hinders such applications. To improve the corrosion resistance of WE43 magnesium alloy, its microstructure was optimized to prevent micro-galvanic coupling between Mg matrix and precipitates. Chemically homogeneous WE43 with nanoscale surface roughness was obtained by magnetron sputtering

with high effective quench rate. The effect of chemical heterogeneity on the corrosion resistance of biodegradable WE43 magnesium alloy was studied by performing corrosion tests in blood bank buffered saline using samples from two metallurgical states, cast and deposited. The microstructure of all samples was investigated by grazing incidence X-ray diffraction (XRD), scanning electron microscopy (SEM), and transmission electron microscopy (TEM). The deposited samples, prepared by magnetron sputtering using targets with the same global composition as cast WE43, exhibited chemically homogeneous microstructure without the formation of secondary phases typically observed in the cast alloy. The corrosion behavior was studied by PD and EIS tests. It was found that the deposited alloy showed enhanced corrosion resistance, ~8-fold reduction in corrosion rate compared to the cast alloy, owing to the elimination of micro-galvanic coupling between the Mg matrix and the precipitates. In-situ monitoring of hydrogen bubble evolution during corrosion indicated significantly reduced cathodic reaction kinetics in the deposited alloy. Post-corrosion surface and cross-sectional SEM studies showed that the high corrosion rate in the cast alloy was associated with the formation of severely cracked corrosion products preferably around Zr- and Y-containing precipitates.

CHAPTER 1: INTRODUCTION

1.1 Problem Statement and Research Significance

The design of light weight metals resistant to both corrosion degradation and wear damage for complex service conditions is increasingly demanding. Unfortunately, there is typically *a tradeoff between corrosion and wear resistance*. For example, aluminum (Al) is a well-known passive metal with good corrosion resistance due to the spontaneous formation of a protective oxide film on the surface, but highly susceptible to wear due to its low hardness. Moreover, during tribocorrosion (i.e. material degradation due to the combined effect of wear and corrosion) the mechanical wear will locally destroy the protective oxide film leading to rapid localized corrosion and early component failure. Most commercial Al alloys are precipitation hardened to enhance their mechanical properties, but the formation of secondary phases and precipitates also lead to a reduction in corrosion resistance due to galvanic coupling between the precipitates and Al matrix. Similar wear-corrosion resistance tradeoff dilemma is also observed in magnesium (Mg) alloys. For example, WE series Mg alloys (W represents Yttrium and E represents rare earth elements) are good candidates for biomedical application such as cardiovascular stents and bone anchors and screws, due to their biocompatibility, ability to degrade in vivo, and mechanical properties close to that of the human bones. However, the $Mg_{41}Nd_5$ and $Mg_{24}Y_5$ precipitates in WE Mg forms micro galvanic couples with the α-Mg matrix, leading to fast corrosion and loss of structural integrity of the implant before the patient is completely cured. This research aims at answering the question "*how to redesign Al and Mg*

alloys to improve their corrosion resistance without sacrificing strength?" The developed understanding from this study will thus serve as important design guidelines for producing novel metals and coatings with enhanced corrosion and wear resistance for use under complex service conditions.

1.2 Research Objective

To combat the wear-corrosion resistance tradeoff dilemma, it was hypothesized that eliminating precipitates in conventional alloys by forming a supersaturated solid solution, the alloying additions would strengthen the material without causing unfavorable galvanic coupling between precipitates and metal matrix, hence enhancing the wear and corrosion resistance simultaneously. The main objective of this dissertation is to test this hypothesis and investigate the role of alloy concentration and microstructure on the corrosion and tribocorrosion resistance of supersaturated solid solutions of Al and Mg alloys, which represent passive and active dissolution behaviors, respectively. Firstly, the effect of alloying additions on the corrosion and tribocorrosion resistance of binary Al-Mn was investigated. Secondly, the effect of chemical homogeneity on the corrosion resistance of a WE43 Mg alloy was studied in simulated physiological environment. Both alloys studied (Al-Mn and WE43) were produced using non-equilibrium processes (e.g. physical vapor deposition, or electrodeposition). The high effective quench rate of these processes enables the formation of supersaturated alloys with chemically homogeneity, ultrafine microstructure and smooth surface morphology. The main objective was successfully addressed by accomplishing the following aims.

1- Design and fabricate Al-Mn supersaturated solid solution. (Ch. 3)

2- Study how alloy concentration affects the microstructure. (Ch. 3)

3- Study how alloy microstructure affects corrosion, wear and their synergy of Al-Mn. (Ch. 3 and 4)

4- Investigate the role of different tribological and electrochemical variables on the tribocorrosion resistance of Al-Mn. (Ch. 4)

5- Synthetize a chemically homogenous i.e. precipitate-free WE43 Mg alloy. (Ch. 5)

6- Evaluate the role of chemical heterogeneity on the corrosion mechanisms of WE43 Mg alloys. (Ch. 5)

1.3 Dissertation Summary

To gain better understanding on the effects of alloy concentration and microstructure evolution on the corrosion and tribocorrosion resistance of Al and Mg alloys, supersaturated solid solutions of Al-Mn and WE-43 Mg alloys were fabricated by magnetron sputtering and tested for their corrosion and tribocorrosion resistance. The chapters of this dissertation are organized as follows:

Chapters 1 and 2 represent the essential framework of the dissertation. The problem statement and significance of the research are presented in chapter 1. The fundamental aspects of light weight metals (with more attention to Al and Mg alloys), corrosion and tribocorrosion mechanisms are discussed in chapter 2.

Chapter 3 discusses the effect of alloy concentration on the microstructure and corrosion resistance of supersaturated Al-Mn alloy. Al-Mn thin films were fabricated by magnetron sputtering. The microstructure evolution as a function of alloy concentration was investigated by grazing incidence X-ray diffraction (GIXRD), scanning electron microscopy (SEM), transmission electron microscopy (TEM), and energy-dispersive X-ray spectroscopy (EDS). The corrosion behavior was investigated in 0.6 M and 0.01 M NaCl aqueous solution. The

3

microstructure was tailored by changing alloy concentration. The pitting potential was found to be strongly affected by alloy composition. The crystalline alloy (Al-5at.%Mn) exhibited the best corrosion resistance over prolonged immersion tests, while the amorphous alloy (Al-20at.%Mn) showed the highest pitting potential during short term immersion.

Chapter 4 utilized the alloy concentration-structure-corrosion resistance relationship developed in chapter 3 to investigate the tribocorrosion response of the crystalline (Al-5at.%Mn) and amorphous (Al-20at.%Mn) Al-Mn alloys. The tribocorrosion tests were conducted in a reciprocating ball-on-plate mode using alumina ball as the counter piece in 0.6 M NaCl aqueous solution. The compact and dense passive film of the amorphous alloys together with the high H/E ratio improved the tribocorrosion resistance of Al. The repassivation current density required to repassivate the worn areas decreased by increasing Mn concentration.

Chapter 5 investigates the effect of chemical heterogeneity on the corrosion resistance of WE43 Mg alloy. Cast and magnetron sputtered samples were tested in blood bank buffered saline solution. The precipitate-free magnetron sputtered alloy with homogeneous microstructure showed a ~8-fold reduction in corrosion rate due to the elimination of the micro-galvanic coupling between the Mg matrix and the more electrochemically noble precipitates. In-situ video monitoring and post-corrosion microstructure characterization provides further understanding of the associated degradation mechanism.

CHAPTER 2: BACKGROUND

2.1 Light Weight Metals

The high strength-to-weight ratio (specific strength) of light metals and alloys promotes their use in structural, automotive and aerospace industries. Al (65 % lighter than steel) and Mg (33% and 75% lighter than Al and steel, respectively) alloys are promising replacement for conventional steel and cast iron in automobile manufacturing, driven by the strict regulations for enhancing fuel efficiency and reducing greenhouse gas emission [1]. In 2015, Ford released the all-aluminum-body F-150 truck with about 15% reduction in body weight. Al stands out compared to other metals for its recyclability, where ~ 75% of Al ever produced is still in use today. In 2015, 56.8 billion Al beverage can (Al-Mn-Mg alloy) have been recycled, accounting for an industry recycling rate of 64.3% [2]. The light weight of Al together with the high strength of some of its alloys, excellent corrosion resistance, excellent electrical and thermal conductivity, permits its use in automobile, aerospace and aircrafts industries, electrically heated appliances and utensils, decorative and functional uses, food and beverage packaging [3]. In addition, Al is also frequently applied as a corrosion protection coating for steel [4, 5], magnesium alloys [6, 7], and NdFeB magnets [8] etc., replacing the toxic cadmium coatings [9]. Common Al wrought alloys with their major alloying elements, properties and applications are listed in table 2.1 [10]. The U.S annual consumption and cost of Al for the past 5 years together with the consumption share of the major markets are shown in Fig 2.1 [11].

Mg is ductile, castable and has good damping properties. It is typically used in automobile, aircraft, aerospace, ballistics, electronics and armor applications [12, 13]. Common Mg wrought alloys with their major alloying elements, properties and applications are listed in table 2.2 [10]. The U.S annual consumption and cost of Mg for the past 5 years together with the consumption share of the major markets are shown in Fig 2.2 [11]. The use of Mg alloys in the automobile industries started in the 1920's in auto-racing vehicles, while the VW Beetle was the first commercial car to include Mg alloys [14]. Physiologically, Mg is the fourth common mineral available in human bodies, and Mg^{2+} is the second common intracellular cation [15]. Due to its biocompatibility, Mg and some of its alloys are considered promising materials for biodegradable applications such as cardiovascular stents [16, 17], tissue scaffolds, and bone screws [18-20]. For example, after several animal trials [21-23], WE43 absorbable cardiovascular stents were used clinically for the first time in 2003-2004 [24].

2.2 Fundamental Mechanisms of Metal Corrosion

2.2.1 Corrosion Reactions

Metallic corrosion is the process of the deterioration of a metal or of its properties due to (mostly electrochemical) reaction with the environment [25]. Consequences are important: in 2002, the direct cost of metallic corrosion in the United States was estimated as 3.1% of the U.S. Gross Domestic Product (GDP) [26]. In 2013 the global cost of corrosion was estimated to be 3.4% of global GDP [27]. For corrosion to occur, the following components must be present: a conductive solution (electrolyte), electronic path, anodic reaction, and cathodic reaction. The electrochemical deterioration of a metal (M) could be represented by the following anodic (oxidation) reaction;

$$M \rightarrow M^{n+} + ne^-. \tag{2.1}$$

To sustain the anodic reaction a matching, electron consuming, cathodic reaction is needed. A generalized cathodic reaction is shown in Eq. 2.2 and depending on the electrolyte it could take one of the common forms in Eq. 2.3-2.6 [28]:

$$aO_X + ne^- \rightarrow b \, Red \tag{2.2}$$

$$O_2 + 2H_2O + 4e^- \rightarrow 4OH^- \text{ (oxygen reduction in neutral and basic media)}, \tag{2.3}$$

$$O_2 + 4H^+ + 4e^- \rightarrow 2H_2O \text{ (oxygen reduction in acidic media)}, \tag{2.4}$$

$$2H^+ + 2e^- \rightarrow H_2 \text{ (hydrogen reduction)}, \tag{2.5}$$

$$2H_2O + 2e^- \rightarrow H_2 + 2OH^- \text{ (water reduction)}. \tag{2.6}$$
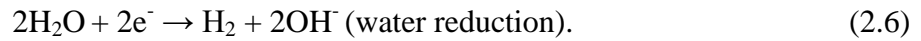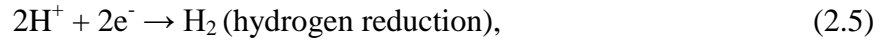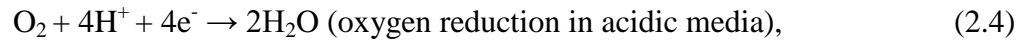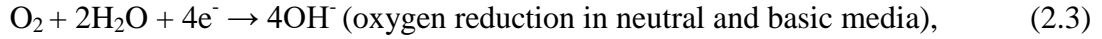
Fig. 2.3 shows a schematic representation of the electrochemical reactions of Mg (left) and Al (right) in either a neutral or basic solution. The rate of the anodic (oxidation) reaction in equation 2.1 is equal to the rate of cathodic (reduction) reaction in equations 2.2-2.5. Here the metal (Al or Mg) is oxidized to metal ion while electrons are released and consumed by the reduction reaction. The number of electrons equals the valence of the metal ions (2 and 3 for Mg and AL, respectively) released to the electrolyte [28]. When a metal is placed in a solution and establishes a dynamic equilibrium with its own ion by simultaneous occurrence of the reaction in Eq. 2.1 and its reverse cathodic reaction, the electrical potential difference between the metal and the solution is given by Nernst equation [25, 28, 29]:

$$(E)_{M^{n+}/M} = (E^O)_{M^{n+}/M} - \frac{RT}{nF} \ln[M]^{n+}. \tag{2.7}$$

The equilibrium potential for the reduction reaction in Eq. 2.2 and the simultaneous occurrence of its reverse anodic reaction is:

$$(E)_{ox/Red} = (E^O)_{ox/Red} - \left(\frac{RT}{nF}\right) \ln \left. [Ox]^a \middle/ [Red]^b \right. \tag{2.8}$$

The activity of the metal, oxidized and reduced species are represented by [M], [Ox], and [Red], respectively. E^O is the standard potential of each designated redox system. When the standard potentials of different metals are listed in ascending or descending order, taking the standard potential of the hydrogen ion system as the zero point, the electrochemical series of metals is formed (Table 2.3) [29]. A metal has the tendency to corrode (when placed in an environment where another redox system is present) if its equilibrium potential is more negative compared to the equilibrium potential of the other system. Both potentials have then a tendency to deviate from their equilibrium and support a coupled reaction at an intermediate mixed potential. The regimes of stability for the corrosion reactions can be illustrated using Pourbaix diagrams where the electrochemical potential is plotted vs. the pH of water [29]. From these diagrams it is possible to identify the electrochemical state of a metal (immunity, actively corroding, or passivity) at a specific pH and potential. The Pourbaix diagrams of Al [10] and Mg [30] are shown in Fig. 2.4 and 2.5, respectively. The dashed lines (a) and (b) in the diagrams represent the potentials below which hydrogen ion reduction and oxygen reduction reactions respectively become possible under standard conditions.

2.2.2 Classification of Electrochemical Corrosion

Generally corrosion is classified into two main categories: uniform and localized [29], based on the amount of metal loss before components failure. Total metal loss during uniform corrosion can be much higher than that of the localized corrosion [25], but the latter can be highly concentrated and have very adverse results. Uniform corrosion occurs when the entire surface of an exposed metal or alloy corrodes, while localized corrosion is the case when specific parts of the exposed surface corrode. Uniform corrosion is often manifested as atmospheric, galvanic, high temperature, liquid-metal, molten salt, biological, and stray-current corrosion. On

the other hand, localized corrosion includes selective dissolution, stress corrosion cracking, impingement attack, pitting, crevice, fretting, and intergranular corrosion [25].

2.2.3 Polarization Behavior of Electrochemical Systems

In the absence of any externally applied current, the rate of the anodic (oxidation) reaction in equation 2.1 is equal to the rate of the cathodic (reduction) reaction in equations 2.2-2.5. The electronic flow associated with the anodic and cathodic reactions can be quantified in terms of respective electric currents I_{anodic} and $I_{cathodic}$, with the former assigned by convention a positive sign while the latter is assigned a negative sign. When the two reactions are coupled as indicated above, a current $I_{corr} = I_{anodic} = |I_{cathodic}|$ represents the rate of both reactions and corresponds to the corrosion rate according to Faraday's law by:

$$I_{corr=} \frac{nFW}{MT} ,$$ (2.9)

where n is the valence of the metal, F is Faraday's constant (96,500 C.mol^{-1}), W is the atomic mass of the metal, M is the mass of corroded metal (g), and T is the length of time for which the current, if constant, was flowing (s). The potential difference between the corroding metal and a reference electrode is known as the open circuit potential (E_{oc}) or corrosion potential (E_{corr}). When an external current is applied to a corroding metal, the potential will deviate from the E_{oc} to another potential E, and the deviation is expressed as the overpotential $\eta=E-E_{oc}$. Fig. 2.6 shows a schematic representation of a polarization diagram. The current is expressed per unit area of the electrode in log scale (log i). In the diagram, the conditions for the unpolarized metal, $E_{o,c}$ and $E_{o,a}$ are the E_{oc} of the reduced and oxidized species, respectively. $i_{o,c}$ and $i_{o,a}$ are the exchange current densities of the reduced and oxidized species, respectively. The intersection of the anodic and cathodic reactions represents the E_{oc}/E_{corr} and i_{corr}. Similarly, E_{oc}/E_{corr} and i_{corr} are estimated as the intersection of the extrapolation of the linear parts (Tafel line) of the diagram

(condition of polarized metal). Under steady state and simple activation polarization conditions where the effect of mass transport is neglected, the total net current density ($i=i_a-i_c$) could be expressed by the Butler-Volmer equation [29, 31]:

$$i = i_{corr}\left[\frac{\alpha nF\eta}{RT} - \frac{(1-\alpha)nF\eta}{RT}\right], \tag{2.10}$$

where η is the overpotential, α is the half reaction transfer coefficient, β_a and β_c can be calculated from Tafel slopes as, $\beta_a = 2.3RT/\alpha nF$ and $\beta_c = -2.3RT/(1-\alpha)nF$ [25].

2.2.4 Electrochemical Measuring Methods

In this dissertation, the corrosion resistance of Al and Mg alloys is mainly evaluated using potentiodynamic (PD) and electrochemical impedance spectroscopy (EIS) tests. The working principles of these two methods are discussed next.

2.2.4.1 PD Tests

With the aid of commercially available instruments such as galvanostat/potentiostat, the polarization diagram (red line) shown in Fig. 2.6 is generated by observing the response of the current under either static or dynamic control of potential. The potential is varied by either a sweep or a step mode over a selected range and rate. Similarly, in galvanostatic experiments, the current is controlled and the potential response is measured. Linear polarization methods are used to compute the corrosion rate of a metal. The corrosion current density (i_{corr}) can be obtained from the polarization resistance (R_P) and Tafel slopes as:

$$i_{corr} = \frac{B}{R_P}, \tag{2.11}$$

where R_P is defined as the ratio of change in potential to the current. Experimentally, Rp is determined from the slope of the short nearly linear segment of the polarization curve when plotted as a function of current density in a linear scale. As shown in [25] B is calculated by:

$$B = \frac{\beta_a \cdot \beta_c}{2.3(\beta_a + \beta_c)}.$$ (2.12)

For passive metals such as Al, Ti, and stainless steel, the anodic curve of the polarization

diagram (Fig. 2.6) will exhibit a characteristic behavior as schematically shown in Fig. 2.7. By

increasing the potential above the passivation potential (E_P), the current density rapidly decreases

(thus indicating a decreased anodic reaction rate) from a critical value (i_c) to a value

corresponding to the passive current density (i_P). In the region between the passive and

transpassive potentials, the metal is covered with a highly protective oxide or hydroxide film

[25].

2.2.4.2 EIS Tests

EIS is a useful technique to better quantify electrochemical parameters of a system. Due

to the small amplitude ac signal used compared to other electrochemical methods, EIS is

considered a nondestructive electrochemical test, from which various system parameters such as

R_P and the value of interfacial capacitance corrosion rate, reaction kinetics, mass transport,

dielectric properties, and detection of localized corrosion can be obtained [32]. Other advantages

of this technique include, capability of probing relaxation phenomena over wide range of

frequencies, its steady sate nature, and availability of time dependent data [33]. The major

challenge in EIS is the complexity of data analysis, usually by means of equivalent circuits

used to fit experimental data [33]. When a small-amplitude sinusoidal potential (± 10 mV) is

applied to a metal-electrolyte interface at various frequencies, the resulting alternating current

(AC) may be out of phase compared to the applied potential as shown in Fig. 2.8. EIS analysis is

represented as Nyquist (Fig. 2.9.a) or Bode plots (Fig. 2.9.b). For the simple case illustrated

there, the impedance at the low frequency limit equals ($R_S + R_P$) and at the high frequency limit

equals R_S, where R_S is the solution resistance. The electrode-solution interface may often be

modeled as an equivalent circuit shown as a simple form in the inset of Fig. 2.9.a, where C is the double layer capacitance for ideal system behavior and is replaced by constant phase element (CPE) for non-ideal behavior [34]. The components of the CPE are discussed in more detail in section 3.3.

2.2.5 Corrosion Mechanism of Al and Al Alloys

The corrosion behavior of Al is best viewed using Pourbaix diagram shown in Fig. 2.4. Al is stable in metallic state at potentials below -1.8 V vs. SHE. Above this potential and in the pH range of -2 to 4.5, Al will oxidize to Al^{3+} in acidic environment. In the pH range between 4.5 and 10, the oxide film is thermodynamically stable. At pH greater than 10.5, Al will corrode under alkaline condition to aluminate (AlO_2^-) [35]. Moon and Pyun [36] found that the corrosion rate of pure Al in ($mg.cm^{-2}.min^{-1}$) increased dramatically from 0.002 at acidic pH to 0.05 at alkaline pH. Depending on the forming conditions, the oxide film grown on Al has different physical and chemical properties [37]. The oxide was found to be amorphous for air-bourne oxides. Films grown in a borate or tartaric acids are thin, dense and amorphous. In sulfuric and phosphoric acids, the films are thick, porous and crystalline. The corrosion of Al and Al alloys is governed by the protectiveness of its passive film [37]. For example, when exposed to halogens containing media (scope of chapter 3), the susceptibility to localized corrosion will depend on the chemical composition, content of micro and macro defects, crystal structure and degree of non-crystallinity of the passive film [37]. A schematic presentation of the pitting process of a passive metal in Cl^- and O_2 contain aqueous solution is shown in Fig. 2.10. Once the passive film is locally destroyed, an active (inside the pit)–passive (cathode) coupling occurs and the Cl^- concentration and pH of the electrolyte inside the pit will change significantly [25]. The Cl^- will move to the bottom of the pit, while O_2 will react with water on the metal surface. The oxidation

and reduction reactions occur similarly as those of Eq. 2.1 and 2.3, respectively [29]. The pH drop is related to the acidity increase at the bottom of the pit due to the formation of acidic condition by the hydrolysis of Al to Al^{3+} and the reaction of Al^{3+} with Cl^- and water [38]:

$$Al^{3+} + 2H_2O \rightarrow H^+ + Al(OH)^{2+}. \tag{2.13}$$

$$Al(OH)^{2+} + Cl^- \rightarrow Al(OH)Cl^+. \tag{2.14}$$

$$Al(OH)Cl^+ + H_2O \rightarrow Al(OH)_2Cl + H^+. \tag{2.15}$$
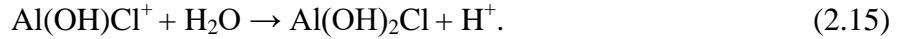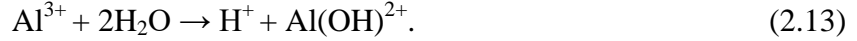
Indeed, Augustynski et al. [39] reported the incorporation of Cl^- ions within the initial 10-15 Å of the oxide film at the oxide/electrolyte interface, the quantities of incorporated Cl^- ions increases at higher temperature and at more anodic potentials.

2.2.5.1 Effects of Allying Concentration on Al Corrosion

Alloying has been found to be a highly effective method to strengthen Al by forming precipitates or secondary particles [40]. However, the presence of precipitation and secondary particles enhances corrosion by catalyzing oxygen reduction, increasing the alloy corrosion potential, and localizing the electrochemical activity due to chemical inhomogeneity from the Al matrix [41]. Recent studies show that alloying can increase the pitting potential (E_{pit}) of Al provided that the alloying elements are retained in solid solution [42-45]. For example, age-hardened 2000 series Al alloys (with Cu as the major alloying element) exhibit poor corrosion resistance [41], but Kim et al. observed an ennoblement of E_{pit} with increasing Cu content in Al-Cu solid solutions [42, 43]. Alloying Al with appropriate transition metals (TMs) such as Mo, Mn, W, Nb, Cr, Ta, V, and Zr in metastable solid solutions offers the possibility to significantly enhance its pitting resistance in chloride solutions [37]. These TMs improve corrosion resistance and decrease pitting susceptibility of Al by increasing the overpotential for anodic dissolution and decreasing metastable pit initiation and growth rates [42]. In addition, alloying is an effective

13

way to minimize grain size and produce nanocrystalline microstructure. These refined microstructures are likely to promote passive film growth due to the high density of point defect sinks and sources at the intersection between grain boundaries and the film/metal interface [46, 47]. The effects of alloying concentration on E_{pit}, i_{corr}, and hardness of Al are sown in Fig. 2.11.

Different Al alloys contains different intermetallics (second phases) [48], such as Al_6Fe and Al_3Fe in 1xxx alloys, AlMg and AlMnMg in 3xxx alloys. Particles containing Cu and Fe were found to decrease the pitting potentials of Al. The electrochemical nobler phase will serve as cathode leading to the anodic dissolution of the matrix. Nisancioglu [49] found that under alkaline condition and near the corrosion potential, Al is selectively dissolved from the Al_3Fe. Mazurkiewicz and Piotrowski [50] reported the dissolution of Al_2Cu and the formation of Al^{3+} and Cu^{2+} in sulfate solution under open circuit and anodic conditions. Other intermetallics such as AlMgMn, AlMnCr and AlMnCr were found to have no effect on the corrosion of Al [37].

2.2.6 Corrosion Mechanism of Mg and Mg Alloys

As indicated previously, Fig. 2.5 shows Pourbaix diagram for Mg-water system at 25 $^\circ$C [30]. Mg metal is thermodynamically stable only at potentials below -2.4 V vs. SHE. Above this potential Mg will oxidize to Mg^{2+}. At pH greater than 8, $Mg(OH)_2$ is insoluble hence this film is considered as a protective hydroxide. In Fig. 2.5, the labels 0, -2, -4 and -6 are the activities of the soluble ions in log scale.

The standard potential of Mg/Mg^{2+} is -2.37 V vs. NHE, this value increases to -1.7 V vs. NHE for Mg corrosion in diluted NaCl solution due to the formation of oxide/hydroxide film on the metal surface [51, 52].
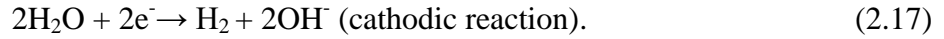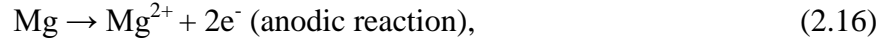
14

Corrosion of Mg occurs as per the following half-cell reactions [53, 54]

$$Mg \rightarrow Mg^{2+} + 2e^- \text{ (anodic reaction)}, \quad (2.16)$$

$$2H_2O + 2e^- \rightarrow H_2 + 2OH^- \text{ (cathodic reaction)}. \quad (2.17)$$

The electrons released from the dissolution of Mg (anodic reaction) are consumed by the cathodic reaction to generate H_2 gas [55]. The Mg^{2+} and OH^- ions formed by the anodic and cathodic reactions, respectively, will then combine to form $Mg(OH)_2$ film as [53];

$$Mg^{2+} + 2OH^- \rightarrow Mg(OH)_2. \quad (2.18)$$

Extensive past research [51, 53, 56-58] have shown that the rate of hydrogen evolution (hence corrosion rate) increased with applied anodic polarization, a phenomena also known as negative difference effect (NDE) [59, 60]. Mg is speculated to undergo electrochemical dissolution to an intermediate uni-positive Mg^+ (denoted with a question mark in Pourbaix diagram), which in turn reacts with water to generate hydrogen gas as follows [53]:

$$Mg \rightarrow Mg^+ + e^-, \quad (2.19)$$

$$Mg^+ + H_2O \rightarrow Mg^{2+} + 1/2H_2 + OH^-. \quad (2.20)$$

Generally, the oxide layer formed on Mg surface is composed of an inner MgO and outer $Mg(OH)_2$ layer [61-63]. The specific composition and structure of this layer is heavily influenced by the alloy composition. For example, Jonsson et al. [64] reported the existence of a layer containing both Al and Mg oxides on the surface of AZ91D. Philips and Kish [62] reported the formation of two diffused oxide layers on AZ80 Mg alloy exposed to pure water; the outmost layer was composed of double Mg-Al hydroxide compound $[Mg_6Al_2(OH)_{18} \cdot 4H_2O]$ and incorporation of Al with Mg as hydroxide compound, whereas the interlayer at the substrate/film interface was enriched in Zn. Nordlien et al. [61] found that for Mg immersed in distilled water,

the oxide film (schematically shown in Fig. 2.12) is composed of a 400-600 nm bottom cellular like layer, a 20-40 nm dense middle layer, and a 1800-2200 nm platelet like upper layer.

As mentioned earlier, Mg is highly susceptible to galvanic corrosion as shown in Fig. 2.13, The cathode is either an adjacent external metal having lower hydrogen overpotential such as Ni, Fe, and Cu (Fig. 2.13.a) or internal cathodes such as impurities or secondary phases present within the alloy microstructure (Fig. 2.13.b) [51].

2.2.6.1 Effects of Allying Concentration and Microstructure on Mg Corrosion

The role of different alloying elements on the corrosion resistance of Mg has been reviewed by Gusieva et al. [54]. Fig. 2.13 summarizes the effect of alloying elements on the electrochemical properties of Mg. When alloying elements were added to improve the mechanical properties of Mg, the resulting changes in chemical composition and microstructure play critical roles in affecting the corrosion behavior of the alloys [54]. Most alloying elements have very limited solubility in Mg [65]. By increasing alloy concentration, the fraction of secondary phases increases, leading to the formation of micro-galvanic coupling between the Mg matrix and the more cathodic secondary phases, hence accelerating the cathodic activity i.e. reduction reaction [66]. Al has the highest solubility ~12 wt.% in Mg. Its addition increases the strength of Mg from ~70 to 250 MPa [67], but at the same time reduces the ductility from 19% at 1.9 wt.% Al to 0.7% at 17.8 wt.% Al, due to the formation of β- and eutectic phases [68, 69]. Below the solubility limit, the addition of Al reduced the anodic activity and ennobles the corrosion potential [70, 71]. The addition of Ag up to 0.1 wt.% increases the hardness of AZ91 alloy without sacrificing the corrosion behavior [72]. Further increasing the concentration of Ag will increase the rate of corrosion due to the galvanic coupling between Mg matrix and the Mg_4Ag precipitates [73]. It was found that up to ~5 wt.% addition of Mn has no effect on the

16

corrosion behavior of Mg. Mn is commonly added to Mg-Al and Mg-Al-Zn. The formation of compound such as Al_8Mn_5, Al_6Mn and Al_4Mn reduces the corrosion rate. It was reported that the addition of Mn isolates Fe in AlMnFe intermetallic particles, hence reducing the effect of micro-galvanic coupling [74]. The high solubility of Y in Mg, similar electrochemical potential, same crystal structure, and similar atomic radii promotes the effective strengthening of Mg by the formation of precipitates or secondary particles [16, 75]. The addition of Y with other rare earth elements was also found to enhance the creep resistance of Mg alloy due to the formation of Y rich phases [16]. Nd was found to be biocompatible [76, 77] and effective in enhancing the corrosion resistance of Mg alloys by reducing micro-galvanic effects due to the presence of intermetallic compounds [78-80]. Nd also enhances the mechanical properties of Mg by forming intermetallic phases at the grain boundaries [17, 78, 81]. Zr addition increases the strength of Mg mainly by grain refinement [82]. Due to the limited solubility of Zr in Mg, the undissolved Zr particles act as selective nucleation cites during solidification. The corrosion resistance of Mg was found to be enhanced when the concentration of Zr is kept below 2% [16]. Li and Ca are more electronegative than Mg and their addition increases the anodic reactions [83, 84]. Ni, Fe and Cu are insoluble in Mg and found to increase the cathodic activities [66, 85].

In addition to alloying, materials microstructure such as grain size and texture also affects corrosion of Mg alloys [86, 87]. The enhanced corrosion behavior of Mg by reducing grain size is related to the enhanced corrosion performances of the passive layer [88], β-phase [89] and corrosion product layer [90]. Hoog et al. [91] reported the reduction in anodic kinetics of severely deformed Mg sample with refined grains. Argade et al. [92] used friction stir processing to reduce the grain size of Mg-Y-RE alloys, and found that the ultra-fine grain microstructure exhibited highest polarization resistance, most positive pitting and repassivation potentials

compared to coarse grained counterpart. Ralston et al. [93] suggested that the environment is the controlling factor in determining the grain size- electrochemical response relationship.

Even for chemically homogeneous Mg alloys, where no precipitates induced galvanic corrosion forms, the change in the crystallographic texture is expected to influence the corrosion resistance. Grains with different crystallographic orientation i.e. electrochemical activities will form galvanic coupling. For Mg alloys, the atomic density of the basal (0001), prismatic type 2 ($11\bar{2}0$), prismatic type 1 ($10\bar{1}0$) planes are 1.13×10^{19}, 6.94×10^{18}, and 5.99×10^{18} atoms/m^2, respectively. The surface energy have been estimated to be 1.54×10^{4}, 2.99×10^{4} and 3.04×10^{4} J/m^2 for (0001), ($11\bar{2}0$), and ($10\bar{1}0$) plane, respectively [94]. It was reported that Mg alloys with high basal plane texture exhibited better corrosion resistance compared with those with high the prismatic planes on the surface. Thus alloys having high basal preferred orientation are expected to exhibit lower corrosion rates compared with alloys having larger amount of high surface energy texture.

2.3 Fundamental Mechanisms of Tribocorrosion

Tribocorrosion is a complex process of material's degradation due to the synergistic contribution of chemical corrosion and mechanical wear in tribological contact [95-97]. Tribocorrosion is expected to take place under different applications such as in orthopedic implants, nuclear power plants, marine and offshore industries, chemical pumps, food processing and mining machineries.

During tribocorrosion, the chemical corrosion and mechanical wear are related by [98];

$$T = W_0 + C_0 + S. \qquad (2.21)$$

where T is the total material loss, W_0 is the material loss due to wear without the influence of corrosion, C_0 is the material loss due to corrosion without the influence of wear, and S is the synergistic effect of corrosion induced wear (ΔW_C) and wear induced corrosion (ΔC_W).

$$S = \Delta W_C + \Delta C_W. \qquad\qquad (2.22)$$

Landolt et al. [96] categorized the different conditions under which tribocorrosion degradation might occur as schematically shown in Fig 2.14. Here, two or three body contacts between the relative sliding surfaces are expected. Movements could be either unidirectional or reciprocating. Fretting is a condition where the reciprocating motion is in the range of few micrometers. Ball bearing is an example of rolling contact configuration. Pipes and pumps carrying slurry particles is an example of erosion corrosion. Landolt et al. [96] also categorized the parameters that affect sliding tribocorrosion into four categories: 1) material parameters (hardness, plasticity, microstructure, surface roughness, wear debris, and oxide film properties). 2) solution parameters (viscosity, conductivity, pH, corrosively, temperature, and oxygen content). 3) electrochemical parameters (applied potential, ohmic resistance, oxide film growth, valence, active dissolution, and repassivation kinetics). 4) mechanical parameters (normal load, sliding velocity, motion, contact bodies, alignment, and vibrations). Dearnley and Aldrich-Smith [99] categorized the tribocorrosion processes of hard cathodic coating on a metal surface such as coating stainless steel with S-phase and CrN into three categories: 1) removal and regeneration of passive film during sliding contact, where no chemical reaction is expected to occur on the substrate and the regeneration of the passive film reduces the susceptibility to localized corrosion, 2) removal of the coating due to the formation of blisters in aggressive corroding media, where Cl^- ions are expected to breakdown the passive film, de-bond the coating from the

substrate and ultimately attack the substrate, and 3) abrasion of the coating due to the roughening of the material interfaces when active counter pieces are used.

Tribocorrosion is critical for passive metals and alloys. During corrosion these metals are protected by their own passive films. But once mechanical wear takes place, the passive film is locally destroyed generating galvanic coupling between the passive and non-passive regions. Subsequently early component failure is mostly expected [95, 97, 100, 101]. Fig. 2.15 shows a schematic presentation of possible relevant mechanisms influencing the tribocorrosion behaviors of passive metals and alloys. Once a mechanical wear is applied, the native oxide film is locally removed, and the underneath metal region is now exposed to the corrosive media. The worn area (anode) exhibit high anodic current density transient, while the rest of the still passive region (cathode) exhibits increase in the cathodic current density [102]. In supersaturated alloys of Al and transition metals (scope of chapter 4), the re-growth of passive film is governed by two counteracting effects, a desirable effect by the high density of point defect sinks and sources at the intersection between grain boundaries and the film/metal interface, and a non-desirable effect due to the increase in the dissolution current densities and pitting tendency at the still passive regions [46]. The cathodic reaction is mainly governed by the extent of grain boundaries intersections and film defect injection and sinks. The existence of alloying elements intended to increase the hardness; hence the tribological properties of Al are also expected to alter the repassivation of worn areas, particularly at high alloying concentrations and finer grain size, where additional deformation methods such as grain boundary segregation and grain rotation are expected to occur. Finally, when third parties such as wear debris agglomerate between the indenter and the worn surface, the rate of passive film removal is expected to aggravate.

20

Table 2.1 List of common Al alloys, their properties and applications [10].

Alloy ID	Major alloying elements	Properties	Applications
1xxx	-	Work hardened Excellent corrosion resistance High thermal and electrical conductivity	Electric condensers Lightning devices Decorative
2xxx	Cu	Precipitation hardened Susceptible to stress corrosion cracking	Aircraft and aerospace Cycling frames
3xxx	Mn	Work hardened Moderate strength Good workability Very high resistance to corrosion	Cladding panels Roofing sheets Heat exchanger tubing Circles for kitchen utensils
4xxx	Si	Good corrosion resistance	Brazing and welding products Cladding panels
5xxx	Mg	Strongest non-heat treatable Al alloys High corrosion resistance in alkali media High as-welded strength	Chemical processing Food handling Marine applications
6xxx	Mg & Si	Precipitation hardened Good corrosion resistance Medium strength Formability and weldability	Aerospace applications Marine applications Automotive applications
7xxx	Zn	Precipitation hardened Heat treatable High resistance to general corrosion High strength	Structural, marine, machinery Process equipment
8xxx	other	Good formability	Fins for heat exchangers Spiral tubes Thin foils

Table 2.2 List of common Mg alloys, their properties and applications [10, 103, 104].

Alloy ID	Major alloying elements	Properties	Applications
AZ31	Al, Zn, Mn	Medium strength Weldable Good formability	Aircraft fuselage Cell phones Laptops
AZ91	Al, Zn, Mn	Excellent castability RT good mechanical properties Good corrosion resistance	Door mirror brackets Valve and cam covers
AM50	Al, Mn	High elongation and energy absorption	High-pressure die casting Steering wheels Seats
AM60	Al, Mn	Good casting properties High mechanical strength	Fans Steering wheels Inlet manifolds
ZE41	Zn, Nd	Good strength Castable	Ballistics Aircraft parts
QE22	Ag, Nd	Weldable High proof stress	Aerospace applications
ZK60	Zn, Zr	Good strength and ductility	Military components Tent poles Sports equipment
WE43	Y, RE, Zr	Good castability High heat resistance High creep resistance Ageing resistance Good fatigue strength Corrosion resistance	Helicopter transmission Race cars Biological applications

Table 2.3 Standard potentials of metals [29].

Type	Reduction reaction	$E^O (V_{SHE})$
Noble	$Au^{3+} + 3e^- = Au$	+ 1.498
	$O_2 + 4H^+ + 4e^- = 2H_2O$	+ 1.229
	$Pt^{2+} + 2e^- = Pt$	+ 1.200
	$Pd^{2+} + 2e^- = Pd$	+ 0.987
	$Ag^{2+} + 2e^- = Ag$	+ 0.799
	$Fe^{3+} + e^- = Fe^{2+}$	+ 0.770
	$Cu^{2+} + 2e^- = Cu$	+ 0.337
	$2H^+ + 2e^- = H_2$	0.000
	$Fe^{3+} + 3e^- = Fe$	- 0.036
	$Pb^{2+} + 2e^- = Pb$	- 0.126
	$Ni^{2+} + 2e^- = Ni$	- 0.250
	$Co^{2+} + 2e^- = Co$	- 0.277
	$Cd^{2+} + 2e^- = Cd$	- 0.403
	$Fe^{2+} + 2e^- = Fe$	- 0.440
	$Cr^{3+} + 3e^- = Cr$	- 0.744
	$Zn^{2+} + 2e^- = Zn$	- 0.763
	$Ti^{2+} + 2e^- = Ti$	- 1.630
	$Al^{3+} + 3e^- = Al$	- 1.662
	$Mg^{2+} + 2e^- = Mg$	- 2.363
	$Na^+ + e^- = Na$	- 2.714
	$K^+ + e^- = K$	- 2.925
Active	$Li^+ + e^- = Li$	- 3.045
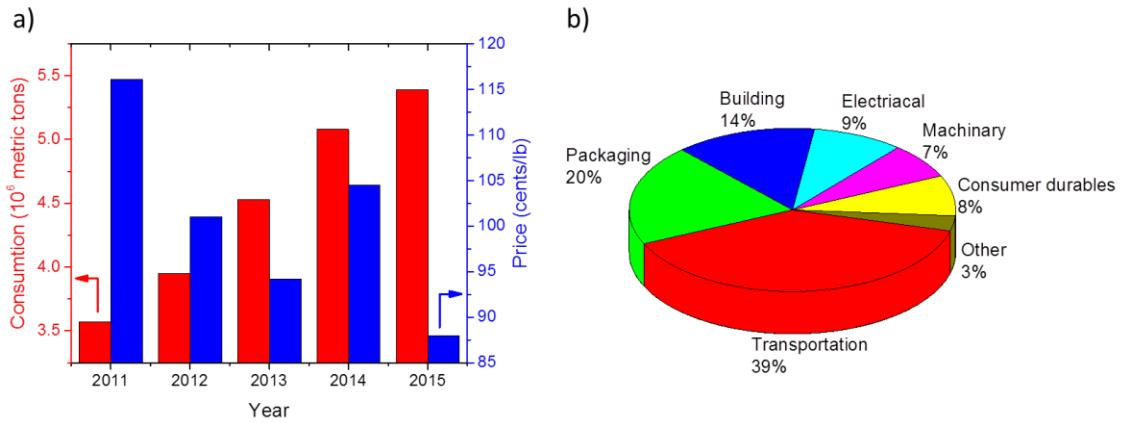
Figure 2.1 a) U.S. annual consumption and cost of Al, b) Al major markets consumptions in 2015 [11].
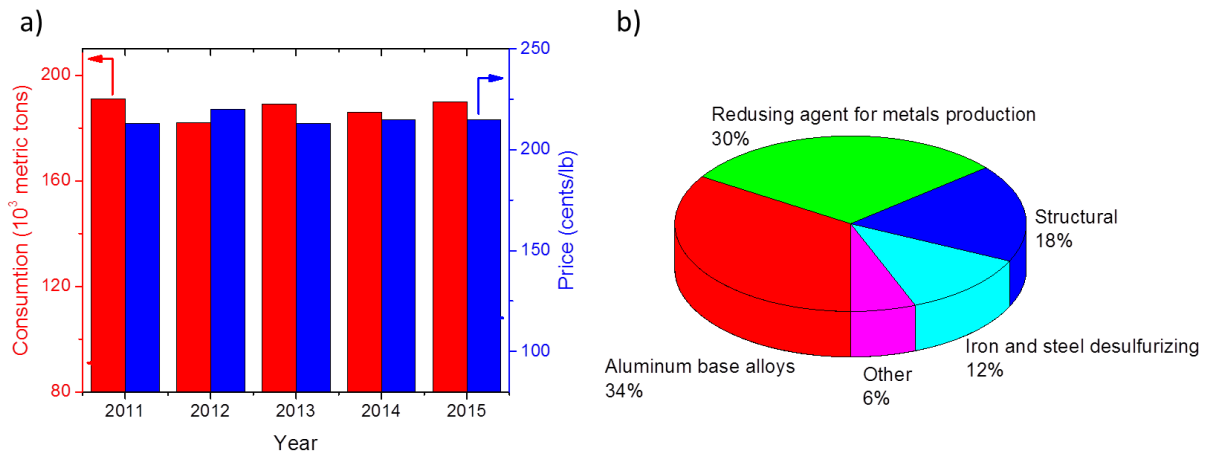
Figure 2.2 a) U.S. annual consumption and cost of Mg, b) Mg major markets consumptions in 2015 [7].
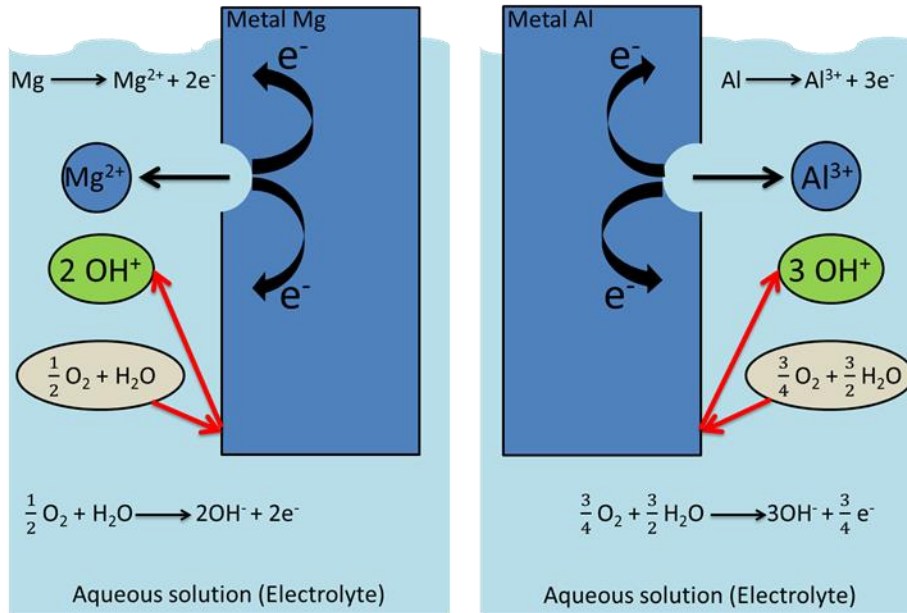
Figure 2.3 Simple schematic of corrosion process of Mg (left) and Al (right) in neutral aqueous solution with dissolved oxygen.
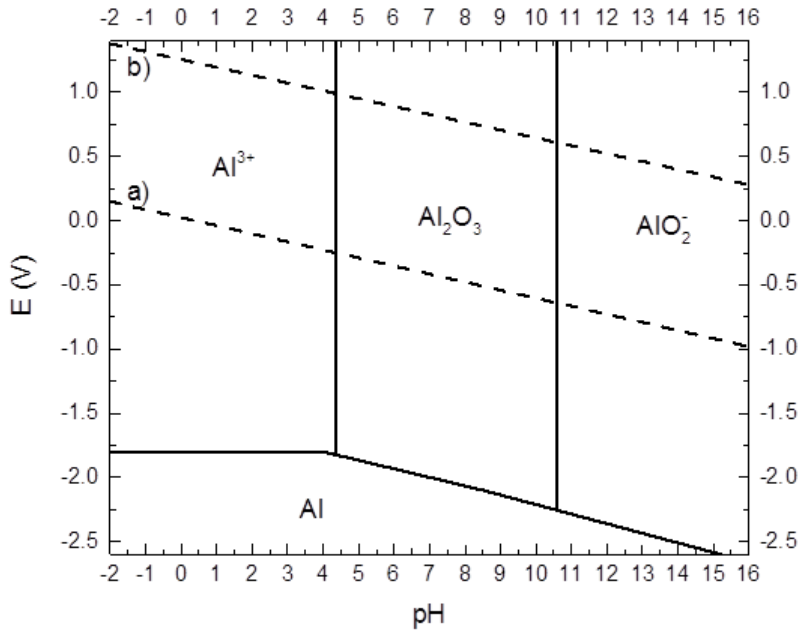
Figure 2.4 Pourbaix diagram for the Al-water system at 25 °C [10].

25
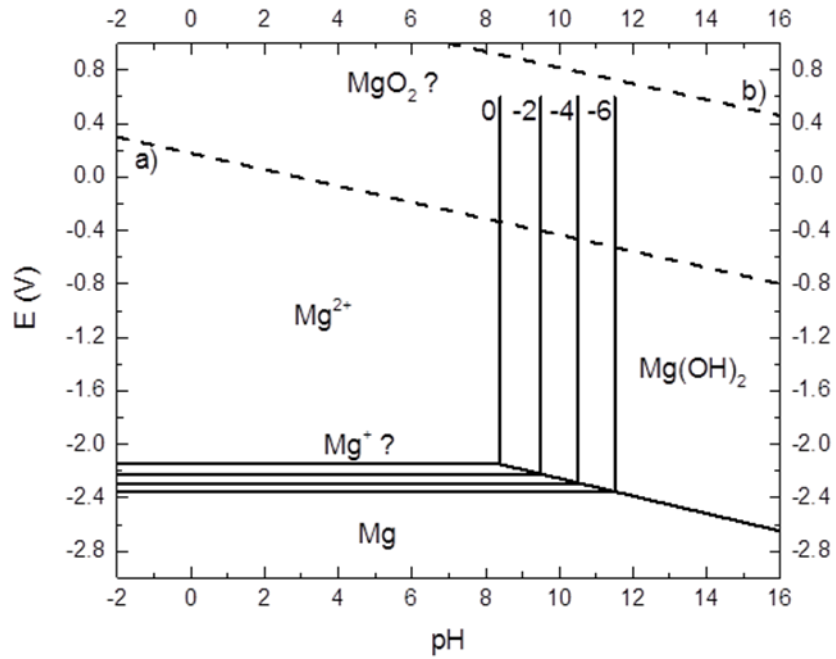
Figure 2.5 Pourbaix diagram for the Mg-water system at 25 °C [30].
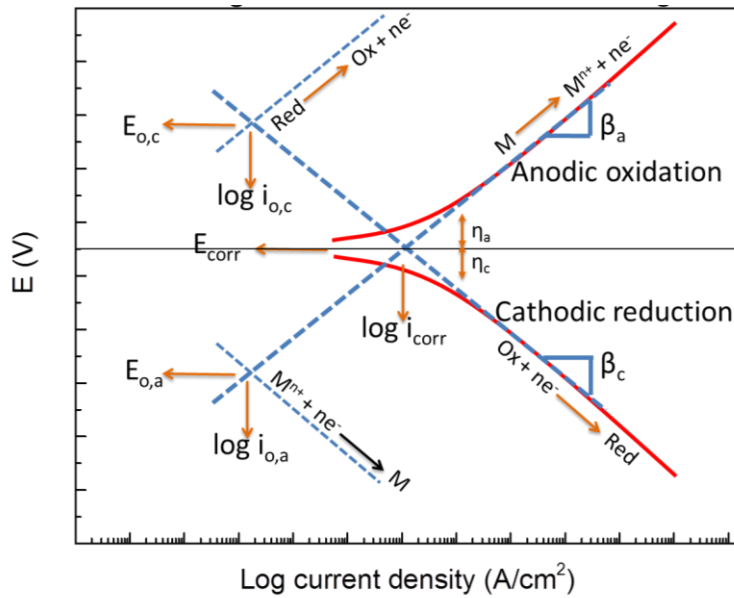
Figure 2.6 Schematic presentation of cathodic and anodic polarization curves [10].
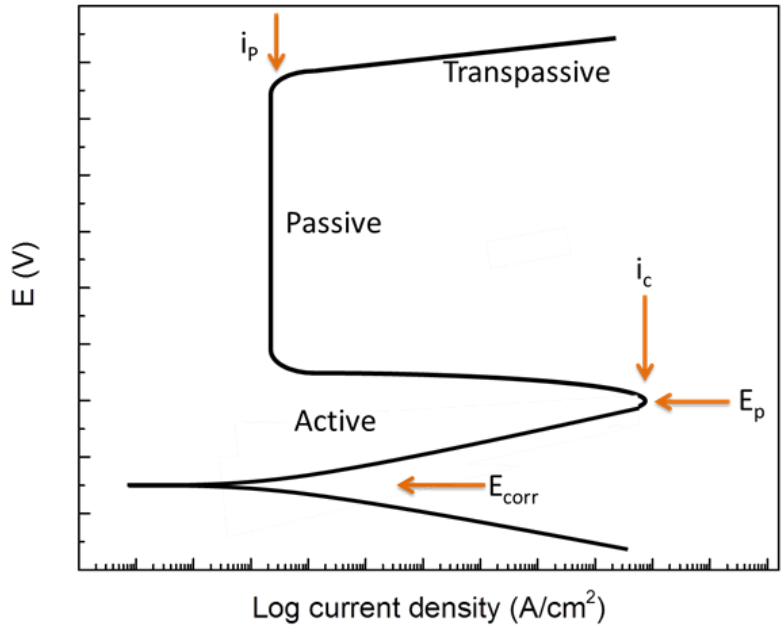
Figure 2.7 Polarization diagram of passive metals.
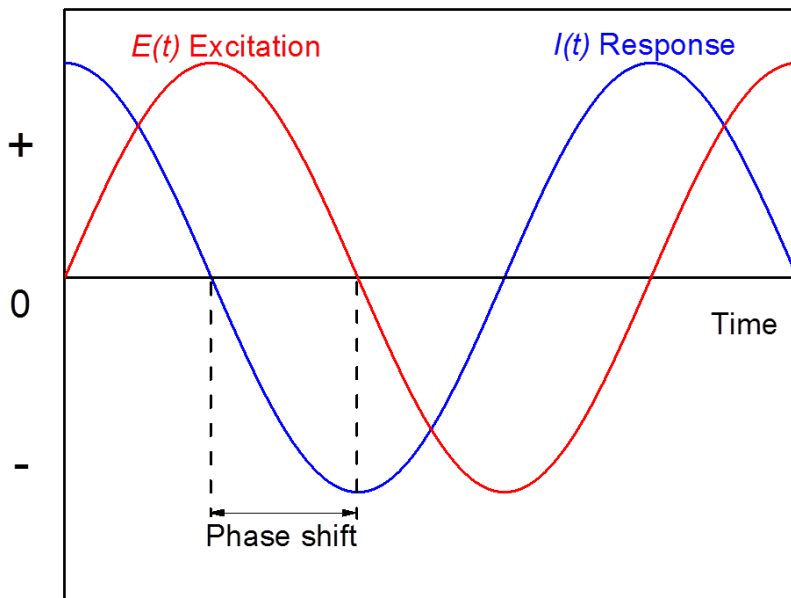
Figure 2.8 Schematic sinusoidal potential excitation for impedance measurements [29].
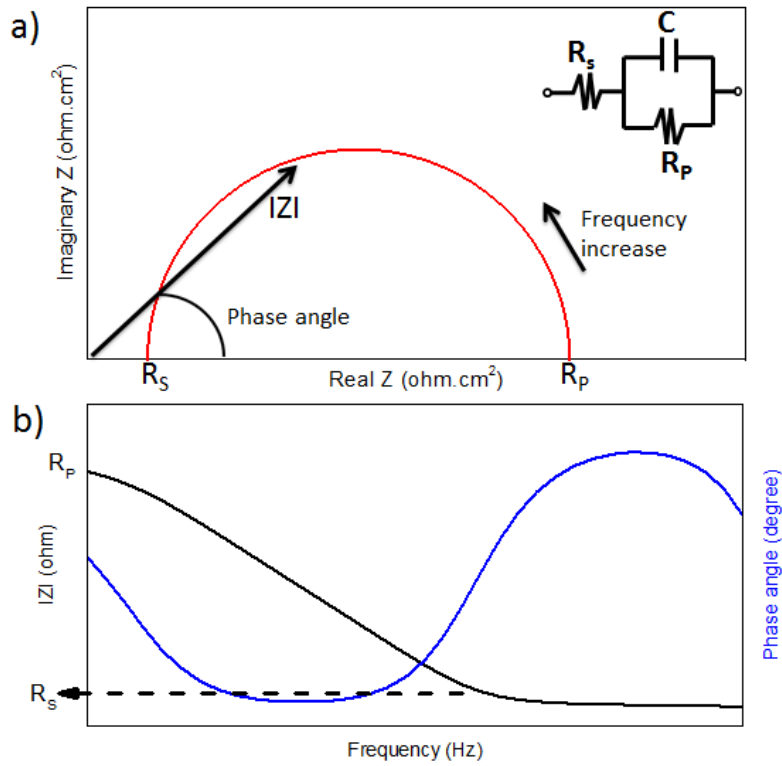
Figure 2.9 Nyquist a) and bode b) representation of the impedance behavior.
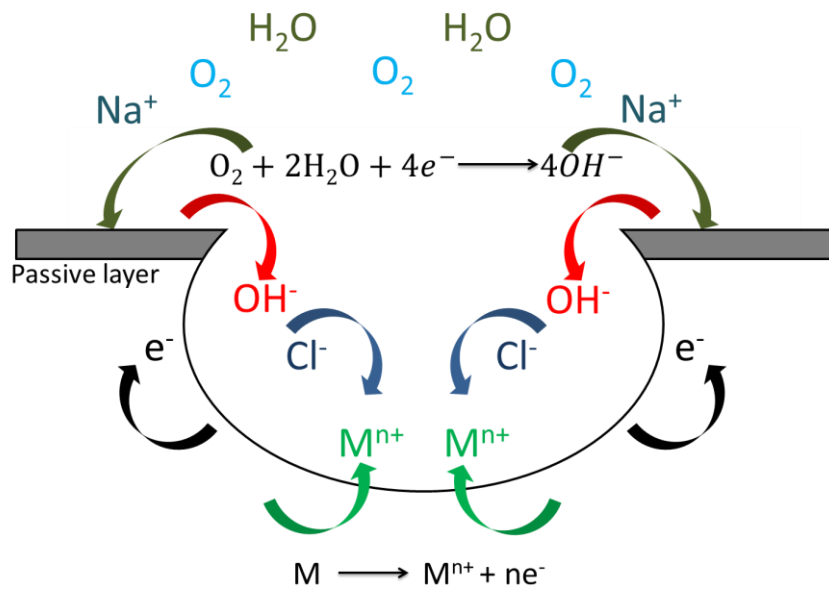
Figure 2.10 Pitting corrosion process of metal (M) in Cl⁻ containing aqueous solution [25].
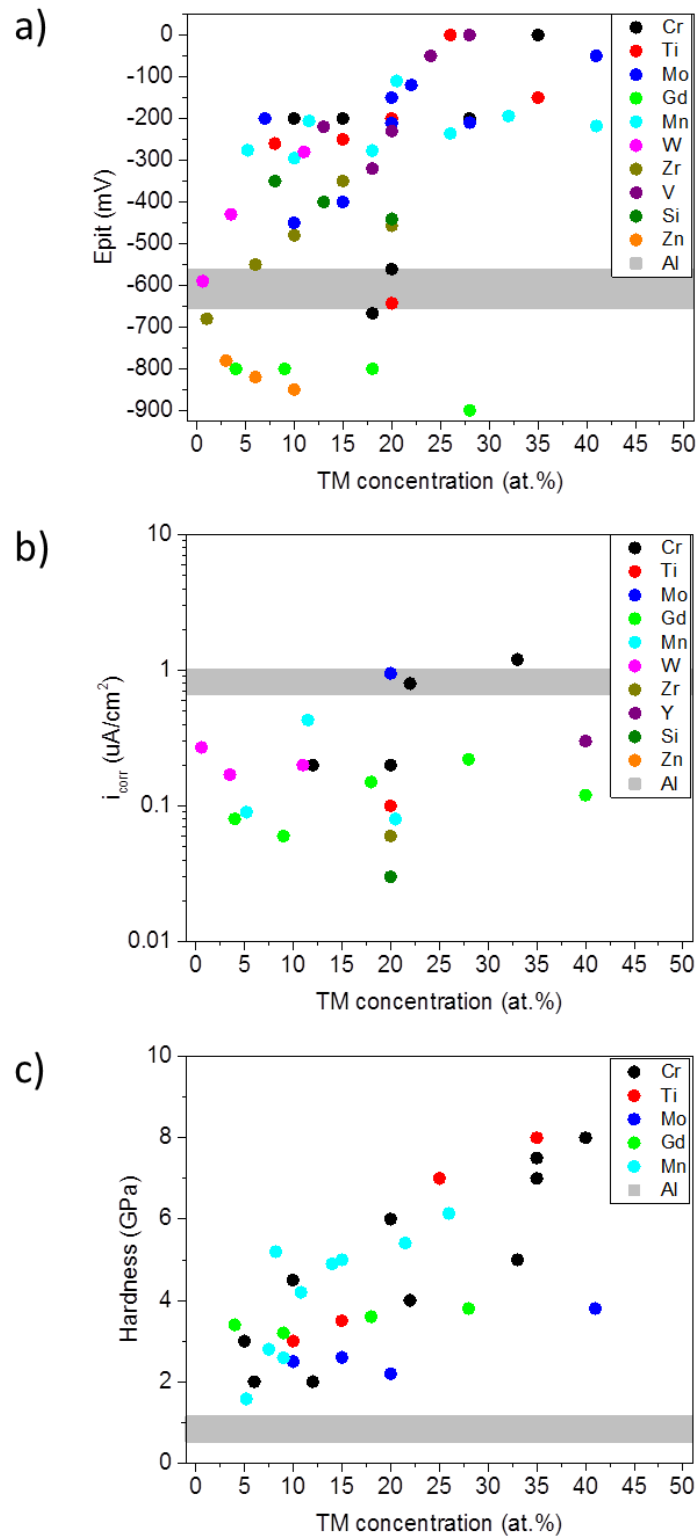
Figure 2.11 Effects of alloying elements on a) pitting potential, b)i_{corr} and c) hardness of Al [9, 44, 105-112].
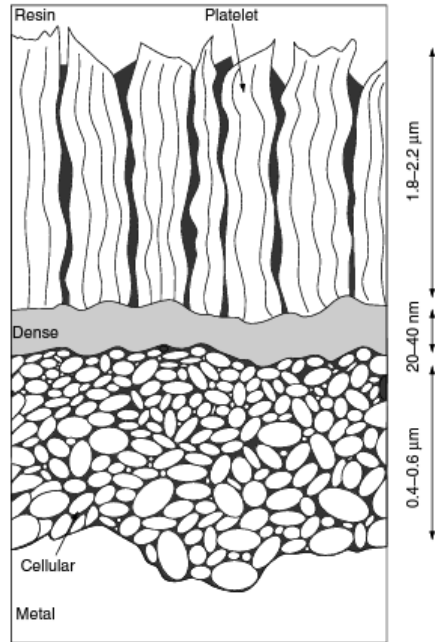
Figure 2.12 Schematic of the trilayer oxide film structure on corroded magnesium [10].
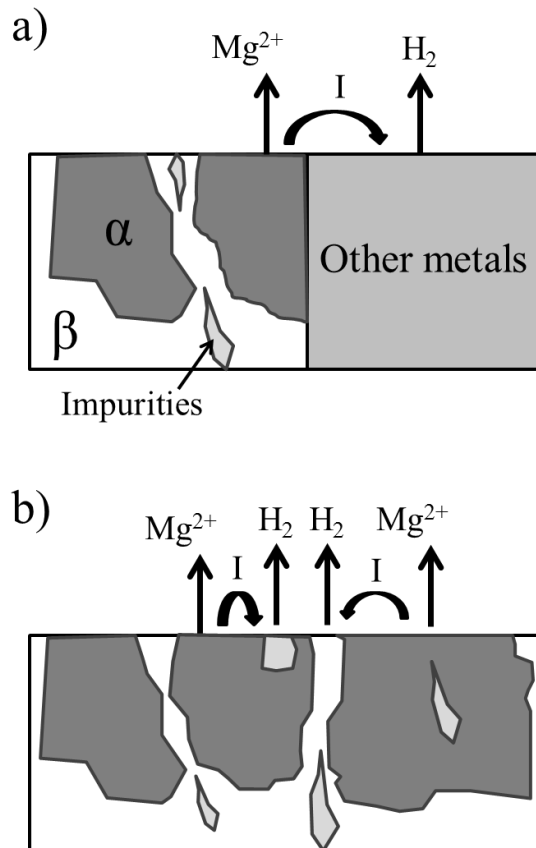
Figure 2.13 Schematic of external a) and internal b) galvanic corrosion [51].
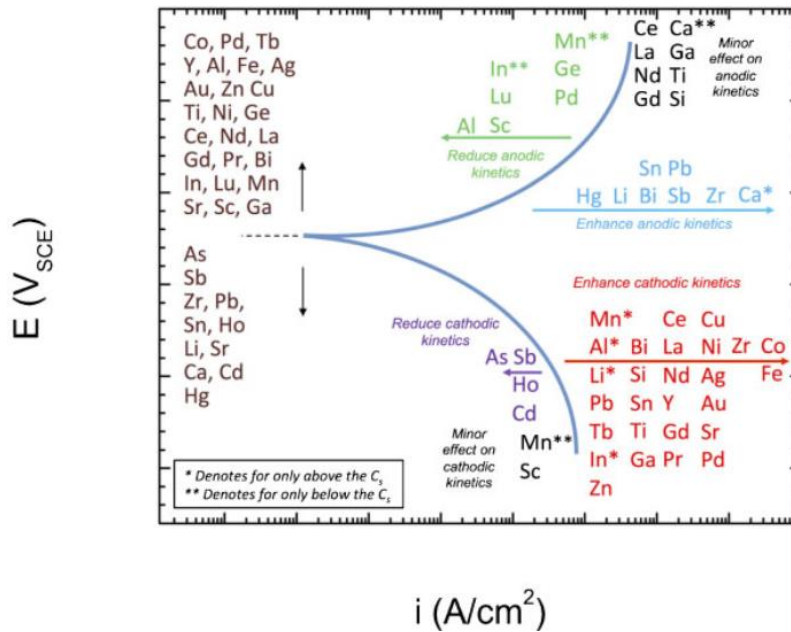
Figure 2.14 Effect of alloying elements on the electrochemical properties of Mg [54].
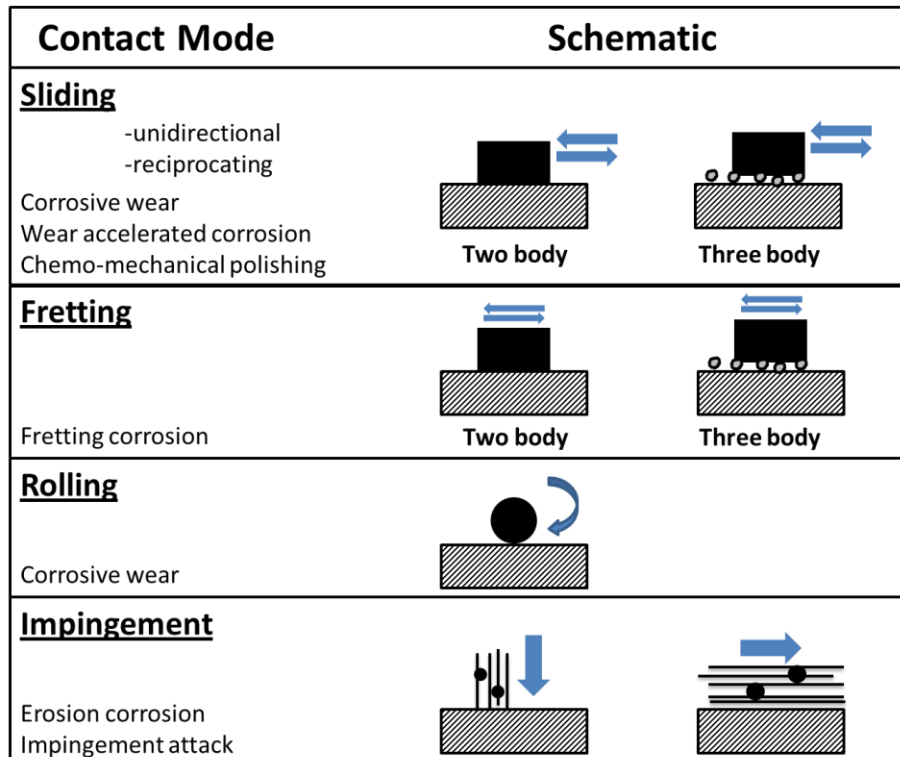
Figure 2.15 Schematics of the different types of tribological contacts during tribocorrosion [96].
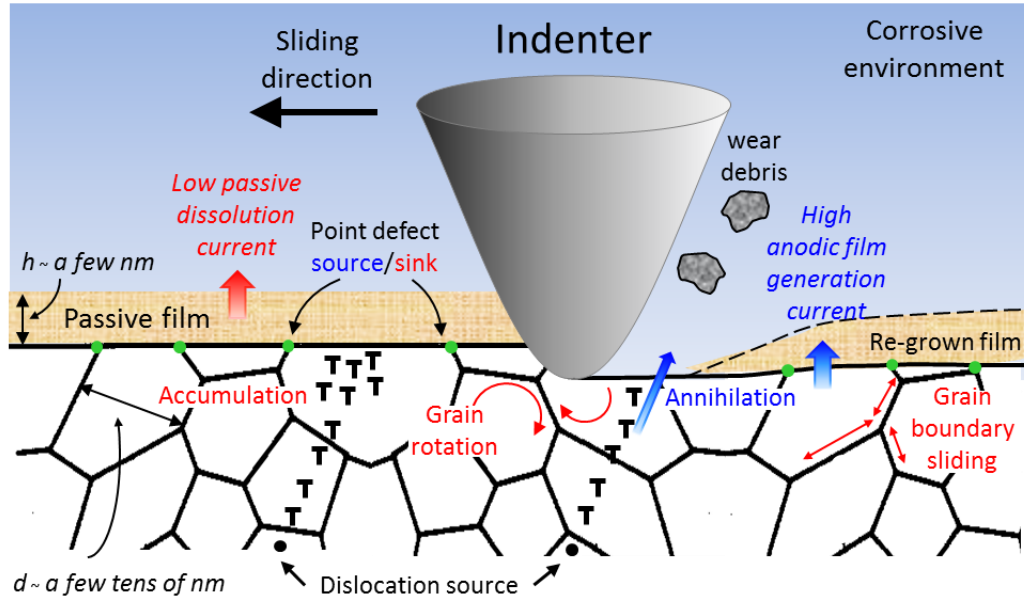
Figure 2.16 Schematic presentation of relevant mechanisms influencing the tribocorrosion of passive metals and alloys.

CHAPTER 3: EFFECT OF ALLOY CONCENTATION ON THE CORROSION

RESISTANCE OF AL AND AL-MN THIN FILMS [1]

3.1 Introduction

Aluminum (Al) films are frequently applied as a corrosion protection coating for steel [4, 5], magnesium alloys [6, 7], and NdFeB magnets [8] etc., replacing the toxic cadmium coatings [9]. Al coatings can be deposited using various methods including electroplating [4], physical and chemical vapor deposition [6, 113], and hot-dipping [5]. An amorphous semiconducting passive film forms on the surface of Al in neutral (pH 4-9) solutions to protect the metal underneath from corrosion [46, 114]. However, this passive film is still vulnerable to local attack from different halide ions in saline environments, which eventually leads to pitting and crevice corrosion of Al. In addition to its pitting susceptibility, the low mechanical strength of Al coating also leads to poor wear resistance, which greatly limits its potential usage in industrial applications where mechanical contact and corrosive environment coexist [41].

Alloying has been found to be a highly effective method to strengthen Al by forming precipitates or secondary particles [40]. However, the presence of precipitation and secondary particles enhances corrosion by catalyzing oxygen reduction, increasing the alloy corrosion potential, and localizing the electrochemical activity due to chemical inhomogeneity from the Al matrix [41]. Recent studies show that alloying can increase the pitting potential (E_{pit}) of Al

---

provided that the alloying elements are retained in solid solution [42-45]. For example, age-hardened 2000 series Al alloys (with Cu as the major alloying element) exhibit poor corrosion resistance [41], but Kim et al. observed an ennoblement of E_{pit} with increasing Cu content in Al-Cu solid solutions [42, 43]. Alloying Al with appropriate transition metals (TMs) such as Mo, Mn, W, Nb, Cr, Ta, V, and Zr in metastable solid solutions offers the possibility to significantly enhance its pitting resistance in chloride solutions [37]. These TMs improve corrosion resistance and decrease pitting susceptibility of Al by increasing the overpotential for anodic dissolution and decreasing metastable pit initiation and growth rates [42]. In addition, alloying is an effective way to minimize grain size and produce nanocrystalline microstructure. These refined microstructures are likely to promote passive film growth due to the high density of point defect sinks and sources at the intersection between grain boundaries and the film/metal interface [46, 47].

Al-Mn is chosen in the present work as a model system to investigate the effects of alloy concentration and microstructure on the corrosion resistance of Al-TM solid solution thin films. This binary system exhibits a wide range of equilibrium phases from solid solution to more than nine intermetallics [115]. Such rich variety of phases indicates the possibility of forming tunable nanostructures by adjusting the alloying concentration [116, 117]. Unlike Mo, Ta, Cr, etc. which improve the pitting resistance of Al by increasing the solute concentration in the passive layer that impede the ingress of chloride ions, Mn is found to be absent from the passive film of Al-Mn in chloride solutions [118, 119]. Instead, it was suggested that Mn solute atoms improve the pitting resistance by hindering the pit growth kinetics of Al [109, 118]. Despite these past studies, findings on how alloying concentration affects the corrosion resistance of Al-Mn are not fully consistent. Moffat et al. [118] investigated the corrosion resistance of Al-Mn alloys with 0

– 26 at.% Mn electrodeposited at 150 $^{\circ}$C. They found that E_{pit} is greatly increased for crystalline (0 – 5 at.% Mn) and amorphous (22 – 26 at.% Mn) Al-Mn but decreased at the intermediate composition (5 – 22 at.% Mn) where crystalline and amorphous phases coexist. On the other hand, Frankel et al. [109]found alloying with Mn enhanced pitting resistance of Al but both the pitting and repassivation potentials of Al-Mn alloys were not strong functions of Mn concentration. In addition, their work did not include characterization of the alloy microstructure or pit morphology. Recently, Reffass et al. [120] showed that the E_{pit} increases monotonically with alloying concentration up to 32 at.% Mn while the corrosion current density remain insensitive to alloy composition. Given the variability and limitations of prior findings noted above, the present work aims at evaluating the composition-corrosion resistance relationship by investigating the role of Mn on the microstructure and corrosion resistance of Al-Mn solid solutions. Attention is given to the microstructure and surface morphology of as-deposited and corroded samples toward better understanding the roles of composition as well as microstructure on corrosion resistance.

3.2 Experimental Procedure

The equilibrium solubility of Mn in Al at room temperature is low, ~ 0.62 at.% [121], so nonequilibrium processing techniques are needed to achieve extended solubility. Physical vapor deposition (PVD) with its associated high quench rates was chosen here to produce supersaturated Al−Mn alloys with crystalline, dual phase, and amorphous microstructure. Pure Al and Al-Mn alloys with 5.2, 11.5, and 20.5 at.% Mn were sputtered on Si wafer using a CRC sputter coater at 80 W radio frequency power under Ar (99.99%, 5 mTorr) atmosphere. To produce Al-Mn alloys, an Al (99.99%) sheet with uniformly spaced holes was placed over a Mn (99.999%) disc and used as the target, 6 cm away from the specimen. The number and size of the

holes on the Al sheet was varied to achieve different alloy compositions. Post deposition chemical analysis confirmed the formation of compositionally homogenous films over the entire sample size of 1.2 X 2 cm^2. Prior to deposition, the Si wafers were etched with 1:50 hydrofluoric acid water solution to remove the native oxide layer to improve coating adhesion. Both Al and Al-Mn were deposited with a nominal film thickness of ~ 1 μm, confirmed using a Detak 3030 ST profilometer. All experiments were performed on as-deposited samples without any pretreatment.

The as-deposited samples were characterized using scanning electron microscopy (SEM, Hitachi SU-70), energy-dispersive X-ray spectroscopy (EDS, EDAX-Phoenix attached to SEM, Hitachi S-800), and grazing incidence X-ray diffraction (XRD, PANalytical X'Pert). Transmission electron microscopy (TEM) analysis including bright-field (BF), dark-field (DF) imaging, and selected area diffraction (SAD) was performed using Tecani F20 TEM. TEM samples were prepared by directly sputtering Al and Al-Mn alloys on continuous carbon film TEM grids for 15 min, which resulted in a sample thickness of ~150 nm.

Electrochemical behavior was characterized at regimes of mild and severe environmental exposure, consisting respectively of naturally aerated 0.01 and 0.6 M NaCl aqueous solutions, both pH ≈ 6.4 and at ambient temperature. The evaluations were conducted in 3-electrode cells where the deposited samples, a mixed metal oxide coated titanium mesh, and a commercial silver-silver chloride electrode (1 M KCl internal solution) were used as the working, counter, and reference electrode respectively. Prior to the corrosion tests, the sample surfaces were covered with stop-off lacquer except to expose a square region with an effective surface area of 1 cm² to the electrolyte, and another region allowing for an electrical contact using an alligator clip. Optical microscopy was performed after each test and results from samples that showed

any indication of crevice corrosion under the stop-off lacquer were discarded. The results reported here for each test condition correspond to at least three separate tests without crevice corrosion. All tests were conducted with a Gamry Reference 600® potentiostat.

In the severe 0.6 M NaCl regime, in addition to open circuit potential (E_{oc}) determinations only short-term solution potentiodynamic polarization (PD) measurements were conducted, after allowing 1 hr of immersion for E_{oc} to approach a stable regime. The PD scans were conducted in the anodic direction at a rate of 0.167 mV/s, starting from a potential ~150 mV more negative than E_{oc}. The scans were terminated when a rapid increase in the anodic current density took place and reached 10 $\mu A \cdot cm^{-2}$. Given the low current densities and solution resistivity involved, no correction was made for solution resistance effects in these tests. The potential at which that rapid increase took place was named E_{pit}. A nominal value of the cathodic polarization slope (β_c) was assigned by fitting a straight line to the portion of the polarization curve that corresponded to potentials more than 50 mV lower than E_{oc}. A nominal value of the anodic polarization slope (β_a), was likewise assigned, using the portion of the curve that started at potentials > 50 mV higher than E_{oc} and ended at E_{pit}. Extrapolation of both of those trends to E_{oc} and suitable averaging of both was used to obtain a nominal corrosion current density (i_{corr}). The i_{corr} was converted to a nominal corrosion rate in ($\mu m/y$) by Faradaic conversion (1 $\mu A.cm^{-2} \approx 10.9$ $\mu m/y$) treating the corrosion as if it were uniform with formation of Al^{+3}. It is noted that unless indicated otherwise current densities and associated corrosion rates are reported as a value averaged over the nominal area of the specimen, recognizing that corrosion rates at localized features may be much larger. Hence, the reported values of corrosion rates in $\mu m/year$ are considered as a rough estimation and are used only for comparing the corrosion resistance of Al-Mn with various Mn%. The unit of corrosion rate ($\mu m/year$) is chosen

37

here to be consistent with that commonly adopted in the literature. However it should be noted that the corrosion experiments performed here were over a much shorter period of time than one year. The reported polarization slopes may reflect passive film properties and ohmic components due to current localization, and are not viewed as representing simple Tafel behavior. Likewise, the potential E_{pit} has been named so by analogy to the behavior observed upon pitting in bulk specimens, but the morphology of localized corrosion in these thin films may differ from that of conventional pits, as discussed later on.

In the milder, 0.01 M NaCl regime E_{oc} and PD measurements were conducted in selected specimens following the same methodology as for the 0.6 M NaCl exposures. The milder conditions enabled longer term evaluations, so with another set of specimens, E_{oc} measurements were conducted regularly over periods of up to 108 hours, supplemented by non-destructive electrochemical impedance spectroscopy (EIS) tests via 10 mV *rms* sinusoidal potential excitation around E_{oc} in the frequency range of 10 mHz to 100 kHz, 5 points per decade. Analysis of the EIS results, described further below, was conducted to obtain a nominal value of i_{corr} as function of exposure time. Finally, corrosion tests results plotted in the all figures here are averages of at least three data points with error bars representing the range of the data. SEM examination was conducted on one of the exposed specimens of each alloy after extraction from the test solution for the longer duration tests. Post-corrosion cross-sectional samples were prepared from areas exposed to the corrosive environment using focused ion beam microscope (FIB, Quanta 200 3D Dual Beam).

3.3 Results and Discussion

3.3.1 Materials Characterization

EDS chemical analysis with spatial resolution of ~200 nm, confirmed the formation of compositionally homogeneous Al-Mn alloy films with 5.2, 11.5, and 20.5 at.% Mn, hereafter noted as alloy A5, A11, and A20, as listed in Table 1. The average oxygen concentration measured for all alloys was 0.62 ± 0.17 at.%. SEM images of as-deposited Al (A0) and Al-Mn alloys are shown in Fig. 3.1. From alloy A0 to alloy A20, the surface morphology became smoother, indicating the formation of finer microstructures (e.g. smaller grain size and/or greater content of amorphous phase) at higher alloying concentration. The faceted angular structures of alloy A0 and alloy A5 indicate the formation of crystalline phases where each angular structure often corresponds to an individual grain [122]. Surfaces of alloy A11 and alloy A20 exhibited compact round nodules, similar to those observed in thin films with ultrafine grains and/or high amount of amorphous phase [123].

To establish the phase nature of the deposits, grazing-incidence angle XRD line scans were performed on a sample of each alloy. The results are shown in Fig. 3.2. The diffraction pattern of alloy A5 was characteristic of a face-centered-cubic (fcc) crystalline structure, similar to that of pure Al (A0), indicating the formation of super-saturated solid solution well beyond the equilibrium solubility. For the alloy A11, broad fcc diffraction peaks and a hint of a diffuse peak at $2\theta \approx 42°$ were observed, indicating that an amorphous phase coexisted with α-Al. At the highest alloying concentration, the alloy A20 was completely amorphous, where all crystalline diffractions were absent and only a broad hump around $2\theta \approx 42°$ was observed. In addition to peak broadening, a right shift of the (111) diffraction peaks was observed from alloy A0 to alloy A11, indicating a decrease of lattice constant (as listed in Table 1) with increasing alloying

concentration. This behavior is similar to that reported for electrodeposited Al-Mn [116], suggesting that Mn, which has a Goldschmidt radius ~ 11% smaller than Al, is substitutionally incorporated into the Al lattice.

Bright-field TEM imaging and selected-area diffraction (SAD) analysis were performed to reveal the detailed microstructure of the as-deposited samples, as shown in Fig. 3.3. The average in-plane grain size of alloy A0, A5, and A11 was 42, 15, and 12 nm respectively, measured using the line-intercept method from both bright-field and dark-field TEM images. The SAD patterns showed that both alloy A0 and alloy A5 exhibited discrete diffraction rings associated with single fcc phase (Fig. 3.3(a-b) insets). A diffuse halo and sharp diffraction rings coexisted in the SAD pattern of alloy A11, confirming the presence of a dual-phase microstructure, in agreement with the XRD results. High-resolution TEM images (Fig. 3.3(d)) of alloy A20 indicated the absence of short-range-order, and the halo ring of the corresponding SAD pattern confirmed the amorphous nature of this alloy. In summary, by tuning the Mn content in the alloy from 5.2 to 20.5 at%, a microstructure transition from nanocrystalline, dual-phase, to complete amorphous phase was achieved.

3.3.2 0.6 M NaCl-Short Term Exposures

Representative PD results in this more aggressive electrolyte are shown in Fig. 3.4. The crossover potentials for zero current (Ezero current) agreed reasonably well with the values of Eoc observed before initiating the scans. Pure Al (A0) showed highly active dissolution immediately on entering the anodic current regime, while all Al-Mn alloys showed regions of predominantly passive behavior (likely with some extent of localized activity), followed by a rapid increase in current density at Epit. Additional tests which included a return scan confirmed that the increase in current was associated with permanent corrosion damage by showing a wide

return loop and lateral propagation of a metal loss front revealing the silicon substrate. The Eoc values and the electrochemical parameters obtained from PD measurements are shown in Fig. 3.5 and Table 3.2. Epit increased monotonically with Mn content. This observation is similar to that of Moffat et al.[118]. At the Eoc all Al-Mn alloys exhibited lower nominal corrosion rate compared to pure Al, consistent with the latter being in a distinct active dissolution pitting regime, while the others approached a passive condition. The amorphous Al-Mn (alloy A20) exhibited the smallest nominal corrosion rate, 0.9 µm/year. Ezero current of nanocrystalline (alloy A5) and complete amorphous (alloy A20) Al-Mn were both anodic compared to that of pure Al (A0). However Ezero current of the dual-phase (alloy A11) was more cathodic, -750 mVAg/AgCl.

3.3.3 0.01 M NaCl-Short and Long Term Exposure

Representative PD results in this milder electrolyte are shown in Fig. 3.6. The IR drop in this electrolyte is estimated to be less than 2 mV thus is neglected here. As for the other electrolyte, the crossover potentials for zero current agreed reasonably well with the values of E_{oc} observed before initiating the scans. Despite the milder electrolyte, Alloy A0 showed highly active dissolution immediately on entering the anodic current regime as it did in the 0.6 M NaCl tests. The Al-Mn alloys, which had shown indications of an initially passive condition in 0.6 M NaCl did as expected the same in 0.01 M NaCl. Unlike in the more severe environment however, none of the Al-Mn alloys in 0.01 M NaCl showed clear indication of onset of pitting even when anodically polarized up to +0.8 V as shown also in (Fig. 3.7(a)). The E_{oc} values and the electrochemical parameters obtained from PD measurements are shown in Fig. 3.7 and Table 3.3. Compared to that of pure Al (A0), the $E_{zero\ current}$ of nanocrystalline (alloy A5) was more cathodic; however it was more anodic for the dual-phase (alloy A11) and the complete

41

amorphous (alloy A20). The E_{OC} of the nanocrystalline (alloy A5) was more cathodic compared to that of pure Al. Similar to the behavior in the more aggressive electrolyte, all Al-Mn alloys exposed to the milder electrolyte exhibited lower nominal corrosion rate compared to pure Al. The amorphous Al-Mn (alloy A20) exhibited the smallest nominal corrosion rate, 0.7 µm/year.

For the long term tests Fig. 3.8 shows that the E_{oc} of pure Al was always more negative than that of all Al-Mn alloys, shifting towards more negative values as exposure time increased and reaching ~ -900 $mV_{Ag/AgCl}$ at 24 hrs. This evolution was indicative of stable local passivity breakdown even in this relatively mild environment, and was confirmed by direct observation as shown in Fig. 3.9 where through thickness macroscopic pits are clearly seen. Given this early manifestation of corrosion, the Al specimens were removed from the solution at 24 hrs.

In contrast to pure Al, the three Al-Mn alloys showed nobler E_{oc} values generally indicative of a predominately passive regime [120]. E_{oc} values started at around -450 to -550 $mV_{Ag/AgCl}$. For alloys A11 and A20, E_{oc} shifted towards more negative values around -750 to -800 $mV_{Ag/AgCl}$ for up to 24 hrs but became increasingly nobler from then on, suggesting a period of some activity but eventually the development of a more stable passive regime [120]. Alloy A5 showed a consistently elevated value of $E_{oc,}$ around -450 $mV_{Ag/AgCl}$ over the entire exposure period suggesting stable passive behavior from the onset. After about 90 hrs of immersion, the E_{oc} values for all three Al-Mn alloys tended to be comparably noble, similar to behavior observed by Refass et al indicative of predominantly passive conditions [120]. This interpretation was consistent with visual observation that showed no macroscopic pitting on any of the three Al-Mn alloys after 108 hrs of immersion, as exemplified in Fig. 3.9 for alloy A20.

EIS (Fig. 3.10) provided further insight on the relative corrosion resistance of the alloys evaluated. The Nyquist diagrams show a prominent high frequency semicircle followed by the

42

onset of another at lower frequencies. This behavior was interpreted tentatively here with the treatment proposed by Akhoondan [124] by fitting the results to the impedance projected by the equivalent circuit and parameters shown in Fig. 3.11. There R_s represents the ohmic solution resistance, which was found, as expected, to be of a value consistent with the cell dimensions and electrolyte resistivity and independent of the material tested. The interfacial impedance is assumed to consist of a nearly ideal capacitive element (CPE_1, with impedance represented by $Z_{CPE} = Y_o^{-1} (j\omega)^{-n}$ where Y_o is a constant, $j = (-1)^{1/2}$, ω is the angular frequency and n is a real number between 0 and 1), representative of the capacitance of the passive film, in parallel with components representing the impedance associated with the Faradaic reactions on the interface. Those processes consist of some form of anodic dissolution, either via slow ionic transport through the bulk film or at discrete film flaws, and a cathodic process that is likely to involve oxygen reduction given the aerated solution condition, and expected to take place preferentially at localized film imperfections. In the adopted interpretation [124] the impedance components of both reactions are assumed to be acting in parallel, but the one for the anodic reaction is taken as being large enough to be neglected given the high polarizability of that reaction in a predominantly passive metal. The remaining dominating impedance, that of the cathodic reaction, may be viewed as being responsible for the observed two-loop behavior by proposing that it reflects the presence of a two-step cathodic process [124]. In such treatment the impedance can be represented by a fast-reacting term R_{ct}, and a slower reacting component corresponding to the parallel combination of R_2 and CPE_2, with R_{ct} as a charge transfer resistance that is approximately related to the surface-averaged corrosion current density on the sample by Stern-Geary equation [125].

$$i_{corr} = B/R_{ct} \tag{3.1}$$

where B has a value of 52 mV, in the order of those commonly assumed for the Stern-Geary constant of predominantly passive metals [126]. The equivalent circuit produced simulations that closely matched the experimental behavior for much of the frequency range sampled, as shown by the solid lines in Fig. 3.10. The evolution of equivalent circuit parameters as a function of immersion time is shown in Fig. 3.12, which also indicates that reasonably similar trends were obtained with multiple replicate specimens.

As illustrated in Fig. 3.10, the high frequency semicircle was only moderately depressed, which on analysis yielded generally elevated values of the CPE parameter n as shown in Fig. 3.12(c). That was especially so at the beginning of the exposure with n ~0.91 for Alloy A5 and only somewhat smaller values for the other alloys. Under those conditions the CPE parameter Y_o may be viewed as a rough estimate of the film capacitance C via

$$C \sim Y_o \cdot sec^{n-1}, \tag{3.2}$$

recognizing that the expression becomes increasingly inaccurate as n decreases from unity [127]. From there, a nominal thickness of the passive film (d) may be obtained from the following equation [128]

$$d = \varepsilon\varepsilon_o A/C, \tag{3.3}$$

where ε is the dielectric constant of the passive film (taking it to be ~10 for aluminum oxide [129]), ε_o is the permittivity of vacuum (8.85×10^{-14} F·cm^{-1}) and A is the exposed surface area (~1 cm^2). As shown in Fig. 3.12(d), the passive film thickness (d) for all alloys at early ages was in the range of ~1–1.5 nm. Those values are comparable to those reported in other investigations for films resulting from natural air oxidation of Al alloys [124, 128], thus supportive of the interpretation of the nature of the reactive term responsible for the high frequency semicircle. Per

Fig. 3.12(b-c) the values of n and Y_o for Alloy A5 remained close to 0.9 and 8 10^{-6} F sec$^{(1-n)}$

respectively during the entire exposure period, suggesting that the passive film thickness was

not changing much with exposure time. For the other alloys the values of n and Yo experienced

moderate decreasing and increasing trends respectively. The corresponding values of d remained

not far from those experienced initially. Further interpretation of any apparent trends of changes

in d with time was not attempted, as they may merely reflect artifacts from data scatter and the

increasing uncertainty in the applicability of Eq. 3.2 associated with decreasing values of n.

As shown in Fig. 3.12(a) the values of nominal corrosion rate (estimated from EIS via

Eq. 3.1 were consistently the lowest (by about one order of magnitude over much of the exposure

period) for Alloy A5 than for the others. Alloy A20 had a brief initial period of low nominal

corrosion rate but rapidly approached the values for A0 and A11 afterwards. Alloy A0 had the

highest nominal corrosion rate, consistent with the early conspicuous surface deterioration

illustrated in Fig. 3.9.

3.3.4 Microstructure and Electrochemical Behavior

Fig. 3.13(a) summarizes the average nominal corrosion rate estimates from PD and EIS

tests of all the alloys as a function of Mn% in both test environments and time frames

investigated. While the estimates were conducted using different techniques and working

assumptions, both methods still indicate as expected [130] corrosion severity that increased with

increasing [Cl$^-$]. It is also noted that despite the 60-fold change in [Cl$^-$], the short term results

show similar ranking in nominal corrosion rate, with A5 and A20 exhibiting the slowest and A0

and A11 the highest nominal corrosion rates by roughly the same proportions. In the long term

0.01 M NaCl solution evaluation, alloy A5 showed the best indications of passive film stability

of all alloys evaluated, with consistently noble E_{oc} values (Fig. 3.8), lowest (although somewhat

increasing with time) nominal corrosion rate, well defined indications of retaining the initial passive film thickness throughout the entire period of exposure, and as shown later visual absence of localized corrosion after 108 hrs.

The behavior in 0.6 M [Cl⁻] allows comparison with work of others also performed in comparably aggressive solutions. The relatively high nominal corrosion rate found here for the dual phase alloy as compared to its nanocrystalline or amorphous Al-Mn counterparts is similar to that reported by Refass et al. [120], Merl et al. [105] and Sanchette et al. [44]. It is likely associated with local galvanic coupling between the crystalline and amorphous phases due to their expected different electrochemical properties. Indeed, phase heterogeneity as a potentially source of local galvanic coupling has already been reported in Al- [131] and Zr-based [132] metallic glasses. For example, Li. et al. [132] found that partially crystallized $Zr_{65}Al_{7.5}Cu_{17.5}Ni_{10}$ alloy experienced accelerated dissolution compared to its crystalline or complete amorphous counterparts, as a result of high chemical activity at the crystalline-amorphous interfaces and grain boundaries.

To clarify the correlation between composition and microstructure and how their interplay affect corrosion resistance in the more aggressive media, Fig. 3.13(b) summarizes the evolution of E_{pit} as a function of Mn content and microstructure from the current work and previous reports [109, 118, 119]. Red, green, and blue symbols are used to represent crystalline, dual phase, and amorphous microstructure respectively. It can be seen that the addition of Mn up to 10 at% was highly effective in improving pitting resistance (as inferred from the value of E_{pit}) in 0.1–0.86 M chloride solutions. This effect was less significant at higher compositions (beyond ~ 20 at. %) when Al-Mn becomes completely amorphous. This overall trend is consistent with observations by Frankel et al. [109], where pitting corrosion of Al-Mn was not much sensitive to

alloy concentration in the range of ~ 6 – 16 at. Mn%. A deviation from this general trend is apparent in the dual phase region from the results by Moffat et al. [118]. However, this deviation is not surprising given the fact that Moffat et al. deposited Al-Mn at an elevated temperature of ~ 150 $^{\circ}$C which promote large chemical inhomogeneity between the fcc and amorphous phase. They noted that the composition of the selectively dissolved fcc phase is ~ 1 at.% Mn, very close to the equilibrium solubility limit. All other data (including our results) in Fig. 3.13(b) were obtained from Al-Mn deposited at room temperature which favors the formation of the compositionally homogenous dual phase microstructure. This chemical homogeneity was also confirmed by Ruan et al. [133] using atom probe tomography (APT). They found that Mn solute atoms distributed homogenously in the Al matrix with no significant clustering or ordering at the grain boundaries or in the amorphous phase, for either pure crystalline or dual phase Al-Mn. Taken together, in chemically homogenous Al-Mn solid solutions, pitting potential is seen to increase monotonically with alloying concentration regardless of the microstructure and phase of the alloy.

3.3.5 Exposed Surface Morphology

Fig. 3.14 shows SEM examination of the exposed alloys (one sample each) for any significant surface features after the 0.01 M NaCl immersion. Pure Al (A0) clearly showed through- thickness circular "pits" ~120 μm in diameter after 24 hrs of immersion; this observation is consistent with the direct visual observation of local corrosion (Fig. 3.9) and the indication of an anodic current surge immediately after exceeding the freely corroding potential (Fig. 3.6). Up to 108 hrs of exposure the surface of both alloys A5 and A11, while showing some alteration compared with the as-deposited state (Fig. 3.1) did not however reveal any marked localized attack. In contrast, a network of conspicuous grooves developed on alloy A20, as

shown in Fig. 3.14(d). Al and Mn EDS maps of the corroded surface (Fig. 3.14(d) insets) were featureless, so the grooves did not seem to be associated with any local compositional inhomogeneity. To reveal the depth of the grooves, a cross-section of the sample was prepared by focused ion beam (FIB) milling (Fig 3.15). Edge rounding and overhanging milling debris introduce some uncertainty, but in general the grooves appeared to be in the order of ~100 nm or less in depth (the depth of the grooves was measured by tilting the sample by 40°).

Besides the grooves, a large population of circular pit-like features ~ 100 nm in diameter was observed as well (white arrows, Fig. 3.15), resembling those observed in electrodeposited amorphous Al-Mn (with 21 at.% and 26 at.% Mn). Closer examination indicated that these features had a tendency to be connected with the groove network as illustrated by the red arrows in box 2, Fig. 3.15. The features may be vestigial traces of metastable pits; Meng et al. [134] demonstrated that the possibility of forming small metastable pits was higher for Al with smaller grain sizes. This grain size dependency is generally consistent with our observation that micrometer-scale stable pits are only observed in pure Al, while these apparent metastable pits were observed on our amorphous Al-Mn alloy.

It is of interest to compare with the SEM evidence the amount of metal dissolution estimated from the EIS apparent corrosion rate test results. From the nominal corrosion rates in Fig. 3.12(a) alloys A11 and A12 would have had experienced after 108 hours, if the wastage was uniform, a deposited layer thickness loss in the order of ~ 200 nm, or about 20% of the initial film thickness. As indicated earlier, the interpretation of the EIS data is based only on working assumptions so only a rough estimate of material loss can be expected. Nevertheless the estimated value is consistent with the SEM indication of the initial film having been still present after 108 hours in both alloys. The EIS estimate also suggests that if in the case of the A20 alloy

the comparatively shallow grooves should be mostly irregularities in an advancing, relatively generalized front of metal wastage; otherwise the grooves would have needed to be much deeper to account for the metal loss estimate. Resolution of this issue merits consideration in subsequent investigations. For alloy A5 the metal loss estimate is about one order of magnitude less than for its two counterparts, fully consistent with the deposit still being in place and the absence of any other microscopic evidence of strong surface alteration. In all Al-Mn alloy cases the relatively sustained value of the passive film thickness indicated by the EIS data suggests that it was being globally regenerated while any metal wastage was taking place.

3.4 Summary of Findings

Al and Al-Mn thin films with up to 20.5 at.% Mn were grown by PVD on Si substrates to evaluate the influence of Mn on microstructure formation as well as their short-term and long-term corrosion behavior. At low Mn concentration (5.2 at.%), Mn and Al form a supersaturated face-centered cubic solid solution with an average grain size of 15 nm. At an intermediate Mn concentration (11.5 at.%), a chemically homogenous dual-phase microstructure was formed consisting of fcc and amorphous Al-Mn. Further increasing alloy concentration to 20.5 at.% Mn leads to the formation of a complete amorphous Al-Mn with reduced surface roughness.

For the microstructures examined here Mn was found to be highly effective in improving the corrosion resistance of Al. The pitting potential increased monotonically with the alloying concentration and was insensitive to the microstructure as long as chemical homogeneity was attained. The alloys containing fully nanocrystalline (5.2 at.%Mn) and fully amorphous (20.5 at%Mn) microstructure exhibited better corrosion resistance than those containing dual phase (11.5 at%Mn). Finally, the amorphous Al-Mn was found to exhibit the highest corrosion resistance at short exposure time in chloride solution while the nanocrystalline counterpart was

more stable over long exposure time up to 108 hrs. Post-corrosion surface characterization revealed a network of surface grooves and circular pits formation on the amorphous Al-Mn after 108 hrs.

As a last note, the enhanced corrosion resistance and decreased pitting susceptibility of Al by alloying with Mn is similar to that observed in other Al-TM (TM=Ta, Mo, Cu, W, etc.) systems. A possible contribution to the enhanced pitting resistance by alloying with Mn is that Mn alters the pit growth kinetics [109]. Since Mn^{2+} has a lower hydrolysis constant than Al^{3+}, thus a higher dissolution rate is required for Al-Mn to maintain the pH necessary for pit growth than pure Al. Finally, while the current study focused on Al-Mn thin films deposited on Si substrate by PVD, this material system can be easily electrodeposited in much thicker coatings (at a deposition rate of ~ 10 – 20 μm/hr [116, 135]) to protect various metal substrates such as Al alloys, steel, and Mg alloys.

Table 3.1 Summary of composition and microstructure results of as-deposited Al and Al-Mn alloys.

Alloy ID	Mn concentration (at.%)	Lattice constant (Å)	TEM grain size (nm)	Phase
A0	0	4.047	42	nanocrystalline
A5	5.2	4.036	15	nanocrystalline
A11	11.5	4.035	12	nanocrystalline + amorphous
A20	20.5	-	-	amorphous

Table 3.2 Electrochemical parameters from PD tests of Al and Al-Mn alloys in 0.6 M NaCl. Values shown as average (range).

Alloy ID	β_a (V/decade)	β_c (V/decade)	Nominal i_{corr} (A/cm²) X10^{-7}	E_{oc} (mV)	Nominal Corrosion Rate (µm/year)	E_{pit} (mV)
A0	-	0.75 (0.17)	8.3 (3.0)	-730 (105)	9.1 (3.3)	-640 (12)
A5	0.23 (0.17)	0.23 (0.10)	0.9 (0.3)	-450 (64)	1.0 (0.4)	-276 (16)
A11	0.67 (0.16)	0.52 (0.25)	4.3 (3.2)	-810 (110)	4.7 (3.5)	-206 (15)
A20	0.35 (0.05)	0.31 (0.26)	0.8 (0.4)	-564 (62)	0.9 (0.5)	-110 (54)

Table 3.3 Electrochemical parameters from PD tests of Al and Al-Mn alloys in 0.01 M NaCl. Values shown as average (range).

Alloy ID	β_a (V/decade)	β_c (V/decade)	Nominal i_{corr} (A/cm²) X10^{-7}	E_{oc} (mV)	Nominal Corrosion Rate (µm/year)	E_{pit} (mV)
A0	-	0.28 (0.29)	1.90 (0.50)	-487 (9)	2.1 (0.5)	-419 (38)
A5	0.28 (0.15)	0.21 (0.09)	1.05 (0.08)	-349 (93)	1.1 (0.2)	-
A11	0.49 (0.31)	0.30 (0.11)	1.18 (0.30)	-503 (106)	1.3 (0.3)	-
A20	0.39 (0.26)	0.24 (0.08)	0.66 (0.58)	-466 (172)	0.7 (0.6)	-
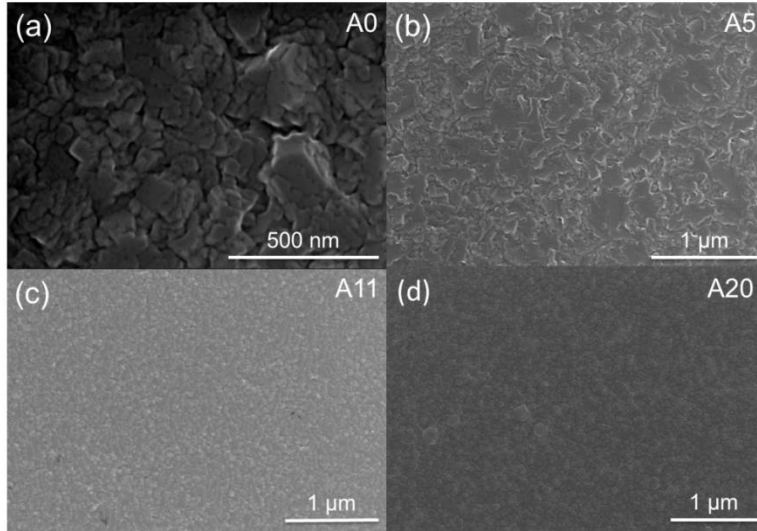
Figure 3.1 Surface SEM images of as-deposited (a) Al, (b) Al-5.2at% Mn, (c) Al-11.5at% Mn, and (d) Al-20.5at% Mn.
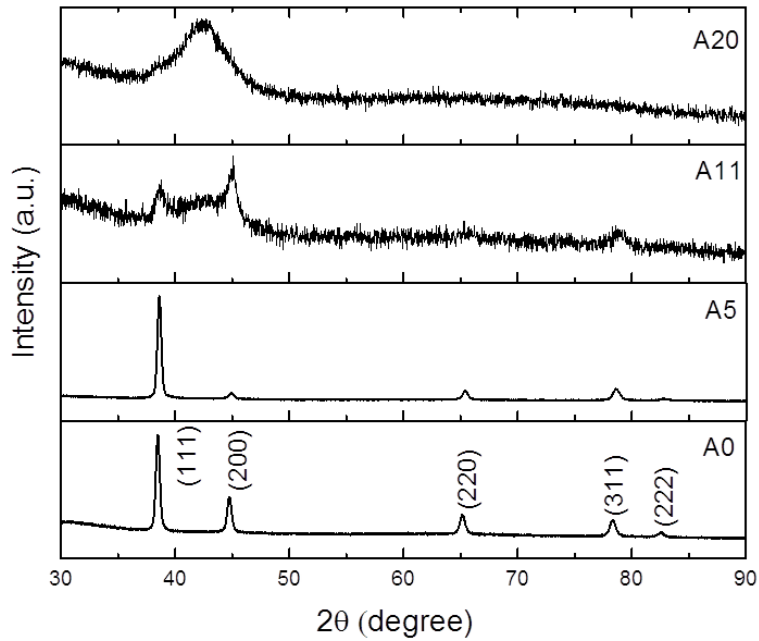
Figure 3.2 XRD line scans of as-deposited Al and Al-Mn alloys.
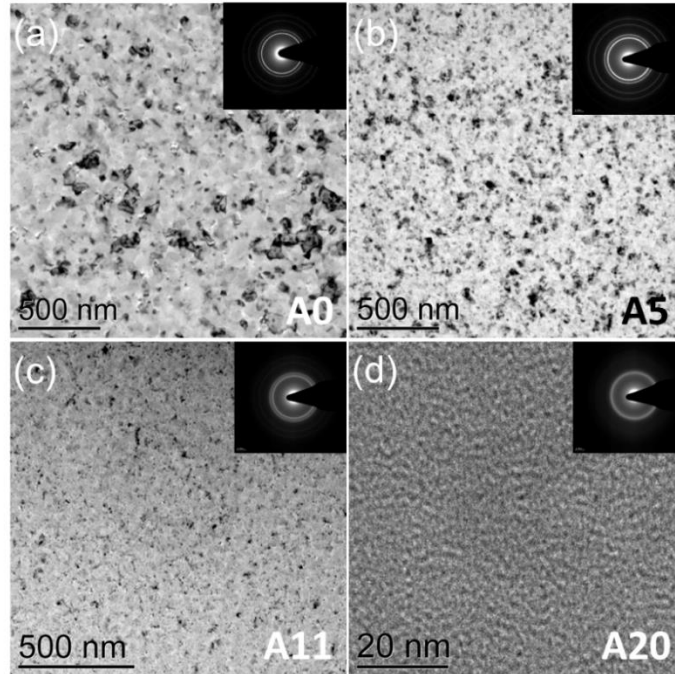
Figure 3.3 Bright field TEM images and selected area diffraction (SAD) patterns (insets) of as-deposited (a) Al, (b) Al-5.2at% Mn, (c) Al-11.5at% Mn, and (d) Al-20.5at% Mn.
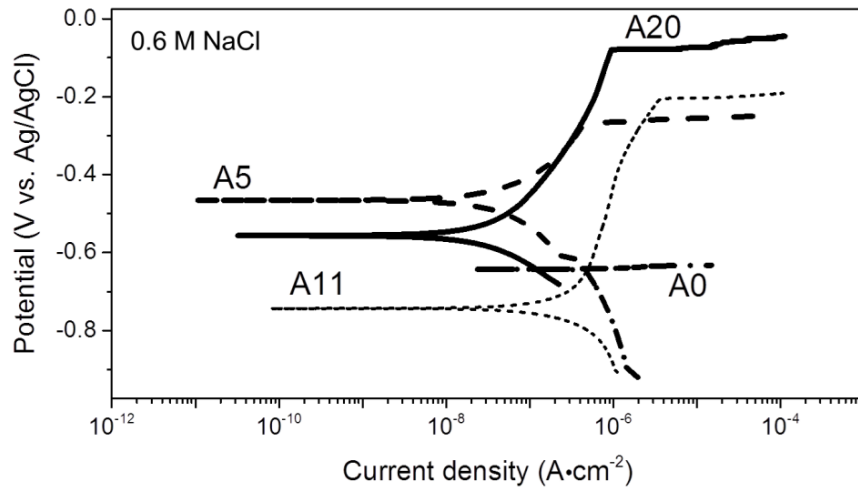
Figure 3.4 Typical potentiodynamic polarization curves of Al and Al-Mn alloys after 1 hour immersion in 0.6 M NaCl solution.
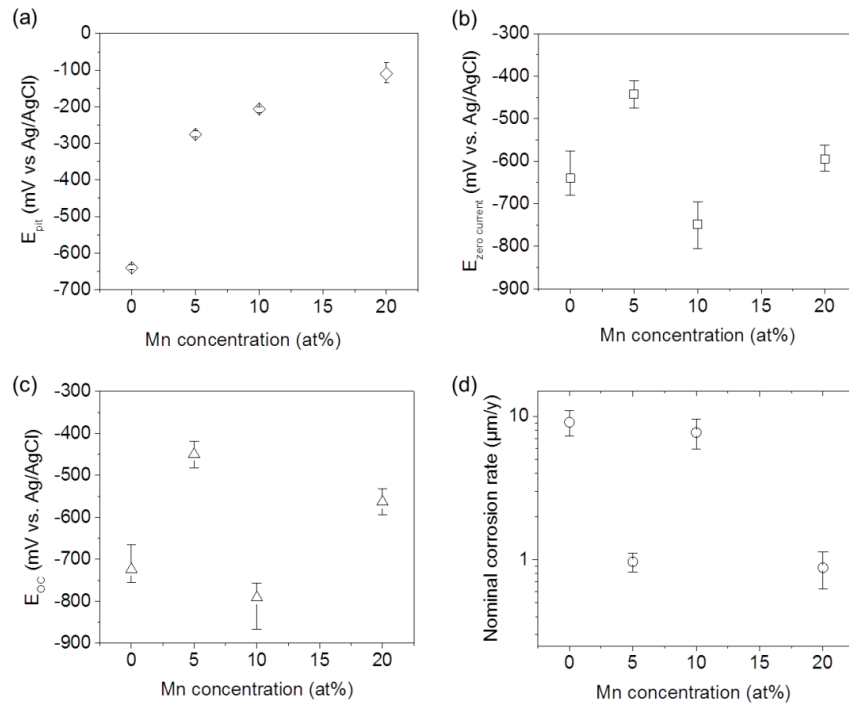
Figure 3.5 Electrochemical parameters (a) Epit, (b) Ezero current, (c) Eoc, and (d) Nominal corrosion rate of Al and Al-Mn alloys obtained from potentiodynamic polarization tests after 1 hour immersion in 0.6 M NaCl solution.
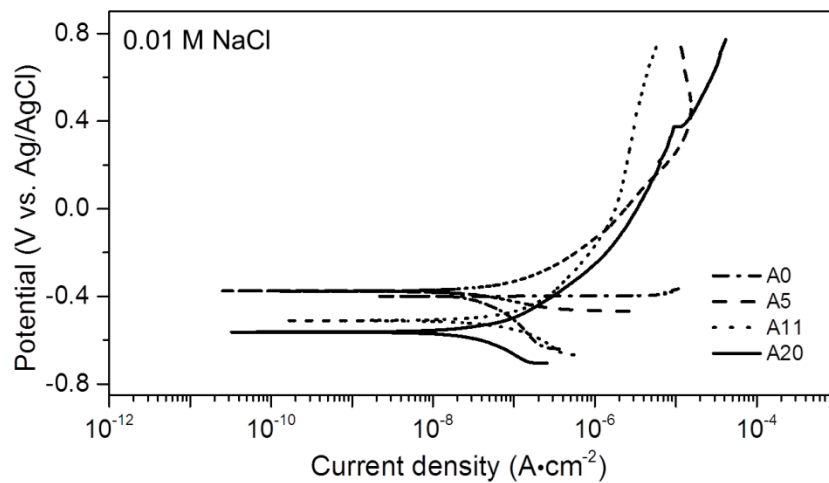
Figure 3.6 Typical potentiodynamic polarization curves of Al and Al-Mn alloys after 1 hour immersion in 0.01 M NaCl solution.
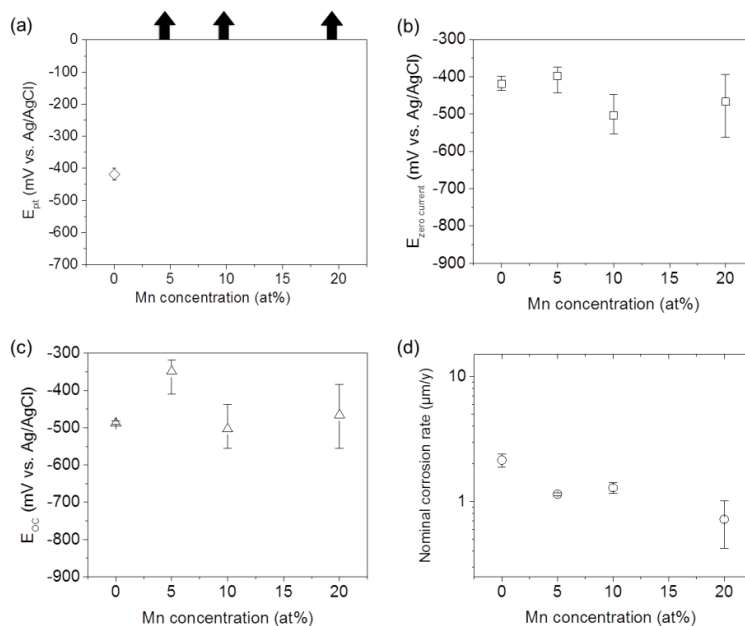
Figure 3.7 Electrochemical parameters (a) Epit, (b) Ezero current, (c) Eoc, and (d) nominal corrosion rate of Al and Al-Mn alloys obtained from potentiodynamic polarization tests after 1 hour immersion in 0.01 M NaCl solution. Arrows denote tests were current surge otherwise indicative of pitting were not observed during anodic polarization.
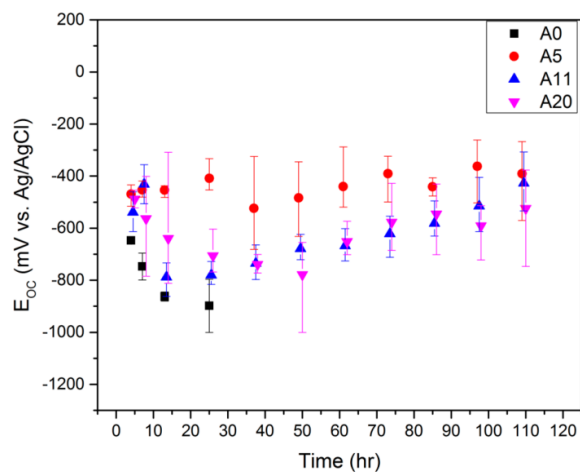
Figure 3.8 Long term evolution of Eoc of Al and Al-Mn alloys immersed in 0.01 M NaCl solution. Al was removed at 24 hrs; all other alloys were exposed up to 108 hrs. The error bars represent the range of data.
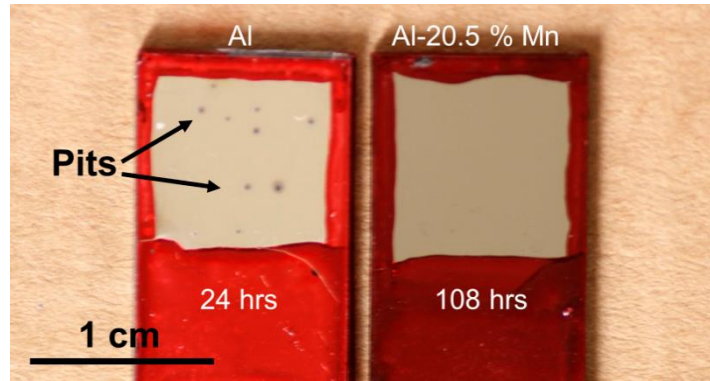
Figure 3.9 Photo of corrosion surfaces of Al (left) and Al-20.5 at.% Mn (right) after immersion in 0.01 M NaCl solution. A diffusive light source was used during photography to minimize surface reflection.
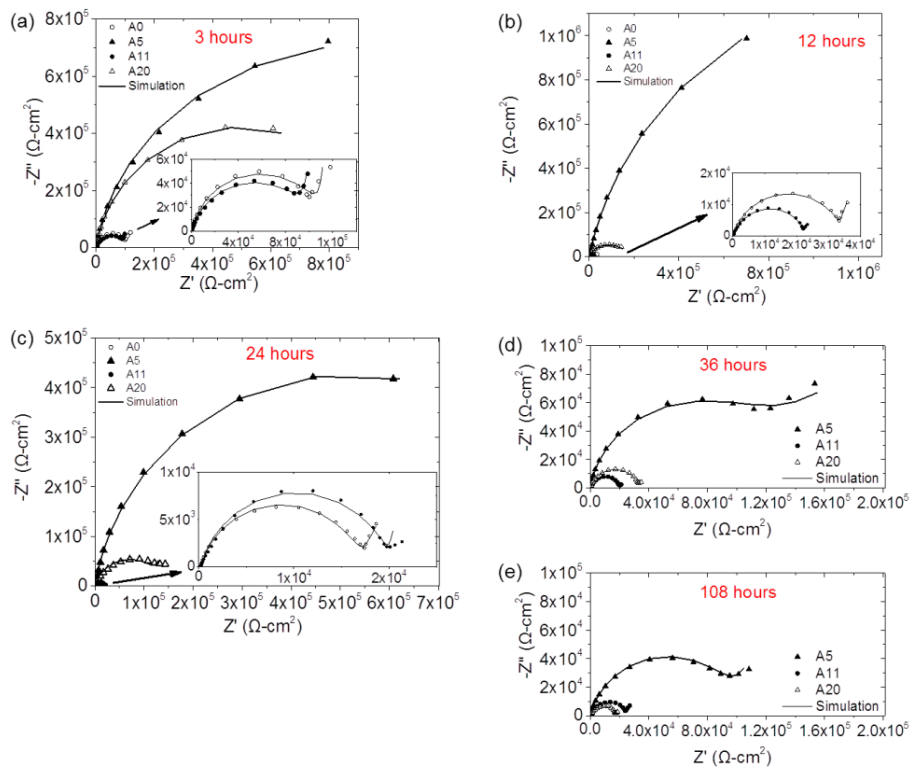
Figure 3.10 Typical Nyquist representation of EIS measurement (scattered data) and model fit (solid lines) of Al and Al-Mn alloys after 3 to 108 hrs immersion in 0.01 M NaCl solution at open circuit potential and 10 mHz minimum data collecting frequency.
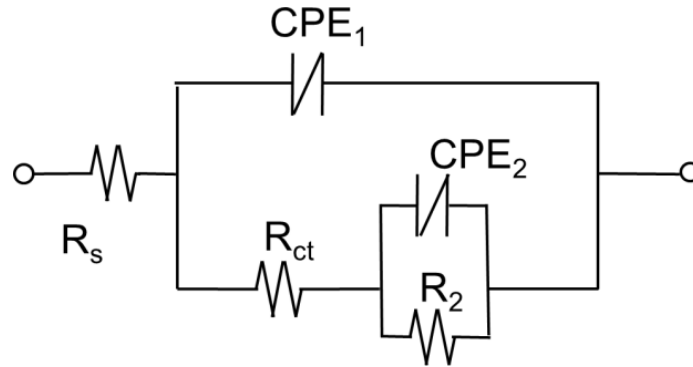
Figure 3.11 Equivalent circuit model used to fit the EIS spectra in Fig.3.10.
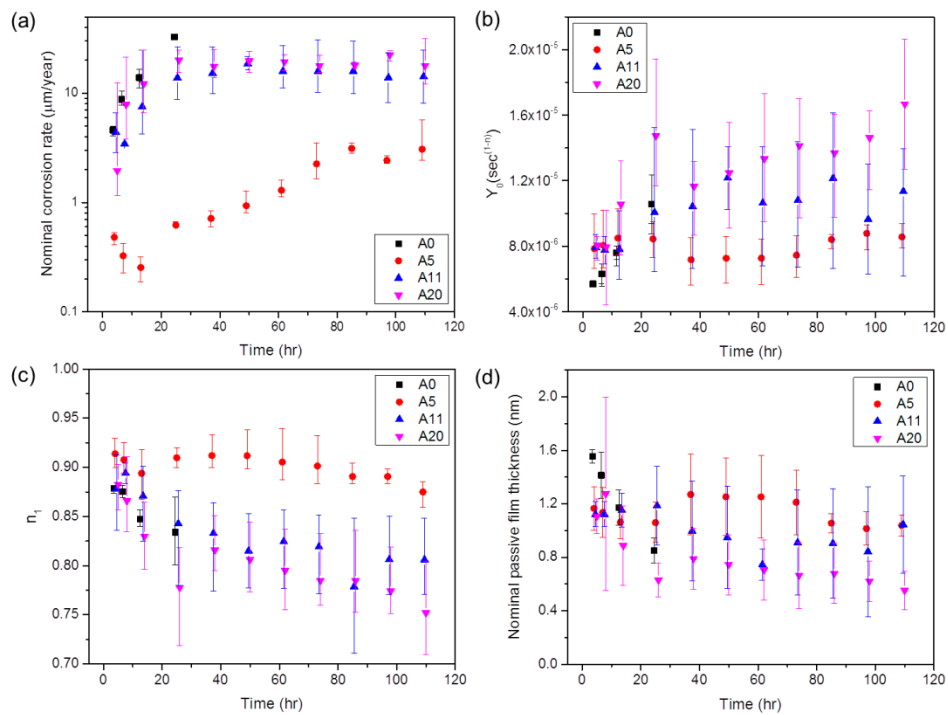
Figure 3.12 The evolution of magnitudes derived from EIS tests (a) nominal corrosion rate, (b) Y0, (c) n1, and (d) nominal passive film thickness as a function of immersion time in 0.01 M NaCl solution. For plot clarity; 0.5, 1, 1.5 and 2 hrs data offset in the time axis was applied to A0, A5, A11 and A20 respectively. The error bars represent the range of data.
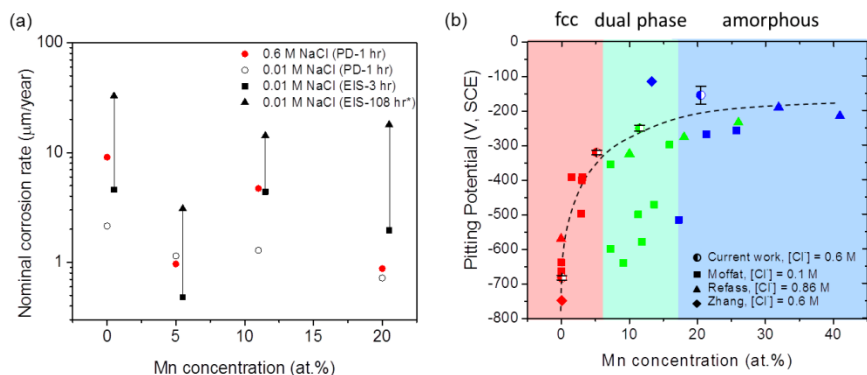
Figure 3.13 (a) Summary of nominal corrosion rate as a function of Mn concentration from PD and EIS tests in 0.01 and 0.6 M NaCl after 1–108 hr immersion. (b) Pitting potential as a function of Mn concentration from the current work and Moffat et al. [21], Refass et al. [26], and Zhang et al. **[119]**. *Solid diamond in (a) represent EIS taken after 108 hr of immersion for all alloys except for pure Al, which is measured at 24 hrs. Red, green, and blue symbols in (b) represent crystalline, dual phase, and amorphous microstructure respectively.
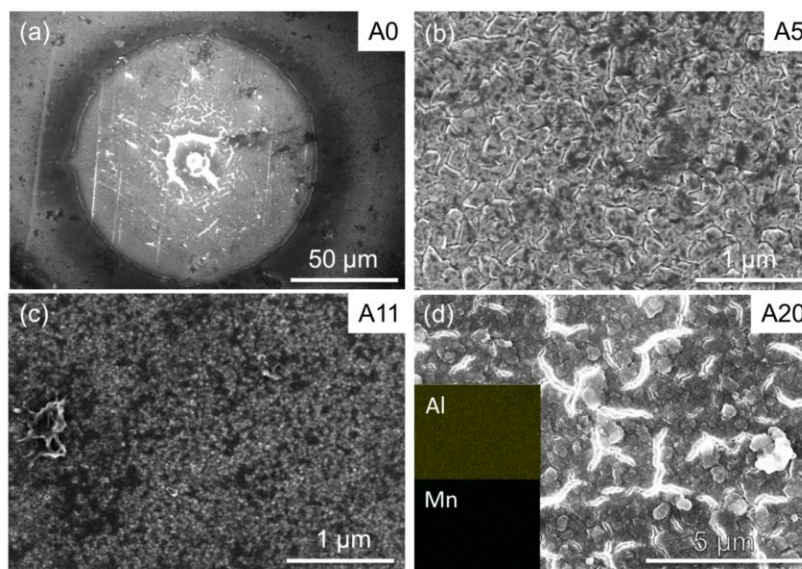
Figure 3.14 SEM micrographs of (a) Al after immersion in 0.01 M NaCl solution for 24 hrs, (b) Al-5.2 at.%Mn, (c) Al-11.5 at% Mn, and (d) Al-20.5at.%Mn after immersion in 0.01 M NaCl solution for 108 hrs. Insets in (d) are the post-corrosion EDS maps of image (d).
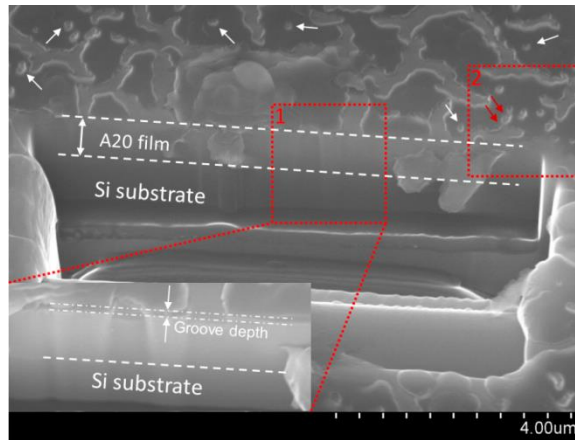
Figure 3.15 Cross-section SEM micrographs of sample A20 after immersion in 0.01 M NaCl solution for 108 hrs. Bottom left inset shows the enlarged area of box 1.

CHAPTER 4: THE EFFECTS OF MN ADDITION ON THE TRIBOCORROSION RESISTANCE OF AL-MN ALLOYS

4.1 Introduction

The increasing demand for materials suitable for complex service conditions such as in biomedical implants, hydraulic systems, nuclear power plants, marine and offshore industries etc. requires the design of new engineering materials resistant to both wear damage and corrosion degradation [96]. Tribocorrosion, a material degradation process caused by the combined effect of wear, corrosion, and their synergy, is most prominent for passive metals such as aluminum (Al) and its alloys [95, 98], which spontaneously form an amorphous semiconducting oxide film (passive film) when in contact with oxygen or water due to their high negative free energy of formation [136]. This passive film, sometimes only a few atomic layers thick, acts as a critical protective barrier against corrosion [95, 136]. When mechanical wear takes place during corrosion, the passive film can be locally destroyed at the contacting asperities, with the ensuing depassivation leading to rapid localized corrosion and early component failure [97, 137]. Thus a better understanding of the tribocorrosion response of Al alloys is required to extend the durability of these technologically important metals in complex service conditions.

Tribocorrosion resistance of passive metals not only depends on material properties (e.g. microstructure, strength, work-hardening ability), but also on environment (e.g. pH, humidity, oxygen concentration) and testing conditions (e.g. applied potential, load, and sliding speed)

[138]. In addition, the problem is further complicated by the fact that the chemical and mechanical attacks are not independent of each other, but often act synergistically to cause accelerated failure [96, 97]. This synergy is often related to various events such as the localized deterioration of the passive film [139], wear debris acting as a third body between the contacting surfaces [140], and material transfer to the counter body due to plastic deformation [141].

This work focuses on studying the alloying effect on the tribocorrosion resistance of Al alloy. Owing to the formation of protective passive film in neutral (pH 4-9) solutions [142], Al is a good candidate for replacing toxic cadmium coatings, and is widely used for corrosion protection of steel [4], magnesium alloys [6], and NdFeB magnets [8] etc. Unfortunately pure Al is highly susceptible to wear due to its low hardness, thus greatly limit the durability and lifetime of such coatings. Alloying is an effective way to improve materials' wear resistance by increasing the hardness per Archard's law (i.e. wear rate is inversely related to hardness) [143]. In addition to hardness increment, proper alloying additions can significantly lower the grain boundary energy and stabilize ultrafine microstructures in the tribolayer, thus suppressing unfavorable stress-assisted grain growth during wear [144]. While most commercial Al alloys are precipitation-hardened to impart good strength and wear resistance, none of them have very good resistance against localized corrosion. The presence of precipitation and secondary particles strengthens the material but, at the same time, enhances corrosion by catalyzing oxygen reduction, increasing the corrosion potential, and localizing the electrochemical activity due to chemical inhomogeneity from the Al matrix [142]. Fig. 4.1 shows the corrosion and wear rate of wrought Al alloys (1xxx, 5xxx, and 6xxx), Al based bulk metallic glass (Al-BMG), and Al based high entropy alloys (Al-HEA) [145-161]. It should be noted here that Al-BMG and Al-HEA are expensive and difficult to fabricate. Recent studies showed that appropriate alloying additions

can increase the pitting potential of Al, provided that the alloying element is retained in solid solution [44, 162-164]. For example, age-hardened 2000 series Al alloys (with Cu as the major alloying element) exhibit poor corrosion resistance [142], but Kim et al. observed an ennoblement of pitting potential with increasing Cu content in Al-Cu solid solutions [162, 163]. Similarly, Al-based high entropy alloys such as $AlxCo_{1.5}CrFeNi_{1.5}Ti_y$, which form a supersaturated solid solution, exhibit remarkable wear and corrosion resistance [165-167].

Current research in tribocorrosion response of Al alloys is very limited in scope. Abundant literature exists pertaining to the possible alloying effects on wear and corrosion resistance, but few attempts have been made to combine knowledge based on these two separated fields towards a better understanding of tribocorrosion. Even though there is no unified theory at the moment, the evidence indicates an exciting opportunity to alloy Al to optimize both wear and corrosion resistance. Fig. 4.2 summarizes alloying effects on hardness, pitting potential and corrosion current density of Al-TM (transition metal) reported so far [9, 34, 44, 105-108, 111, 116, 168]. It can be seen that higher alloying content improves hardness, hence is likely to enhance wear resistance, although the optimum alloy concentration is not known a priori due to complicated dynamic microstructure evolution (e.g. dislocation accumulation due to sustained plastic deformation vs. stress-assisted grain growth and dynamic recovery) in the tribolayer [144]. On the other hand, alloying may affect corrosion resistance of Al in different ways depending on the specific alloying elements, as reviewed by Szklarska-Smialowska [37]. Small quantities of Sn, In, Hg, Ga, and Zn are detrimental to Al corrosion, as they reduce the passive potential region and shift the corrosion and pitting potentials in the negative direction [169]. Thus these TMs lead to high anodic current density and uniform active surface corrosion. Other TMs such as Cu, Mo, Mn, W, Nb, Cr, Ta, V, and Zr improve corrosion resistance and decrease

pitting susceptibility of Al by increasing the overpotential for anodic dissolution and decreasing metastable pit initiation and growth rates [162]. Furthermore, as shown in Fig. 4.2(b-c), the pitting potential of Al-TM generally increases with alloy concentration although the corrosion current remain scattered.

The above discussion suggests a great opportunity of combating tribocorrosion by alloying Al with appropriate TMs in solid solution. This work combines tribological, electrochemical methods and finite element modeling to evaluate the fundamental deformation and degradation mechanism during tribocorrosion of aluminum-manganese (Al-Mn) solid solutions. The corrosion behavior of Al-Mn has been studied extensively previously [34, 109, 118, 170], but the tribocorrosion resistance of this system has not yet been reported before. Al-Mn alloys were prepared by magnetron sputtering. The high effective quench rate during physical vapor deposition allows the generation of high levels of supersaturation of both interstitial and low-miscibility substitutional alloying elements, which is essential in promoting chemically homogenous nanocrystalline or glassy phase formation far beyond the equilibrium solubility limit [116]. The alloying element (Mn) was selected based on the following criteria: 1) excellent microstructure stability due to high grain boundary segregation enthalpy of Mn in Al [171, 172], 2) high ionic potential of Mn_xO_y (e.g. 17.95 for Mn_2O_7 and 15.19 for MnO_3), indicating good oxide film lubricity [173], 3) similar atomic radii as Al (atomic radii ratio rMn/rAl= 1.12) that favors high non-equilibrium solubility, and 4) a wide range of equilibrium phases that could be formed in Al-Mn binary system [174], which allows tunable microstructure via alloying [116, 117]. Alloying elements that satisfy these criteria are expected to have the potential to increase tribocorrosion resistance of Al. This work focused on two compositions: ~ 5.2 at.% and 20.5 at.% Mn, which showed high corrosion resistance for Al-Mn with up to ~ 20

at.% Mn [34]. Their difference in microstructure and hardness also allows the study of the composition-microstructure-tribocorrosion resistance relationship of Al-Mn. While focusing on a binary system here, it is believed that the generated understanding could also benefit the design of more complicated solid solution systems, such as Al based bulk metallic glass and high entropy alloys.

4.2 Materials and Methods

4.2.1 Materials Synthesis, Characterization, and Mechanical Testing

Pure Al and Al-Mn thin films with 5.2 at.% and 20.5 at.% Mn were prepared by RF magnetron sputtering on (100) Si substrate, as listed in Table 4.1. To improve film-substrate adhesion, the native oxide film of Si was chemically etched using hydrofluoric acid prior to deposition. Sputtering was carried out inside a vacuum chamber (CRC-100 sputtering coater) at 80 W input power under 5 mTorr argon atmosphere (99.99%). All metallic film thicknesses were kept at ~ 1.2 μm, as measured using a Dektak D150 Profiler. The as-sputtered films were characterized using grazing incidence X-ray diffraction (GIXRD, PANalytical X'Pert) with monochromatized Cu Kα (1.5404 Å) radiation, at 40 kV and 40 mA. The sample surface morphology and chemical composition before and after tribocorrosion tests were characterized using scanning electron microscopy (SEM, Hitachi SU-70) and energy-dispersive X-ray spectroscopy (EDS, EDAX-Phoenix). Transmission electron microscopy (TEM) analysis including bright-field (BF), dark-field (DF) imaging, and selected area diffraction (SAD) were performed using Tecani F20 TEM. TEM samples were prepared by directly sputtering Al and Al-Mn (~150 nm) on continuous carbon film TEM grids. Post-tribocorrosion cross-sectional samples were prepared from areas inside the wear-track using focused ion beam microscope (FIB, Quanta 200 3D Dual Beam). Nanoindentation tests were performed using a triboindenter

(Hysitron, Ti900) with a diamond Berkovich tip (~125 nm radius). All indentations were carried out under a trapezoidal loading profile with 3 mN maximum load, 0.05 N/s loading/unloading rate, and 5 s holding time. The penetration depth was kept below ~ 10% of total film thickness to eliminate the substrate effect. The hardness was obtained following Oliver–Pharr method [175]. The reported value of hardness is the average of at least 20 measurements.

4.2.2 Electrochemical and Tribocorrosion Tests

A protective stop-off lacquer was applied to the sample surface to expose an effective area of ~1 cm² for the electrochemical tests and ~ 1.8 cm² for the tribocorrosion tests. The electrochemical measurements were conducted in a typical three electrode configuration at ambient temperature in naturally aerated stagnant 0.6 M NaCl aqueous solution (pH ≈ 6.4) using a Gamry Reference 600® potentiostat. The as-deposited samples, mixed metal oxide coated titanium mesh, and a commercial silver-silver chloride electrode (1 M KCl internal solution) served as the working, counter, and reference electrode respectively. Potentiodynamic polarization (PD) measurements were conducted after 1 hr of immersion in the electrolyte allowing for the stability of the open circuit potential (E_{OC}). The scan rate was 0.167 mV/s, starting at a potential ~150 mV cathodic to E_{OC} and terminated when a rapid increase in the anodic current density took place reaching 10 $\mu A \cdot cm^{-2}$. To examine the behavior of the passive film, electrochemical impedance spectroscopy (EIS) and Mott-Schottky (MS) analysis were conducted following potentiostatic (PS) anodic polarization. EIS tests were conducted at E_{OC} in the frequency range of 100 kHz to 10 mHz, 5 points per decade, and 10 mV_{rms} sinusoidal potential excitation. The obtained data was then fitted using Gamry E-chem software. The PS analysis was conducted for 60 min with a sample period of 10 Hz at a fixed potential of 200 mV vs. E_{OC} within the passive region to produce a compact and dense passive film. MS tests were

65

conducted from 0 to 300 mV vs. E_{OC} in the anodic region at 1 kHz frequency, amplitude of 10 mV$_{rms}$, and potential sweeping rate of 10 mV/s.

Tribocorrosion tests were carried out in a reciprocating ball-on-plate mode with alumina ball (Al_2O_3, ø4 mm) as the counter piece using a universal mechanical testing (UMT) apparatus with a custom-made tribocorrosion cell, as shown in Fig. 4.3. Each test was carried out at 5 mm stroke length, 5 mm/s sliding velocity, under 0.5 N normal load (corresponds to initial mean Hertzian contact pressure of 0.47 GPa) at various potentials (E_{OC}, anodic and cathodic potentials) following the hereafter sequence; E_{OC} stabilization for 20 min, application of a specified potential for 20 min, application of reciprocating load for 5 min, re-passivation at the same potential for 5 min. The anodic potential (200 mV above Eoc) was selected within the passive region below the pitting potentials and the cathodic potential (350 mV below Eoc) was chosen to avoid hydrogen evolution reaction during sliding, which might lead to embrittlement of the samples [176]. Pure Al was not tested in the anodic regime due to its active anodic dissolution. A new alumina ball was used for each test to minimize contamination. After the tribocorrosion tests, wear track dimensions were measured using a Dektak D150 profilometer from three different locations along the wear track for each sample. The wear track cross-sectional area (i.e. wear track width times sample height loss) was then calculated using the trapezoidal numerical integration method. The total material loss rate (total volume loss/sliding distance) was obtained by multiplying the cross-sectional area by the wear track length and then divided by the total sliding distance. All electrochemical and tribocorrosion test results reported hereafter correspond to the average from at least three separate samples at each test condition.

4.3 Results and Discussion

4.3.1 Microstructure and Mechanical Properties

Table 4.1 summarizes the composition, microstructure and mechanical properties of all as-deposited samples. The average oxygen concentration measured for all alloys was 0.62 ± 0.17 at.% and was assumed to be negligible here. Fig. 4.4 shows the GIXRD line scans of all samples. Sample A5 exhibited a single fcc phase, similar to that of pure Al, indicating the formation of supersaturated solid solution of Al-Mn, well exceeding the equilibrium solubility limit of Mn in Al (typically < 1 at. % at low temperatures) [177]. The observed peak shift towards higher 2θ angles for A5 compared to pure Al, indicated the reduction of lattice constant from 4.047 and 4.036 Å, suggesting that Mn, which has a Goldschmidt radius ~ 11% smaller than Al, is substitutionally incorporated into the Al lattice. Similar behavior has also been reported by Ruan and Schuh for electrodeposited Al-Mn up to 15.8 at.% Mn [116]. The line scans of A20 showed no evidence of crystalline diffraction patterns, where the broad hump located at $2\theta \approx 42°$ confirmed that this alloy was amorphous.

SEM images in Fig. 4.5 show the surface morphologies of the as-deposited films. It can be seen that pure Al and A5 exhibited faceted angular structure associated with the formation of crystalline phase, where each angular structure often corresponds to an individual grain [46]. Further increasing Mn concentration to 20.5 at.%, the surface morphology of amorphous alloy A20 exhibited compound round nodules, similar to that reported in thin films with ultrafine grains and/or high amounts of amorphous phase [123]. Insets in Fig. 4.5(d and g) are the EDS maps of Mn element of A5 and A20 respectively. It was found that Mn is homogeneously distributed throughout the entire sample tested. Fig. 4.5(b, e, and h) show BF TEM images of Al and Al-Mn alloys. The average grain size of pure Al and A5 was 42 ± 11.5 and 15 ± 6.2 nm

67

respectively, measured using the line-intercept method, while A20 showed no evidence of short range order. The SAD patterns of pure Al and A5 in Fig. 4.5 exhibited single fcc phase, indicated by the discrete diffraction rings, whereas A20 exhibited halo ring confirming the amorphous nature of this alloy.

The hardness of pure Al (0.67± 0.18 GPa) was increased to 1.58 ± 0.13 GPa and 5.41± 0.15 GPa for A5 and A20, respectively. This behavior is similar to that reported in PVD sputtered [170] and electrodeposited [116, 123] Al-Mn alloys. The increase in hardness could be related to solid solution strengthening, structure refinement, and the increase of average bond strength with increasing Mn concentration, as shown recently by Wang et al. via first-principles calculations [178]. The H/E ratio, which is often related to materials' wear resistance [179], is 0.020 and 0.056 for A5 and A20 respectively, as compared to 0.009 for pure Al. This increase in H/E indicates an enhanced wear resistance and coating durability via Mn alloying, as confirmed later in section 4.3.3.

4.3.2 Corrosion Behavior

Prior to tribocorrosion study, effects of Mn on the corrosion behavior of Al were evaluated using PD tests. The typical PD curves of all samples after 1 hr immersion in 0.6 M NaCl solution are shown in Fig. 4.6. Pure Al showed immediate active dissolution upon entering the anodic current regime, while both A5 and A20 showed well-defined passive regions, followed by a rapid increase in current density at the onset of pitting potentials (E_{pit}), i.e. the potential at which stable pits are initiated [109]. The amorphous alloy A20 exhibited the highest E_{pit} due to the high Mn content, similar to that reported elsewhere [118, 170]. At E_{oc}, A5 and A20 exhibited a reduction in corrosion current density (i_{corr}) and an anodic shift of the crossover potentials for zero current ($E_{zero\ current}$) compared to pure Al, indicating the passive behavior of

Al-Mn alloys. The evolution of E_{oc} and the electrochemical parameters obtained from PD measurements are listed in Table 4.2, where the nominal corrosion rates in µm/year was obtained by converting the i_{corr} using Faraday's conversion (1 µA.cm^{-2} ≈ 10.9 µm/y) assuming uniform corrosion with the formation of Al^{3+}. From the above results it can be seen that Mn addition enhanced corrosion resistance and decreased pitting susceptibility of Al, similar to that reported in other Al-TM (TM = Ta, Mo, Cu, W, etc.) systems. It is believed such improvement is due to the fact that Mn alters the pit growth kinetics; since Mn^{2+} has a lower hydrolysis constant than Al^{3+}, thus a higher dissolution rate is required for Al-Mn to maintain the pH necessary for pit growth than pure Al [109].

Alloying additions often affect corrosion resistance by modifying the passive film properties. To evaluate the effect of Mn concentration on passive film protectiveness of Al, potentiostatic (PS) anodic polarization tests were carried out. Fig. 4.7 shows the evolution of current density as a function of time for A5 and A20 at 200 mV above E_{OC}. In PS experiments, the current density (i) could be represented as [180]:

$$i = At^{-k},$$ (4.1)

where t is the time, k is the slope of the curve in the double logarithmic i-t plot, and A is a constant that depends on the applied potential and concentration of the electrolyte. The value of k is considered as an indication of the compactness of the passive film, where k = 0 indicates active corrosion, k = -0.5 indicates formation of porous and diffusion controlled passive film, and k = -1 indicates the formation of protective and compact passive film. From Fig. 4.7 it can be seen that both alloys showed a decrease in the current density as time proceeded, suggesting the continuous growth of the passive film throughout the entire time of anodic polarization. In addition, A20 exhibited more negative slopes (-0.79 and -0.96) compared to A5 (-0.39 and -0.49), indicating the formation of denser and more protective passive film at higher Mn%.

To evaluate the corrosion resistance of the polarized Al-Mn, EIS measurements were conducted after the PS test. The Nyquist representation of the results (Fig. 4.8) shows a single capacitive semicircle, confirming the presence of protective passive film for both alloys. in addition, the diameter of the capacitive semicircles increases with Mn addition, indicating an increase in the corrosion resistance at higher Mn%. The experimental results were fitted using an equivalent circuit model, as shown in Fig. 4.8 inset, where R_S represents the ohmic solution resistance, CPE_1 (constant phase element) represents the somewhat nearly-ideal capacitive behavior of the passive film [8]. That component, in combination with the charge transfer resistance R_1 which represents the impedance associated with the Faradaic reactions on the interface [105], accounts for the time constant of the high frequency semicircle. R_1 may be considered as being representative of a conductive path through imperfections of the passive film that may reflect breakdown ranging from incipient (largest values of R_1) through more advanced (smaller values) paths. R_1 is in series with the components of the time constant at low frequency CPE_2 and R_2 which correspond to the double layer capacitor at the metal surface. The summation of R_1 and R_2 could be considered as the overall impedance and represent the polarization resistance (R_P) of the system [181].

The impedance of the CPE is represented by the following equation [182]:

$$Z_{CPE} = Y_o^{-1}(j\omega)^{-n}, \tag{4.2}$$

where Y_o is a constant that represents the interfacial properties, j is an imaginary unit, ω is angular frequency, and n is a real number between (0 and 1) that represents the heterogeneity of the surface. The modeled curves using this proposed equivalent analog circuit are plotted as solid lines in Fig. 4.8.

The nominal thickness of the passive film is estimated as;

$$d = \varepsilon\varepsilon_o A/C, \qquad (4.3)$$

where ε is the dielectric constant of the passive film (10 for aluminum oxide [129]), εo is the permittivity of vacuum (8.85x10-14 F·cm^{-1}), A is the exposed surface area (~1 cm^2) and C is the capacitance evaluated from CPE$_1$. The equivalent circuit fitting parameters are shown in Fig. 4.9. It can be seen that for all fitting parameters (R$_1$, Y$_0$, and n), A20 is higher than A5, indicating the formation of a more homogenous passive film with higher polarization resistance. In addition, the passive film thickness of A20 is ~ 1.2 nm, much higher than that of A5 (~ 0.6 nm).

Passive films on most metals and alloys are semiconducting, albeit often highly defective. The formation and breakdown of passive film strongly depends on the semiconducting nature of the passive film, which can be evaluated using Mott-Schottky (MS) analysis. During MS test, the electronic properties of the passive film could be evaluated using equations 4.4 and 4.5 for n-type and p-type semiconductor behavior, respectively [119, 183-186].

$$\frac{1}{C^2} = \frac{2}{\varepsilon\varepsilon_0 eN_d}(E - E_{fb} - \frac{KT}{e}) \qquad (4.4)$$

$$\frac{1}{C^2} = \frac{-2}{\varepsilon\varepsilon_0 eN_a}(E - E_{fb} - \frac{KT}{e}) \qquad (4.5)$$

where C is the capacitance, ε is the dielectric constant of the passive film (10 for Al$_2$O$_3$ [129]), ε_o is the permittivity of vacuum (8.85x10^{-14} Fcm^{-1}), Nd and Na are the donor and acceptor densities respectively, E is the applied potential, E$_{fb}$ is the flat band potential, K is Boltzmann constant (1.38x10^{-23} JK^{-1}), T is the absolute temperature, and e is the elementary charge (1.602x10^{-19} C).

The MS curves for A5 and A20 in 0.6 M NaCl solution are shown in Fig. 4.10. The positive slope indicates an n-type semiconductor behavior for both alloys [187]. The donor densities (slope of the fitting straight line) and flat band potential (intersection of the straight line with the potential axis) are shown in Fig. 4.10. For an n-type semiconductor, the donors are

usually positive point defects such as oxygen vacancies or cation interstitials [184]. By increasing Mn concentration, the donor density is decreased from 2.66×10^{17} cm^{-3} for A5 to 5.63×10^{13} cm^{-3} for A20. Moreover, the E_{fb} was shifted towards more negative values, -320 mV and -650 mV for A5 and A20 respectively. The more positive E_{fb} of A5 results from the adsorption of oxygen into the passive film as a result of the oxygen reduction cathodic reaction [188]. The decreased carrier densities of amorphous compared to crystalline alloy was similar to that reported elsewhere [119, 189]. The enhanced corrosion resistance of A20 could be explained by the point defect model [190], where the low concentration of cation vacancies retards the breakdown of the passive film when the Cl$^-$ are incorporated in the anion cites [37]. Taken all the results together, in chloride containing solutions, higher Mn concentration favors the formation of a thicker, more compact and protective passive film on the surface that significantly enhances the pitting resistance and lowers the corrosion rate of Al-Mn.

4.3.3 Tribocorrosion Behavior

Fig. 4.11 shows typical evolution of E_{OC} during tribocorrosion tests for all samples subjected to 0.5 N load in 0.6 M NaCl aqueous solution. It can be seen that once the normal load was applied, a shift of E_{OC} towards more negative values was observed in all samples. This negative shift of potential could be related to the deterioration of the passive film and the exposure of newly depassivated areas having lower equilibrium potential compared to the rest passive areas [176, 191-193]. Once the load was removed, E_{OC} shifted back to more positive values towards its original state, indicating the recovery (repassivation) of the passive film. The amorphous alloy A20 exhibited the lowest negative shift (-20 mV vs. E_{OC}) and the highest recovery rate of E_{OC} compared to A5 (-250 mV E_{OC}) and pure Al (-400 mV E_{OC}). During sliding, there is a competition between passive film removal and repassivation until a at steady-state

tribolayer forms in the worn area. The negligible negative shift of E_{OC} for A20 thus suggests that the depassivation and repassivation rates were in equilibrium for the amorphous alloy [194].

To gain better understanding of the depassivation-repassivation kinetics, a galvanic model proposed by Vieira et.al [191] was used to simulate the potential evolution during sliding. The cathodic potential (E_C) can be calculated as

$$E_c = E_{corr} + a_c - b_c \log i_a - b_c \log[\left(\frac{1}{A_{owt}}\right)\left(\frac{L^2 R C_w t}{0.0833}\right)^{0.333}], \tag{4.6}$$

where E_{corr} is the corrosion potential estimated from PD tests, a_c and b_c are the Tafel constants obtained from the linear regression of the cathodic part of PD curves, i_a is the current density required to repassivate the worn areas, A_{owt} is the area outside the wear track (estimated as the sample surface area exposed to the corrosive environment), L is the wear track length, R is the radius of the alumina ball, C_w is a constant obtained by dividing the wear track volume by the sliding duration, and t is the sliding time. The model simulation results for pure Al and A5 are shown in Fig. 4.12. The E_C evolution of A20 did not fit this model due to its unique behavior as discussed earlier. The fitted ia for A5 (0.9 ± 0.36 µA/cm2) is more than 10 times lower than that of pure Al (13 ± 4.6 µA/cm2), indicating that less current density is required to repassivate the worn surface of A5. Given the similar depassivation rate imposed by mechanical wear, these results indicate a much faster repassivation rate of A5. This is not surprising given the fact that pure Al is in active corrosion mode at OCP as shown earlier by the PD tests (Fig. 4.6).

The applied potential has often been found to significantly affect tribocorrosion resistance by accelerating the total material loss at anodic potentials [195, 196]. In this study, the tribocorrosion behavior was evaluated at three potentials: E_{OC}, anodic (200 mV above E_{OC}) and cathodic (350 mV below E_{OC}) potential. The results are summarized in Fig. 4.13. The total material loss rate (i.e. volume loss normalized by sliding distance) was found to be lowest at the

cathodic potential where the material removal was only caused by mechanical wear, and highest at the anodic potential due to the contribution of both corrosion and wear. This behavior is similar to that reported for heat treated Al alloy [191], 316L stainless steel [196] and tungsten [197] during tribocorrosion. Overall A20 exhibited the lowest material loss compared to A5 and pure Al at all applied potentials, which could be related to its high hardness and enhanced electrochemical properties, as discussed in sections 3.1 and 3.2. Fig. 13(b) shows the evolution of coefficient of friction (COF) at various potentials. For pure Al and A5, COF was found to be almost insensitive to the applied potential while for A20, the anodic shift of applied potential led to a decrease of COF.

SEM images in Fig. 14 show the surface morphology of wear tracks after tribocorrosion tests at various applied potentials. Cross-sectional SEM images (Fig. 14 insets) confirm that all wear track depths were less than the total film thickness and no film delamination was observed. At all potentials studied here, the wear track is characterized by scratches and grooves, indicating extensive abrasive wear. At a given potential, the wear track width decreases with increasing Mn content, indicating improved wear resistance at higher Mn%. At the anodic potential, no pit was observed for either A5 or A20. This is likely due to the high depassivation rate at the testing speed (5 mm/s) that leads to active corrosion of the whole wear track. EDS maps of the wear tracks after tribocorrosion at the anodic potential are shown in Fig. 15. High oxygen content can be seen on the whole wear track of A5, most likely from trapped wear debris with high oxygen content. The fact that the oxygen distribution is patchy on A20 is consistent with its narrow and 'clean' wear track morphology, indicating milder wear compared to A5.

Passive metals often suffer from high wear-corrosion synergy, as discussed in the introduction. The wear-corrosion synergy (S) can be estimated as [176, 198]

$$S = T - W_0 - C_0 \qquad (4.7)$$

where T is the total material loss measured at E_{OC}, W_0 is the material loss due to pure mechanical wear measured at the cathodic potential, and C_0 is the material loss due to pure corrosion estimated from PD tests [139, 199]. To be consistent with unit, all the terms in eqn. (7) was represented in mm/year. The synergy factor (F) is defined as [200]:

$$F = \frac{T}{(T-S)} \qquad (4.8)$$

A high F value thus indicates high synergy between wear and corrosion. The results are shown in Fig. 16. Interestingly, even though A20 exhibits lower T, W_0, and C_0, its wear-corrosion synergy is higher than A5. In other words, the combined attack of wear and corrosion is more detrimental to A20. In addition, it can be seen that at the testing conditions studied here, the total material loss is dominated by mechanical wear while corrosion is negligible. This is in agreement with the criteria proposed by Stack et.al, which take in consideration the ratio of chemical to mechanical wear (C_0 / W_0) [201-203]. For $C_0 / W_0 \leq 0.1$, wear is the dominating mechanism; for $0.1 < C_0 / W_0 \leq 10$, both wear and corrosion contribute significantly to material degradation; and for $C_0 / W_0 > 10$, corrosion is the dominating mechanism. In this work, C_0 / W_0 is 2.33×10^{-5} and 6.36×10^{-5} for A5 and A20, respectively, well below 0.1.

The origin of wear-corrosion synergy often comes from two terms: corrosion-accelerated wear and wear-accelerated corrosion. For corrosion-accelerated wear, the excess material loss at OCP and anodic potential compared to the cathodic potential indicates that corrosion significantly accelerated wear of Al-Mn, most likely by trapping abrasive wear debris with high Al_2O_3 content. Wear debris particles generated at the presence of passive film are likely to contain higher oxygen content compared to those from wear tests without corrosion. Indeed, EDS analysis at the anodic potential shows a high oxygen concentration on the wear track of

both samples (Fig. 15). Depending on the lubricity, these debris can act either as abrasive particles or solid lubricant. According to Erdemir's crystal chemical model [173], the lubricity of oxide is related to its ionic potential $\varphi = Z/r$, where Z and r is the charge and radius of the cation respectively. Oxides with high ionic potential $\varphi > 7$ (such as V_2O_5, MoO_3) are soft and lubricious, while oxides with low ionic potential $\varphi < 7$ (such as TiO_2, Fe_2O_3) are strong and difficult to shear. The ionic potential of Al_2O_3 is 4.4; thus, it is considered strong and abrasive and will lead to accelerated wear. It should also be noted that while manganese oxides such as Mn_2O_7 and MnO_3 are lubricous, X-ray photoelectron spectroscopy study showed that the passive film of Al-Mn was mainly composed of AlO(OH) and Mn was selectively dissolved in the outer part of the passive film [119]. Thus their effect on surface friction and wear can be neglected here.

In addition to corrosion-accelerated wear, another origin of wear-corrosion synergy is wear-accelerated corrosion, which can be measured by recording the current evolution under imposed passive potential. Typically at the onset of rubbing, the wear track depassivates, leading to an increase in the current flow through the metal/electrolyte interface in order to sustain the imposed passive potential. As long as depassivation prevails during the test (I.e. the depassivation rate is much higher than repassivation rate), the current remains at an elevated level until the end of the test, when the current restores its original value due to subsequent repassivation of the worn area. The wear accelerated corrosion can then be quantified by calculating the total charge transferred due to this excess current flow. The evolution of this current for A5 and A20 at the anodic potential is shown in Fig. 17(a). Before the initiation of sliding, both samples were in their passive states and the current is less than 1 µA. Unlike A5, which exhibit a sharp increase in current at the onset of rubbing, A20 exhibits a low current for

the first ~ 50 sec before reaching steady state. It is likely that the high hardness of A20 results in a smaller wear track during the initial running-in period, which can be repassivated quickly. During sliding, the current increase is higher in A5 than A20, indicating accelerated corrosion due to the deterioration of the passive film is more significant for the former [139, 204, 205]. Once the load was removed, the galvanic current shifted back towards its original state indicating the recovery of the passive film, similar to that reported in other passive alloys [206].

To quantify the wear accelerated corrosion, the contribution of electrochemical material loss (Vchem) resulted from metal oxidation under anodic applied potential could be calculated by Faraday's law as [191, 207, 208]

$$V_{chem} = \frac{QM}{nF\rho} \tag{4.7}$$

where Q is the electrical charge (calculated by multiplying the difference between the average anodic current during and before sliding by the time), M is the molecular weight of Al (26.98 g/mole), n is the oxidation valence (3 for Al), F is Faraday's constant (96,500 C/mole) and ρ is the density ($\approx$ 2.7 g/cm^3). The electrochemical material loss is equal to that required to repassivate the worn area (hence rebuild the oxide film) by metal oxidation[207]. The total material loss at the anodic potential is then represented by the sum of the electrochemical (Vchem) and mechanical material loss (Vmech), as shown in Fig. 17(b). It can be seen that A20 exhibited less contribution of Vchem (8.3X10^{-11} mm^3) compared to A5 (1.9X10^{-10} mm^3), indicating less metal oxidation was required for repassivation at higher Mn%.

4.4 Summary and Conclusion

This work expanded the available research on wear and corrosion to the tribocorrosion behavior of Al-Mn alloys. Al-Mn as processed here formed chemically homogenous supersaturated solid solutions. Increasing Mn concentration led to the formation of

nanocrystalline (5.2 at.% Mn) and fully amorphous (20.5 at.% Mn) microstructures. Mn was found to be highly effective in improving the wear, corrosion, and tribocorrosion resistance of Al. Mn addition increased the hardness of Al by solid solution strengthening and structure refinement. Such hardness increment resulted in improved wear and tribocorrosion resistance. At the same time, Mn addition enhanced the protectiveness of passive film; thicker and denser passive film with lower defect density was formed at higher Mn concentration. The total material loss was found to increase with applied potential. At cathodic potentials, mechanical wear dominates tribocorrosion, and the total material loss is mainly governed by the mechanical properties of the material. At open circuit and anodic potentials, mechanical wear led to local depassivation of the wear track, with the ensuring active corrosion resulting in accelerated material loss. Finally, the Al-Mn system studied here is self-repairing; upon the removal of mechanical load, the depassivated area quickly repassivates, with faster repassivation kinetics at higher Mn content.

Table 4.1 Summary of microstructure and mechanical properties of as-deposited Al and Al-Mn thin films. Lattice constant (a) was calculated from GIXRD results. Grain size (d) was measured from BF and DF TEM images using line-intercept method. Hardness (H) and elastic modulus (E) were calculated from nanoindentation tests.

Sample ID	Mn %(at.%)	a (Å)	d (nm)	H (GPa)	E (GPa)	H/E	Phase
A0	0	4.047	42 ± 11.5	0.67 ± 0.18	70.13 ± 5.16	0.009	nanocrystalline
A5	5.2 ± 0.1	4.036	15 ± 6.2	1.58 ± 0.13	77.65 ± 3.19	0.020	nanocrystalline
A20	20.5 ± 0.4	-	-	5.41 ± 0.15	97.54 ± 0.15	0.056	amorphous

Table 4.2 Electrochemical parameters of Al and Al-Mn alloys obtained from PD tests in 0.6 M NaCl aqueous solution. The values of nominal corrosion rates were reported in μm/year as commonly adopted in the literature for thin films. Values are shown as Average (Range)

Sample ID	β_a	β_c	E_{oc}	E_{pit}	Nominal i_{corr}	Nominal Corrosion Rate (μm/year)
A0	-	0.75 (0.17)	-730 (105)	-640 (12)	8.3 (3.0)	9.1 (3.3)
A5	0.23 (0.17)	0.23 (0.10)	-450 (64)	-276 (16)	0.9 (0.3)	1.0 (0.4)
A20	0.35 (0.05)	0.31 (0.26)	-564 (62)	-110 (54)	0.8 (0.4)	0.9 (0.5)
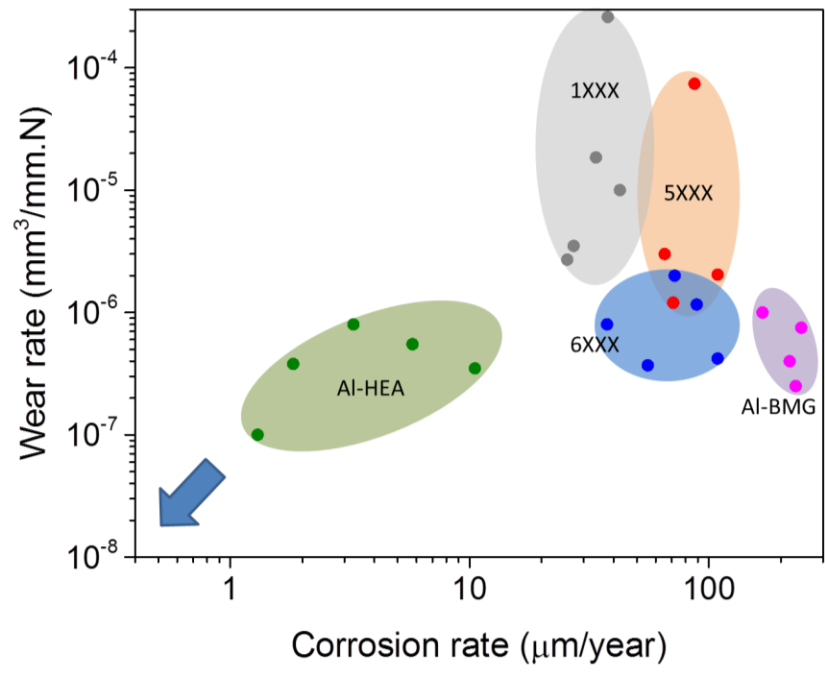
Figure 4.1 Corrosion rate vs. wear rate of wrought, BMG, and HEA Al alloys [145-161].
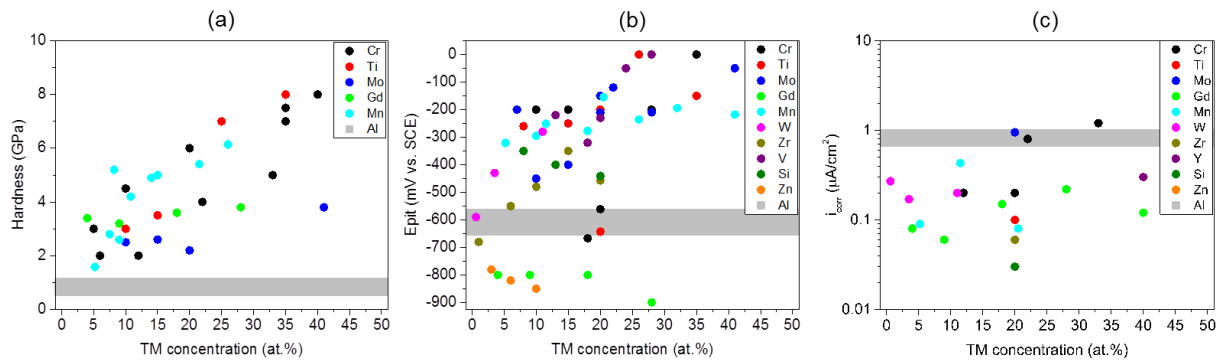
Figure 4.2 Summary of (a) hardness, (b) pitting potential, and (c) corrosion current density as a function of transition metal (TM) concentration in Al-TM systems [145-161] .
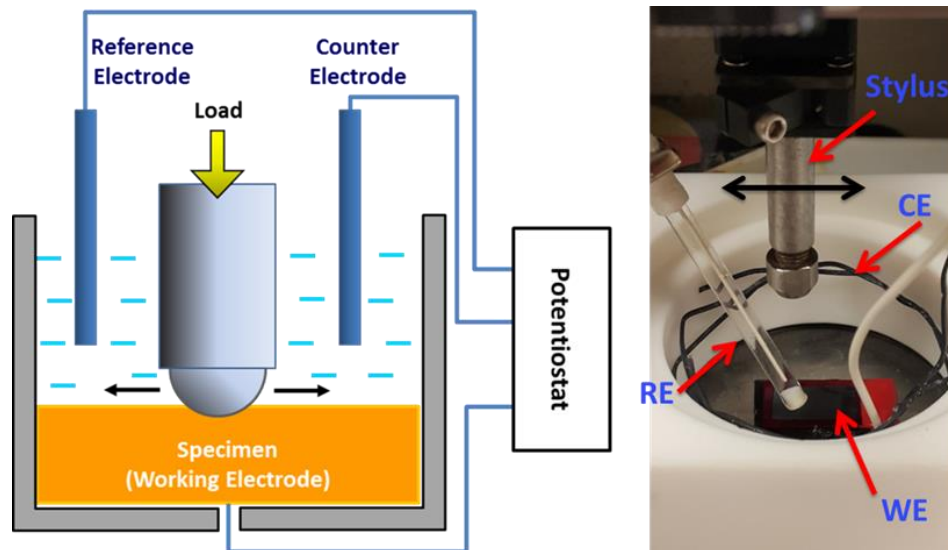
Figure 4.3 Schematic illustration (left) and photo (right) of tribocorrosion set-up used in the current study.
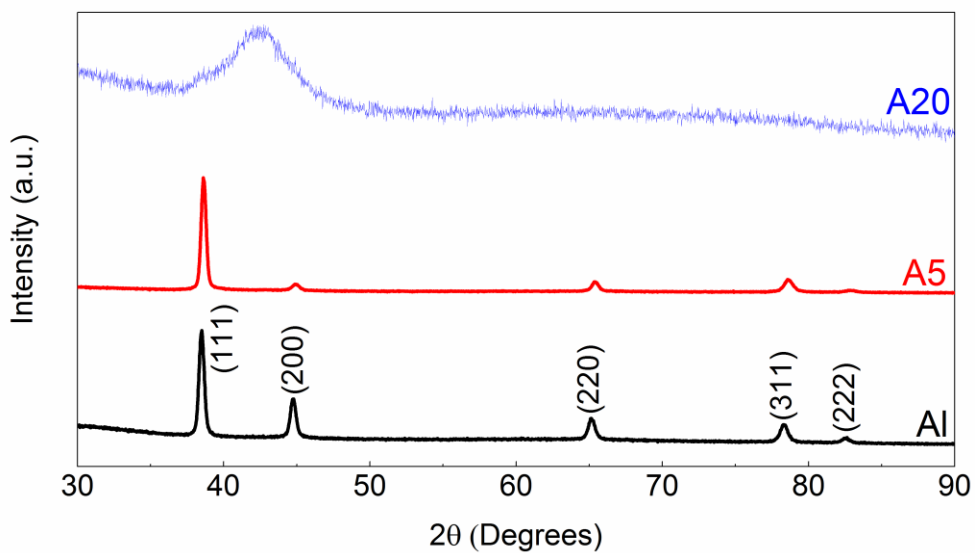
Figure 4.4 GIXRD line scans of as-deposited Al and Al-Mn alloys.
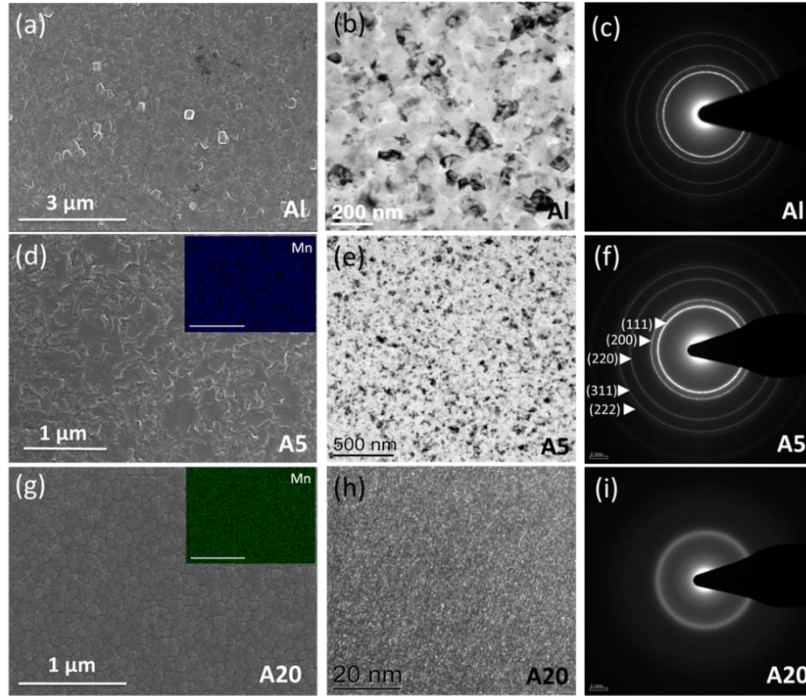
Figure 4.5 (a),(d),(g) Surface SEM images, (b),(e),(h) BF TEM images, and (c),(f),(i) the corresponding SAD patterns of as-deposited samples. Insets in (b) and (c) are the EDS maps (scale bar is 5 μm) of as-deposited A5 and A20, respectively.
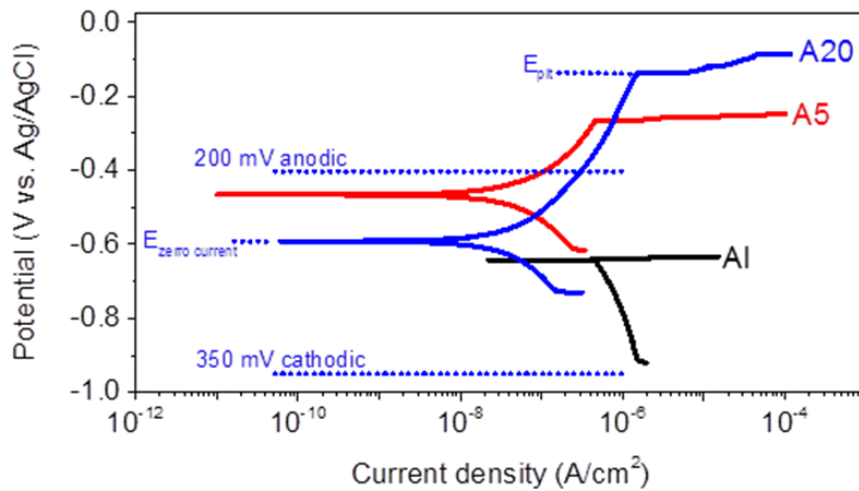
Figure 4.6 Typical potentiodynamic polarization curves of Al and Al-Mn alloys after 1 hour immersion in 0.6 M NaCl solution.
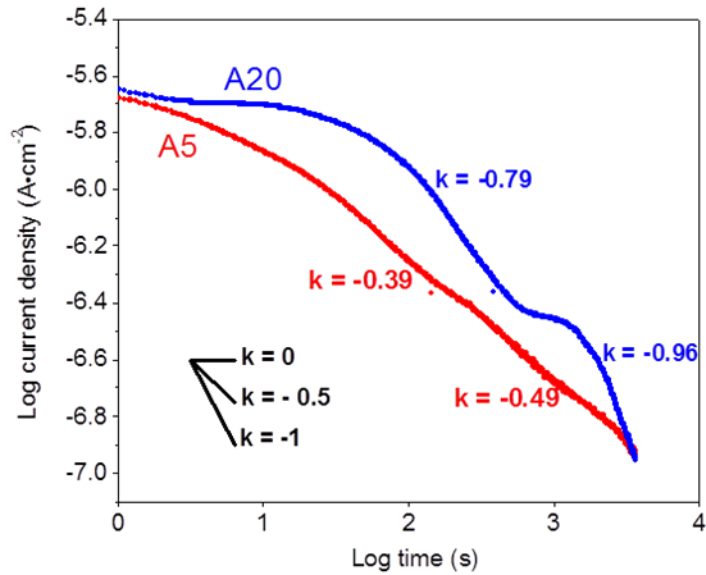
Figure 4.7 Double-log plots of current–time of the amorphous and crystalline Al-Mn alloys during anodic potentiostatic polarization at a constant potential of 200 mV vs. Eoc for 3,600 s in 0.6 M NaCl aqueous solution.
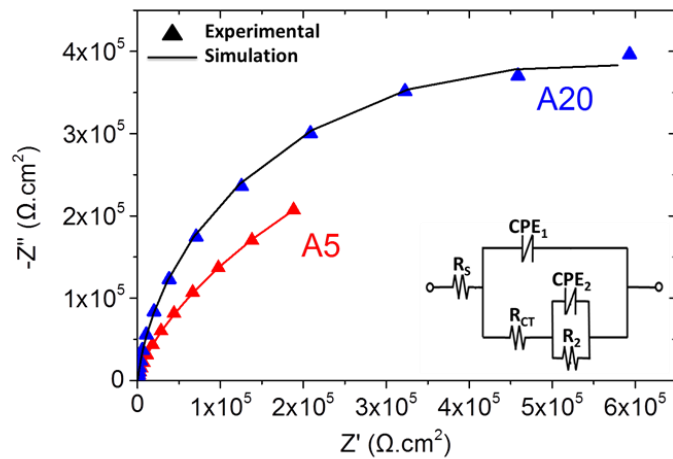
Figure 4.8 Typical Nyquist representation of EIS measurement (scattered data) and model fit (solid lines) of the amorphous and crystalline Al-Mn alloys measured at open circuit potential, 10 mHz minimum frequency at data collecting frequency of 5 points per decade
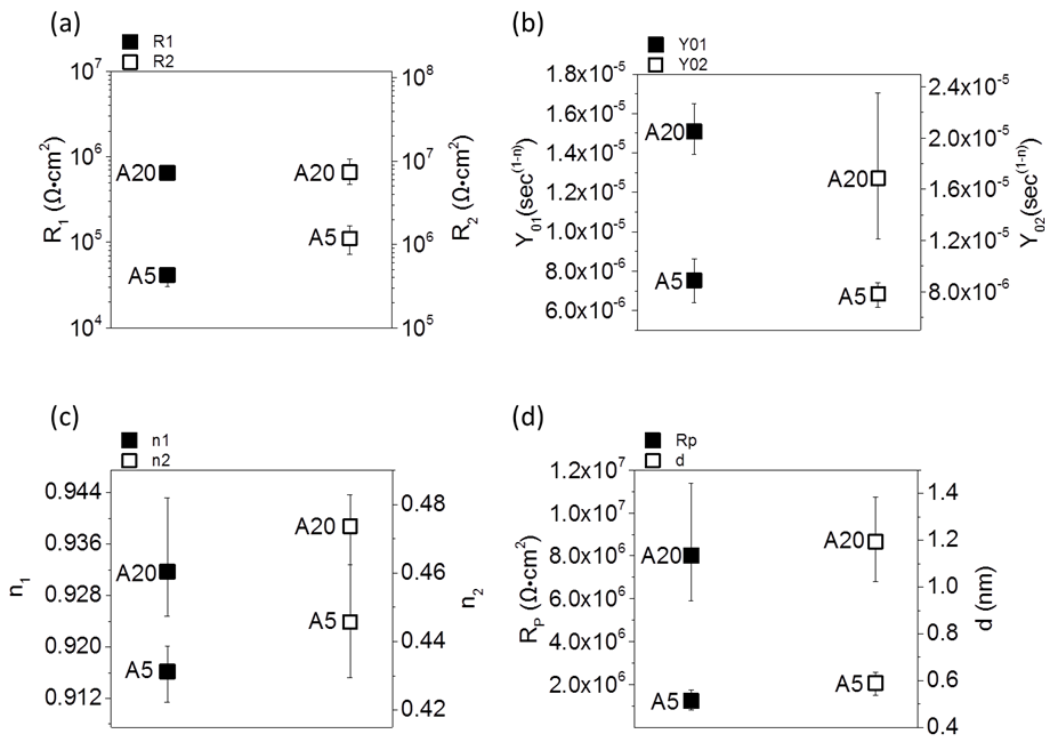
Figure 4.9 Equivalent circuit parameters (a) R, (b) Y0, (c) n, and (d) RP and passive film thickness (d) of the amorphous (A20) and crystalline (A5) Al-Mn alloys in 0.6 M NaCl solution.
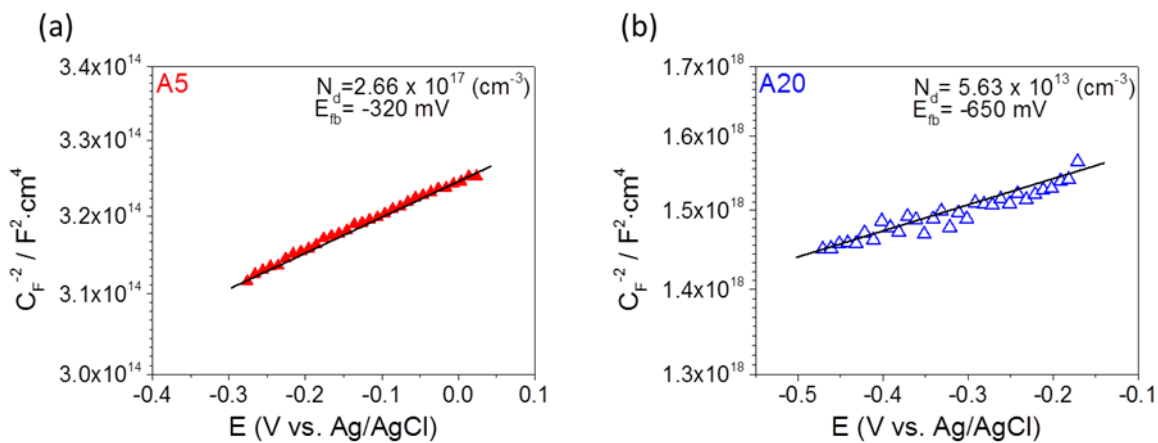
Figure 4.10 Mott–Schottky plots of passive films formed on the amorphous and crystalline Al-Mn alloys after anodic potentiostatic polarization in 0.6 M NaCl aqueous solutions with a measurement frequency of 1 kHz.
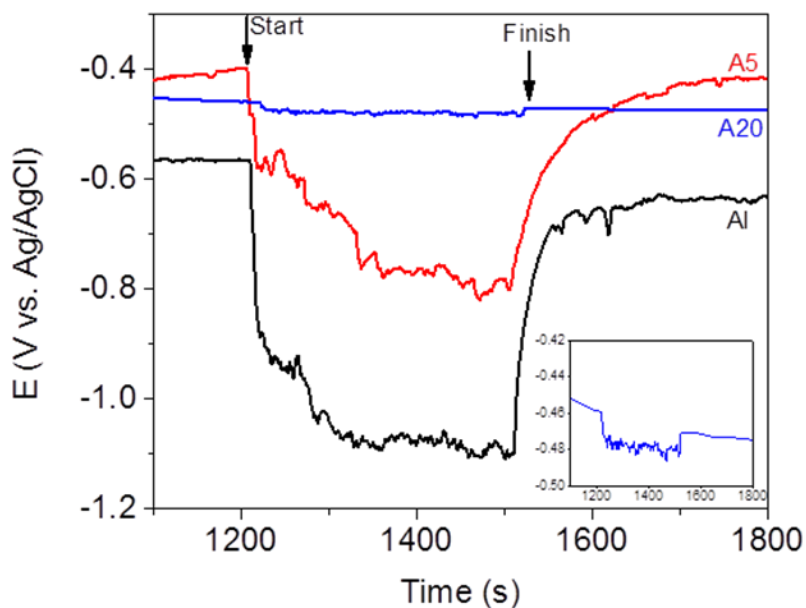
Figure 4.11 Evolution of corrosion potential before, during and after tribocorrosion tests at open circuit potential in 0.6 M NaCl. Inset shows data for A20 plotted on a smaller potential scale for better visualization.
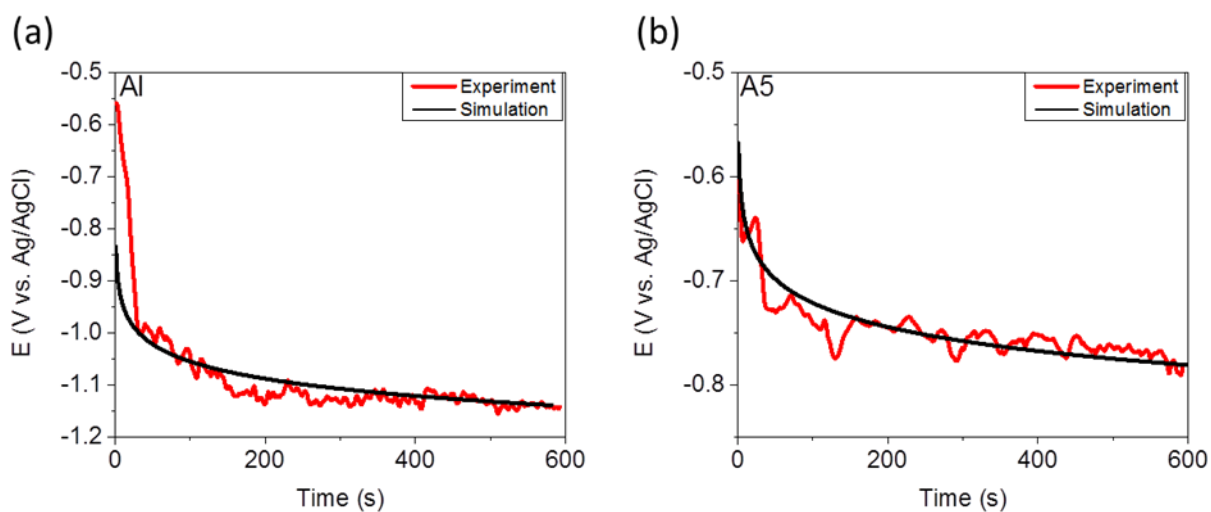
Figure 4.12 Experimental measurements (red curves) and model simulation (black curves) of potential evolution during tribocorrosion tests for (a) Al and (b) A5.
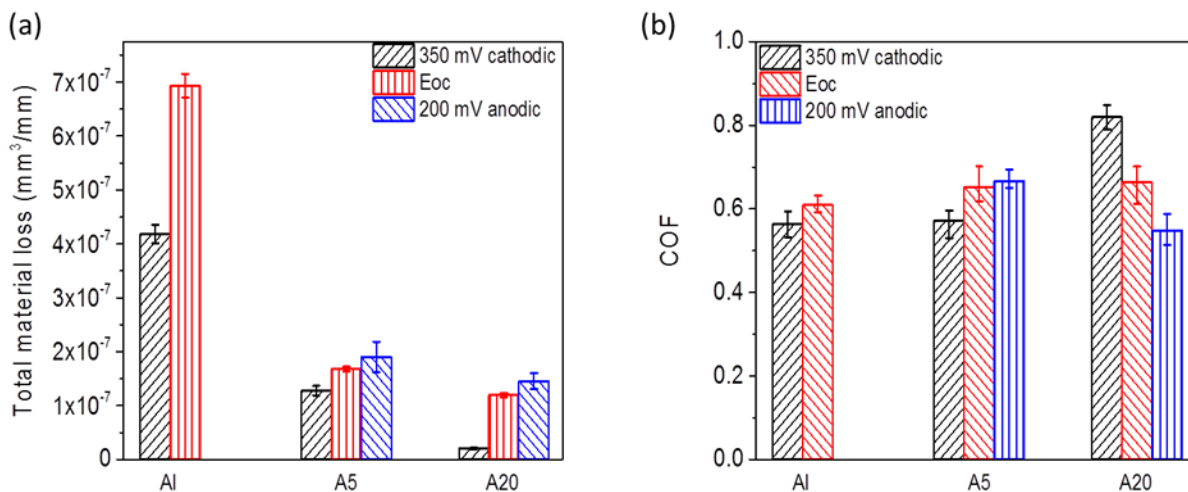
Figure 4.13 Summary of (a) the total material loss, and (b) COF of Al and Al-Mn alloys at various applied potentials.
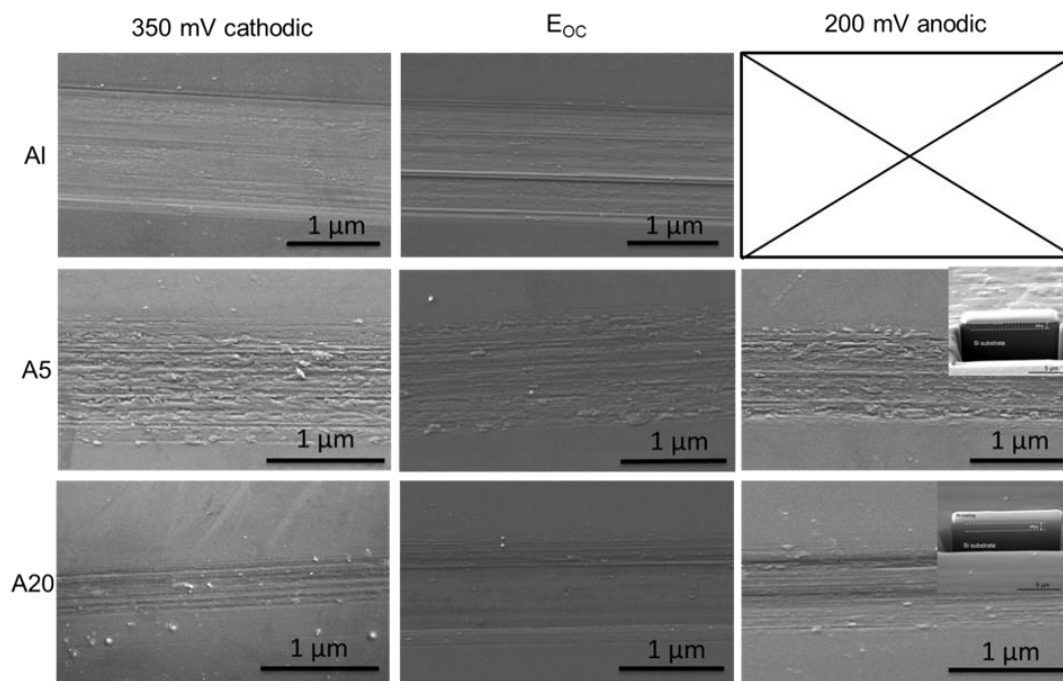
Figure 4.14 SEM images of the wear track formed on Al and Al-Mn alloys in 0.6 M NaCl at different applied potentials.
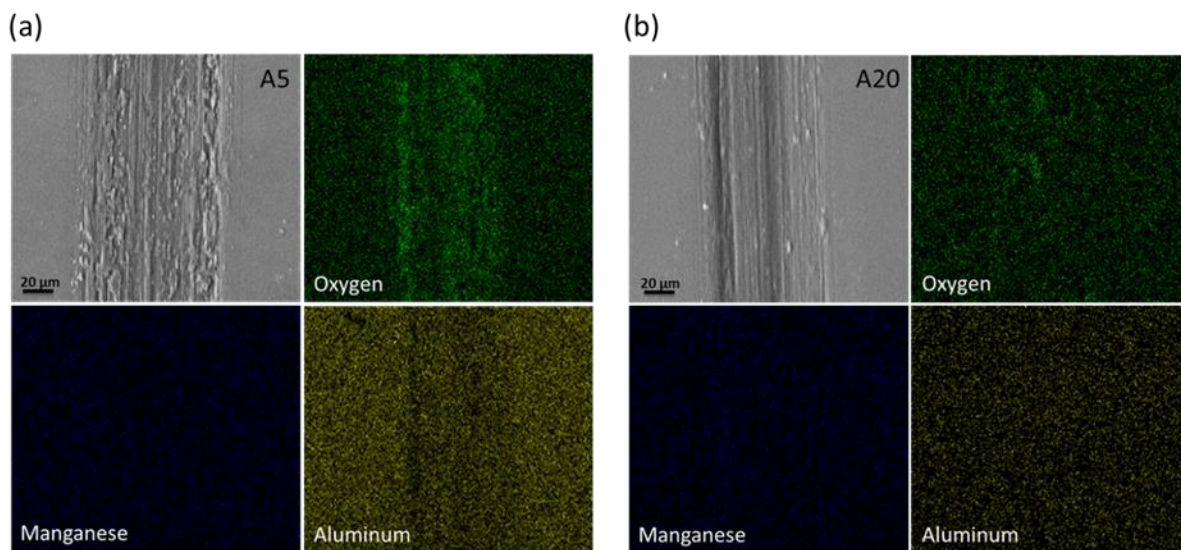
Figure 4.15 SEM image and the corresponding EDS element maps (O, Mn and Al) of (a) A5 and (b) A20 after tribocorrosion at the anodic potential (200 mV above Eoc).
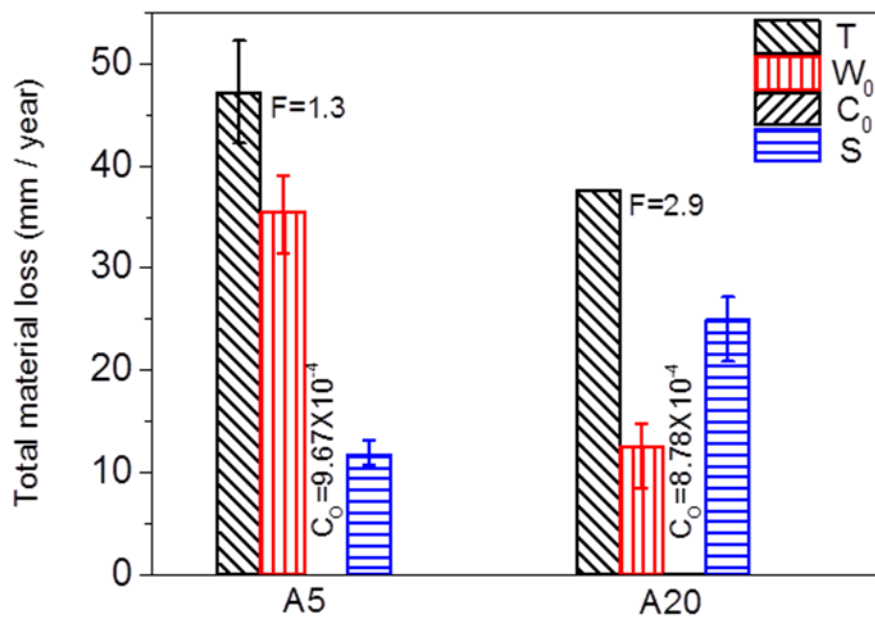
Figure 4.16 Synergetic contributions of the mechanical wear and corrosion of the amorphous and crystalline Al-Mn alloys in 0.6 M NaCl. The total material loss (T) was measured at the open circuit potential.
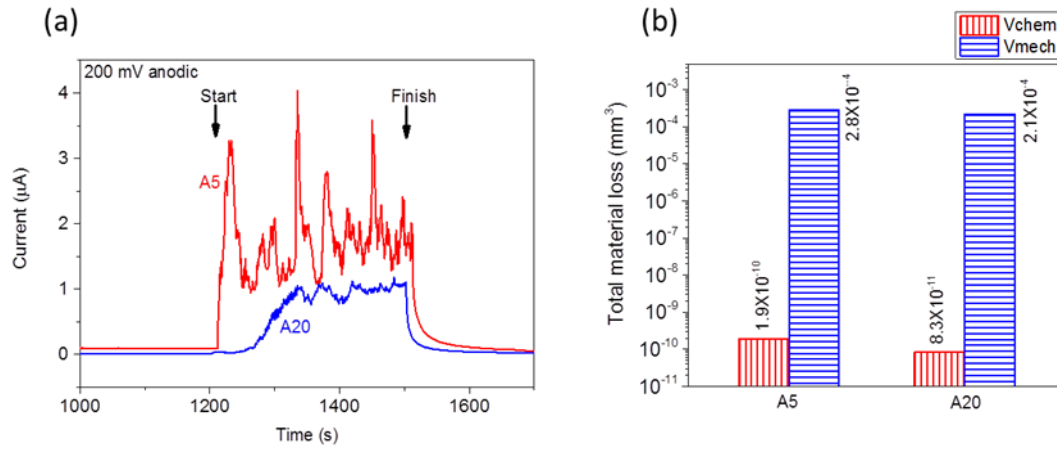
Figure 4.17 Current evolution and (b) chemical and mechanical wear of A5 and A20 during tribocorrosion under anodic applied potential.

CHAPTER 5: INFLUENCE OF CHEMICAL HETEROGENEITY ON THE CORROSION RESISTANCE OF BIODEGRADABLE WE-43 MG ALLOY

5.1 Introduction

Biodegradable WE43 magnesium (Mg) alloy containing major alloying elements of yttrium (Y, 4.1wt%), neodymium (Nd, 2.1wt%), and zirconium (Zr, 0.56wt%) has received great interest lately for potential applications as cardiovascular stents [21, 209] and bone implants [210, 211]. WE43 Mg alloys exhibit good cell adhesion in physiological environment and can safely degrade in the human body; hence no post operation is required once the damaged tissue is healed, minimizing procedure cost and risks [212, 213]. In contrast to conventional medical metals such as titanium, cobalt-chromium, and stainless steel, the mechanical properties of Mg are close to that of human bones [214, 215], thus minimizing the stress shield effect [216] and increasing implant stability [214]. Moreover, Mg is an essential element for human metabolic processes and has been shown to enhance bone growth when used as implants [82, 217, 218].

The high degradation rate of Mg alloys in physiological environments [219, 220] and subsequent loss of structural integrity and extensive hydrogen evolution to balance the anodic dissolution [221, 222], limits the wide applications of these materials. For example, FDA determined that implants have to retain 80% of their initial mechanical properties during the first 12 weeks after implantation, and the total absorption should be achieved in around 2-3 years. When tested in vivo, Witte et al. [223] found that WE43 Mg alloy completely degrade within 18 weeks. Corrosion of Mg occurs as per the following half-cell reactions [53, 54].
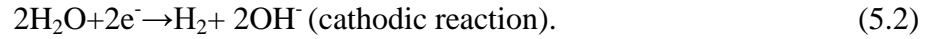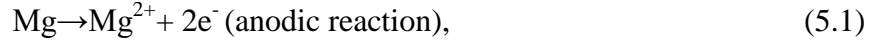
$$Mg \rightarrow Mg^{2+} + 2e^- \text{ (anodic reaction)}, \hspace{2cm} (5.1)$$

$$2H_2O + 2e^- \rightarrow H_2 + 2OH^- \text{ (cathodic reaction)}. \hspace{1.5cm} (5.2)$$

The electrons released from the dissolution of Mg (anodic reaction) are consumed by the cathodic reaction to generate H_2 gas [55]. The Mg^{2+} and OH^- ions formed by the anodic and cathodic reactions, respectively, will then combine to form $Mg(OH)_2$ film as [53];

$$Mg^{2+} + 2OH^- \rightarrow Mg(OH)_2. \hspace{2cm} (5.3)$$

The selection of proper alloying elements with specific composition is a common approach to enhance the mechanical properties and corrosion resistance of Mg [16]. The high solubility of Y in Mg, similar electrochemical potential, same crystal structure, and similar atomic radii promotes the effective strengthening of Mg by the formation of precipitates or secondary particles [16, 75]. The addition of Y with other rare earth elements was also found to enhance the creep resistance of Mg alloy due to the formation of Y rich phases [16]. Nd was found to be biocompatible [76, 77] and effective in enhancing the corrosion resistance of Mg alloys by reducing micro-galvanic effects due to the presence of intermetallic compounds [78-80]. Nd also enhances the mechanical properties of Mg by forming intermetallic phases at the grain boundaries [17, 78, 81]. Zr addition increases the strength of Mg mainly by grain refinement [82]. Due to the limited solubility of Zr in Mg, the undissolved Zr particles act as selective nucleation cites during solidification. The corrosion resistance of Mg was found to be enhanced when the concentration of Zr is kept below 2% [16].

While alloying is a convenient method to enhance the mechanical properties of Mg, its effect on corrosion resistance is often complicated and detrimental. This is because the formation of precipitates and secondary phases due to alloy addition strengthens the material, but at the same time, often lead to undesired micro-galvanic coupling between the precipitates and α-Mg

matrix, which is considered the dominating corrosion mechanism of Mg alloys. Various strategies have been explored to enhance the corrosion resistance of Mg alloys, including designing new alloy compositions and microstructures [224-226], as well as applying various surface treatment methods such as ion implantation [210, 215, 227-230], electrodeposition [231, 232], and physical vapor deposition (PVD) [233, 234] to modify or cover the surface of Mg. The new alloy design approach did not entirely resolve the issue of galvanic coupling between different secondary phases coexisting with α-Mg matrix in the alloy. In addition, new alloys with favorable in vivo degradation behavior are not necessarily associated with good biocompatibility, thus extensive time-consuming animal studies have to be performed (and positive outcome demonstrated) before they could be approved by FDA [235]. On the other hand, the surface modification approach enhances the corrosion resistance of the alloy by altering the chemical and/or physical properties of the surface [236-244]. For example, James et al. [229] plasma implanted WE43 alloy with both Zr and N and found enhanced corrosion resistance due to the formation of Zr and N rich surface layer. However, surface treatment such as plasma ion implantation is only effective in altering the properties of a very thin (50-150 nm) surface layer [210, 215, 229], hence offering very limited benefits for corrosion resistance improvement. In addition, there could be accelerated corrosion due to galvanic effects between coating and Mg substrate.

Given the limitations noted above, the present work aims at evaluating the role of chemical heterogeneity on the microstructure-corrosion resistance relationship of WE43 Mg alloy. The approach presented here consists of keeping composition as in the regular commercial alloy, but modifying processing of the material via a deposition process to obtain a microstructure that is radically different from that of the conventionally prepared, cast material.

Samples from two metallurgical states will be investigated: cast and as-deposited. The cast samples contain extensive precipitates due to limited solubility of alloying elements in Mg, hence representing a microstructure with high level of chemical heterogeneity. The deposited samples, prepared using non-equilibrium processing technique (i.e. physical vapor deposition), contain supersatured solid solution of all elements hence representing a microstructure without chemical heterogeneity. Corrosion study, combined with in-situ image monitoring, and post-corrosion microstructure characterization will be combined to study the roles of chemical heterogeneity on the corrosion mechanism of WE43 in simulated physiological environment.

5.2 Materials and Methods

5.2.1 Materials Synthesis and Characterization

Cast WE43 Mg sheets (1 mm thickness) and sputtering targets with the same global composition of 4.1 wt.% Y, 2.1 wt.% Nd, 0.56 wt.% Zr, and balance Mg, were purchased from AEM Products. The cast sheets were cut into rectangles of (25x15) mm^2 for the electrochemical tests. Prior to corrosion testing, the cast samples were mechanically polished using a series of SiC abrasive papers down to 2400 grit size, followed by 0.3 µm alumina polish suspension (Pace Technologies), rinsed with di-water, and air dried. The thin film samples were prepared by DC magnetron sputtering (CRC-100 sputter coater) on (100) Si wafers. Prior to sputtering, the Si wafers were chemically etched using hydrofluoric acid to remove the native oxide film. Sputtering was conducted inside a vacuum chamber (5 mTorr working pressure) with argon atmosphere at 100 A current for 3hr hours to achieve a nominal film thickness of ~ 570 nm.

The cast and as-deposited thin films were studied by grazing incidence X-ray diffraction (GIXRD, X'Pert PANalytical), using Cu Kα (1.5404 Å) radiation at 40 kV and 40 mA. Data was collected over 2Θ values of 20-80°, 0.015° step size, and 3.5 s per step. The obtained diffraction

patterns were then analyzed using X'Pert Highscore software. The surface morphology and composition of all samples were characterized using scanning electron microscopy (SEM, Hitachi SU-70) and calibrated energy-dispersive X-ray spectroscopy (EDS, EDAX-Phoenix). EDS analysis were carried out using acceleration voltage of 10 kV. Transmission electron microscopy (TEM) analysis of as-sputtered samples, including bright-field (BF), dark-field (DF) imaging, and selected area diffraction (SAD) were performed using (Tecani F20) TEM operated at 200 kV. TEM samples were prepared by directly sputtering the WE43 on continuous carbon film TEM grids for 15 min, which resulted in a sample thickness of ~150 nm. TEM grain size was estimated using line-intercept method. Cross-sections of samples after the electrochemical test were prepared by milling the sample surface using focused ion beam microscope (FIB, Quanta 200 3D Dual Beam) operated at 20 kV using Ga ions.

5.2.2 Electrochemical Tests

An effective area of 1 cm² of all samples was obtained by using Gamry PortHoleTM electrochemical sample mask for the electrochemical tests. All electrochemical measurements were performed at room temperature using a Gamry Reference 600® potentiostat with the conventional three electrode configuration in naturally aerated and stagnant blood bank buffered saline having a pH of 7.0-7.2 and the following ingredients concentration in g/L (NaCl: 8.5, Na_2HPO_4: 1.67, $NaHPO_4$: 0.39). The sample, mixed metal oxide coated titanium mesh, and a commercial silver-silver chloride electrode (1 M KCl internal solution) were used as the working, counter, and reference electrode, respectively.

Potentiodynamic polarization (PD) measurements were conducted in a single upward scan at constant scan rate of 1 mV/s, starting from cathodic potential (~ -150 mV to E_{OC}) to anodic potential (~ +300 mV Vs. E_{OC}). EIS tests were conducted after 15 min of immersion in

the electrolyte at E_{OC} in the frequency range of 10 kHz to 100 mHz, 5 points per decade, and 10 mV_{rms} sinusoidal potential excitation. The obtained data was then fitted using Gamry E-chem software. The evolution of H_2 gas was monitored for long exposure period (4 hrs) by simple immersion test. To ensure data reproducibility and accuracy, the results of minimum three samples are reported for each electrochemical test.

5.3 Results and Discussion

5.3.1 Microstructure

Fig. 5.1 shows the surface morphology and the corresponding EDS element maps of cast WE43 alloy. The microstructure consists of a solid solution of α-Mg matrix and randomly distributed intermetallic precipitates with high Y, Nd, and Zr content [245], which formed during solidification due to limited solubility of the alloying elements in Mg. These precipitates have three different shapes; longitudinal, cuboidal, and spherical, as indicated in Fig. 5.1(a). The average length of the longitudinal precipitates is 20.6 ± 2.2 μm, while the average size of the cuboidal and the spherical particles is 3.3 ± 0.4 and 5.9 ± 0.4 μm respectively. EDS element maps in Fig. 5.1 (b-f) shows that the longitudinal and spherical precipitates are rich in Nd while the cuboidal particles are rich in both Y and Zr. Table 5.1 summarizes the compositions of these precipitates. It can be seen that indeed the longitudinal and spherical phases has a higher Nd concentration, while the cuboidal phase shower higher Y and Zr content than the α-Mg.

The surface morphology of the as-deposited WE43 thin films (Fig. 5.2) exhibits dense faceted angular structures, which are often associated with the formation of nanocrystalline phase with columnar through thickness grains. EDS analysis in Table 5.1 shows that global composition of the as-deposited thin film is very close to that of the cast alloy. The EDS element maps (Fig. 5.2 b-f) shows that all alloying elements are homogeneously distributed within the α-

Mg matrix, thus exceeding their equilibrium solubility in Mg [246, 247]. Fig. 5.3 shows the GIXRD line scans of the cast and as-deposited samples. The diffraction peaks of the cast alloy indicate the presence of $Mg_{41}Nd_5$ and $Mg_{24}Y_5$ precipitates in addition to α-Mg. While current XRD data base does not include results from Mg-Y-Zr alloy, it is likely that the XRD identified $Mg_{24}Y_5$ phase also contains Zr, as indicated by prior EDS results (Fig. 5.1 and Table 5.1). More work is planned in the future to quantify the structure and composition of these precipitates by detailed TEM study. Nevertheless these phases are consistent with those reported by others from the same alloy [248]. On the other hand, XRD result of the as-deposited WE43 exhibited only α-Mg phase, where the diffraction peaks of the precipitates observed in the cast alloy no longer exist. This result suggests that the fast effective quenching rate during magnetron sputtering leads to the supersaturation of Y, Zr, and Nd in the α-Mg matrix [249, 250], hence eliminating chemical heterogeneity while maintaining the same global composition. It is also interesting to note that the as-deposited WE43 exhibited a high intensity $(11\bar{2}0)$ peak and absence of $(10\bar{1}0)$ and $(10\bar{1}2)$ peaks, suggesting the presence of a strong $(11\bar{2}0)$ fiber texture in the film thickness direction, similar to those reported in other PVD deposited Mg alloy thin films [251].

Fig. 5.4 (a) and (b) show bright-field (BF) and dark-field (DF) TEM images of as-deposited WE43 alloy. The average grain size was 46.6 ± 11.5 nm, measured using line-intercept method from multiple DF images. The SAD pattern (Fig. 5.4(c)) exhibited discrete diffraction rings, corresponding with a single hcp phase, indicating the formation of supersaturated solid solution [34], in agreement with the XRD results.

5.3.2 Potentiodynamic Polarization Tests

Fig. 5.5 shows the representative PD results of the cast and as-deposited WE43 Mg alloys after immersion in blood bank buffered saline for 20 min. The anodic branch of the PD curve

represents the anodic dissolution of Mg, while the cathodic branch represents the cathodic reaction of hydrogen evolution. The inset shows three separately repeated tests for each sample sets. It can be seen from Fig. 5.5 that the as-deposited alloy exhibits a shift of both the anodic and cathodic branches towards lower corrosion current densities (i_{corr}), indicating a decrease in anodic and cathodic kinetics [54, 252]. In addition, the PD curves of both alloys show relatively low Tafel slopes, indicating low polarizability, similarly to those typically observed in Mg alloys [253]. The cast alloy exhibits no evidence of passivity, while the as-deposited alloy is believed to form a protective oxide film on the alloy surface, which fractured at the breakdown potential of -1.4 $V_{Ag/AgCl}$. Beyond this potential, the oxide film can no longer protect the sample [215, 254].

The values of the crossover potentials for zero current ($E_{zero\ current}$) of both alloys scatter around -1.5 $V_{Ag/AgCl}$. These values are slightly higher than that reported for cast WE43 alloy in NaCl aqueous solutions (-1.9 to -1.8 $V_{Ag/AgCl}$), simulated body fluids (SBF) (-1.9 to -1.6 $V_{Ag/AgCl}$) and complete cell culture medium (cDMEM) (-1.7 to -1.6 $V_{Ag/AgCl}$) [210, 215, 216, 230, 255]. The E_{OC} and the electrochemical parameters obtained from the PD tests for both samples are listed in Table 5.2. Due to the asymmetry of the anodic and cathodic branches of the PD curves, in this work the $E_{zero\ current}$ and the nominal (i_{corr}) were estimated by Tafel extrapolation of the cathodic region starting from a potential that is 50 mV cathodic to the E_{OC} of the PD curves [31, 230]. The i_{corr} of the cast and as-deposited WE43 Mg alloys are 99.3 ± 17.0 µA/cm^2 and 12.0 ± 2.1 µA/cm^2, respectively. It is interesting to note that the i_{corr} values of as-deposited alloy reported here is remarkably lower than that of plasma ion implanted WE43 Mg alloy in SBF solution [215, 229, 230]. The corrosion rate in µm/year was estimated by Faradic conversion of the i_{corr} (1 µA/cm^2 corresponds to approx. 22.6 µm/year), considering uniform corrosion of Mg with the formation of Mg^{2+}. It was found that the as-deposited WE43 exhibited ~ 8 fold

reduction in the nominal corrosion rate (272 ± 48 μm/year) compared to the cast alloy (2249 ± 385 μm/year). Additional tests (Fig. 5.6(a)) of the cast alloy, which included a return scan at an apex potential of 300 mV vs. E_{OC} showed a return loop, indicating the susceptibility of the alloy to localized corrosion. Cyclic cathodic polarization scans (Fig. 5.6(b)) show that no hysteresis existed between the forward and reverse curves, thus justifying the chosen scan rate of 1 mV/s during PD tests is appropriate for representing the corrosion kinetics of the alloys.

5.3.3 Electrochemical Impedance Spectroscopy Study

To further evaluate the corrosion mechanism of the cast and as-deposited WE43 Mg alloy, EIS measurements were conducted after E_{OC} stabilization for 15 min in blood bank buffered saline. The Nyquist representation of the results (Fig. 5.7) for both alloys show two overlapping capacitive semicircles. The semicircles at high and low frequency attribute to the mass transport through the oxide/hydroxide layer and charge transfer, respectively. The Nyquist results indicated that both alloy exhibited similar corrosion mechanism, but the significantly larger capacitive loop of the as-deposited alloy compared to that of the cast alloy indicates the enhanced corrosion resistance [210, 230] achieved by reducing the chemical heterogeneity.

The experimental data were fitted using the equivalent circuit model shown as inset in (Fig. 5.7). Constant phase elements (CPEs) were used instead of capacitors due to the depression of the Nyquist curve at low frequencies. Here, Rs represents the ohmic solution resistance, the constant phase elements CPE_1 and CPE_2 represent the capacitive behavior of the oxide/hydroxide layer and charge separation due to hydrogen evolution, respectively. The impedance of the CPE is represented as

$$Z_{CPE} = Y_o^{-1}(j\omega)^{-n}, \tag{5.4}$$

where Yo is a constant, j = (-1)1/2, ω is the angular frequency and n is a real number between 0 and 1. R_1 and R_2 are the resistance of the oxide/hydroxide layer and charge transfer resistance

due to hydrogen evolution reaction, respectively [256, 257]. The polarization resistance R_P was estimated as $R_P = R_1 + R_2$ [257]. As shown in Fig. 5.7, the fitted results closely matched the experimental behavior for much of the frequency range for both alloys. It was found that R_1 for the as-deposited alloy ($3821 \pm 235\ \Omega$) was significantly higher than that of the cast alloy ($27 \pm 12\ \Omega$), indicating the former has much larger resistance against the transportation of the corrosive media through the oxide/hydroxide film. Similarly, R_2 for the as-deposited alloy ($440 \pm 160\ \Omega$) is higher than that of the cast alloy ($188 \pm 76\ \Omega$), confirming the enhanced resistance to Mg dissolution.

The corrosion rate (i_{corr}) from EIS tests was estimated from the R_P using Stern-Geary equation [253, 258]:

$$i_{corr} = B/R_P, \qquad (5.5)$$

where B is the apparent Stern-Geary coefficient with a value of 54 and 73 mV for the cast and as-deposited alloys respectively. These B values were obtained from Tafel extrapolation of the PD tests following the equation:

$$B = \frac{\beta_a \cdot \beta_c}{2.3(\beta_a + \beta_c)}, \qquad (5.6)$$

where β_a and β_c are the anodic and cathodic Tafel slopes, respectively. In this work the value of β_a was estimated to be equal to β_c for the cast alloy. It is also noted here, that the validity of corrosion rates estimated from Stern-Geary equation depends on the correct determination of the coefficient B and whether Mg dissolves directly to Mg^{2+} or through Mg^+ intermediate [57, 253, 259]. Through equations (5) and (6), It was found that the i_{corr} for the as-deposited alloy ($17 \pm 0.3\ \mu A/cm^2$) is much lower than that of the cast alloy ($257 \pm 82\ \mu A/cm^2$), in agreement with the PD tests.

5.3.4 Immersion Test

Finally, the corrosion behavior and H_2 evolution of both alloys in blood bank buffered saline was examined using a high definition camera (1920×1080 pixels, 30 fps) at different time intervals up to 160 min, as shown in Fig. 5.8. It can be seen that during the entire immersion period, the cast alloy developed a much higher amount of hydrogen bubbles and sites of corrosion, compared to the as-deposited alloy. The difference in the amount of bubbles generated from the surface of both alloys during the simple immersion test could be related to their different cathodic kinetics. Such results supported those obtained from the PD test, where it was found that the cathodic kinetics was hindered by minimizing the chemical heterogeneity in the as-deposited alloy. The H_2 bubbles observed at the edges of both samples are similar to that reported by Wu et al. [260] for AZ91D Mg alloy immersed in 0.1 M NaCl solution, and are believed to be not related to the corrosion behavior. It was noted that the as-deposited sample darkened within the first 5 min of immersion, revealing a color similar to the natural color of rare earth elements. Similar behavior was also reported by Wu et al. [69] for lanthanum (La) magnetron sputtered AZ91D Mg alloy. To understand the role of this darkened layer and its formation process, the evolution of Eoc were closely monitored for the first 1,000 sec of the immersion for both samples, as shown in Fig. 5.9. For the deposited sample, the Eoc increased significantly from about −1.67 V vs. Ag/AgCl up to about −1.52 V vs. Ag/AgCl in the first ~150–200 s upon immersion. Such fast increase in Eoc is often associated with passivation of the surface and formation of a surface film [261]. Q-tip was frequently used to scrub the sample surface to introduce local disturbance on the surface film during the immersion. It can be seen that such disturbance has negligible effect on Eoc of the cast alloy. Interestingly, for the as-deposited alloy, once the darkened film formed (after ~ 470 sec), such disturbance lead to a

sudden decrease of Eoc, followed by a gradual recovery once the Q-tip is removed, characteristic of a typical depassivation-repassivation behavior of passive metals [191]. Preliminary scanning Kelvin probe microscopy (SKPM) measurements (not shown here) suggest that the work function of the darkened surface is similar to that of the virgin surface of the as-deposited sample. Thus this surface darkening is believed to have no effect on the surface properties of the as-deposited sample. Detailed characterization of this layer, including the film thickness, composition, and semiconducting properties, is left for future work.

Fig. 5.10 and 5.11 show the surface morphologies and EDS analysis of the cast and as-deposited WE43 alloys after immersion in blood bank buffered saline for 4 hours. The surface morphology of the cast alloy shows thick corrosion product film with extensive dehydration cracks, similar to that reported for the same alloy in Ringer's solution, cell culture and simulated body fluid [229, 230]. Chu and Marquis [261] showed that such films contain a bi-layered porous structure, with an outer porous amorphous $Mg(OH)_2$ layer on top of an inner MgO layer. According to the EDS maps (Fig. 5.10 (b-g)), the regions of corrosion film on the cast alloys were enriched in Zr and Y. This behavior could be related to the micro-galvanic coupling between the α-Mg and the precipitates. Although WE43 contains three different types of precipitates, the Zr-rich phases exhibit the highest Volta potential difference with respect to the α-Mg matrix compared to all other precipitates [261]. Hence during corrosion, the α-Mg will serve as the anode and the Zr-rich precipitates as effective local cathodes. The cathodic reaction then takes place according to Eq. (2),(3) around the Zr-rich phases. In contrast to the cast alloy, the surface of the deposited alloy was still smooth without noticeable corrosion product formation (Fig. 5.11). The EDS analysis (Fig. 5.11 (b-g)) confirmed that all the alloying elements remained in solution after corrosion.

To further examine the corrosion product formed on the cast alloy, cross-section of the corroded region was prepared by FIB milling (Fig. 5.12 (a, c)). Edge rounding and milling debris were minimized by selecting a minimum current (0.3 pA) during the last stages of the milling process. The cracks depth appeared to be ~1.6 μm, obtained by tilting the sample at 40° and applying tilt correction for the measurement. These cracks could serve as open channels that allow the corrosive environment to penetrate into the alloy interior for the corrosion reactions to continue. On the other hand, the as-deposited alloy exhibited dense columnar structure similar to that reported for other magnetron sputtered metallic thin films (Fig 5.12. (b, d)). After 4 hr immersion, the cross-section of the deposited alloy was still uniform in thickness and maintaining good adhesion with the substrate. These observations thus support the results obtained from the electrochemical tests, confirming that eliminating undesirable chemical heterogeneity of the alloy is an effective method to enhance the corrosion resistance of WE43 Mg alloy by minimizing micro-galvanic corrosion.

5.4 Summary and Conclusions

The microstructure and corrosion behavior of deposited WE43 Mg alloy were compared with that of cast alloy having the same global composition. The as-deposited alloy formed a chemically homogeneous supersaturated solid solution with an average grain size of ~ 46 nm. Achieving chemical homogeneity was found to be highly effective in improving the corrosion resistance of WE43 by hindering the anodic and cathodic activities and minimizing undesirable micro-galvanic corrosion, resulting in ~ 8-fold reduction in corrosion rate. Post-corrosion surface characterizations revealed the corrosion products primarily formed above areas enriched in Zr and Y elements. The corrosion product of the cast alloy exhibited a network of dehydration cracks, through which the corrosive media could penetrate towards the interior of the sample. In

contrast, the as-deposited alloy managed to maintain the chemical homogeneity of the pre-corrosion condition. Corrosion was found to proceed in a more uniform fashion in the deposited sample due to the formation of protective surface layer. Finally it should also be pointed out that while the as-deposited alloy was conveniently produced by PVD, it is however a surface technique and in its laboratory form not suitable for producing millimeter sized bulk samples. Nevertheless it is anticipated that the understanding generated here will provide critical design guidance for microstructure optimization in bulk biomedical products produced by other scalable non-equilibrium techniques such as semi-solid casting, rapid solidification, cold spray, electrodeposition, and powder metallurgy.

Table 5.1 Summary of the global and precipitate compositions of cast and as-sputtered Mg-WE43, measured by EDS analysis on polished sample surfaces.

Samples	Mg (wt.%)	Y (wt.%)	Nd (wt.%)	Zr (wt.%)
Cast WE43 (global)	93.1 ± 0.3	3.6 ± 0.5	2.4 ± 0.2	0.6 ± 0.2
Longitudinal/Spherical phase	82.4 ± 4.4	6.6 ± 3.4	7.2 ± 2.6	3.9 ± 0.9
Cuboidal phase	69.1 ± 7	9.2 ± 1.9	3.5 ± 2.1	18.8 ± 4.2
As-deposited WE43 (global)	93.09 ± 0.88	4.67 ± 0.6	1.79 ± 0.35	0.45 ± 0.19

Table 5.2 Electrochemical parameters obtained from PD tests of cast and as-deposited WE43 alloy.

Samples	βa (mV/decade)	βc (mV/decade)	Nominal i_{corr} ($\mu A/cm^2$)	E_{oc} (mV)	B (mV)	Nominal corrosion rate (μm/year)
Cast	35.3 ± 17.2	250.3 ± 15.5	99.3 ± 17	-1510 ± 50	54	2249 ± 385
As-deposited	326.2 ± 21.1	347.7 ± 49.9	12.0 ± 2.1	-1520 ± 50	73	272 ± 48
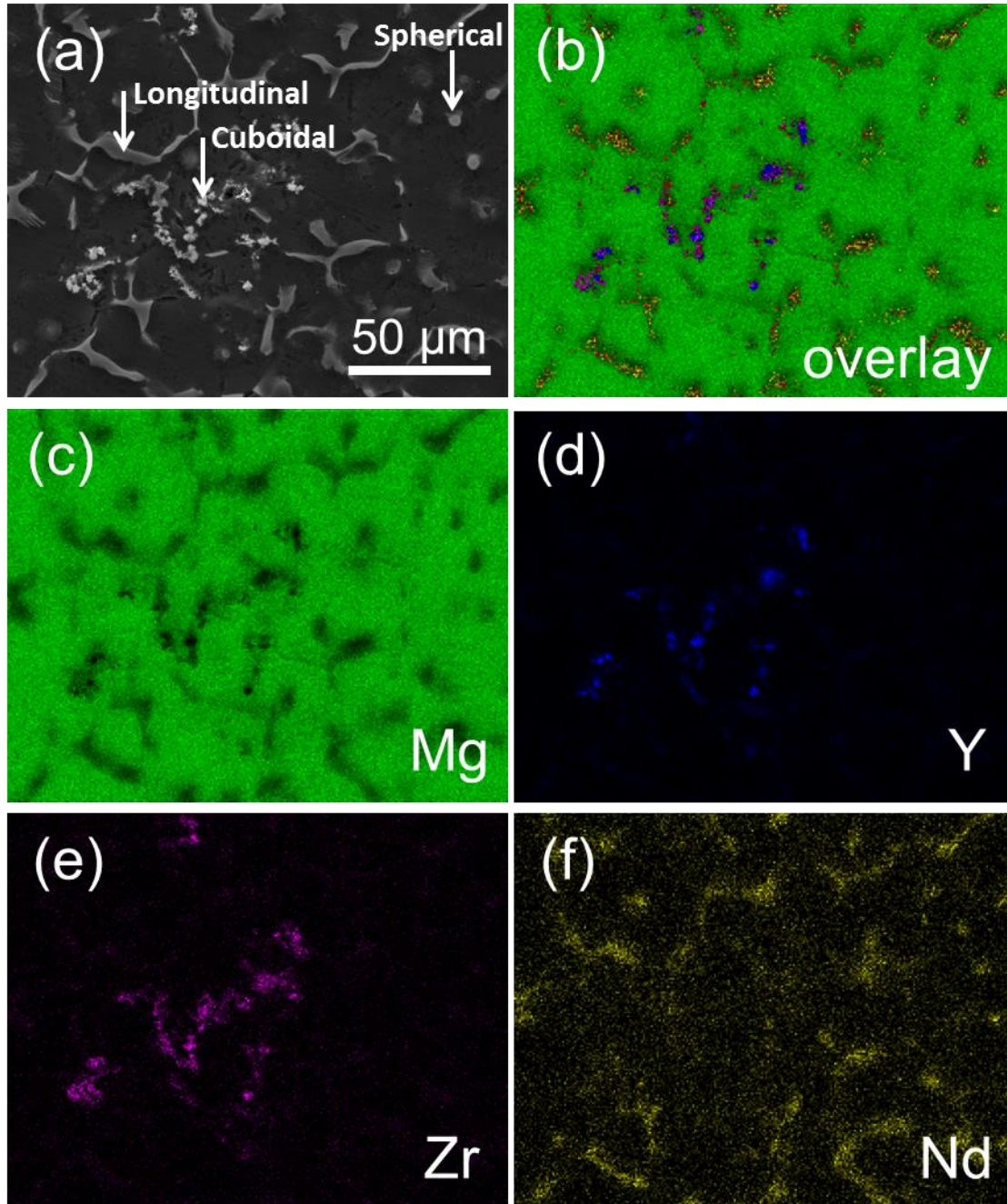
Figure 5.1 (a) SEM image and the corresponding EDS element map of (b) all elements, (c) Mg, (d) Y, (e) Zr, and (f) Nd, obtained from polished cast WE43 alloy.
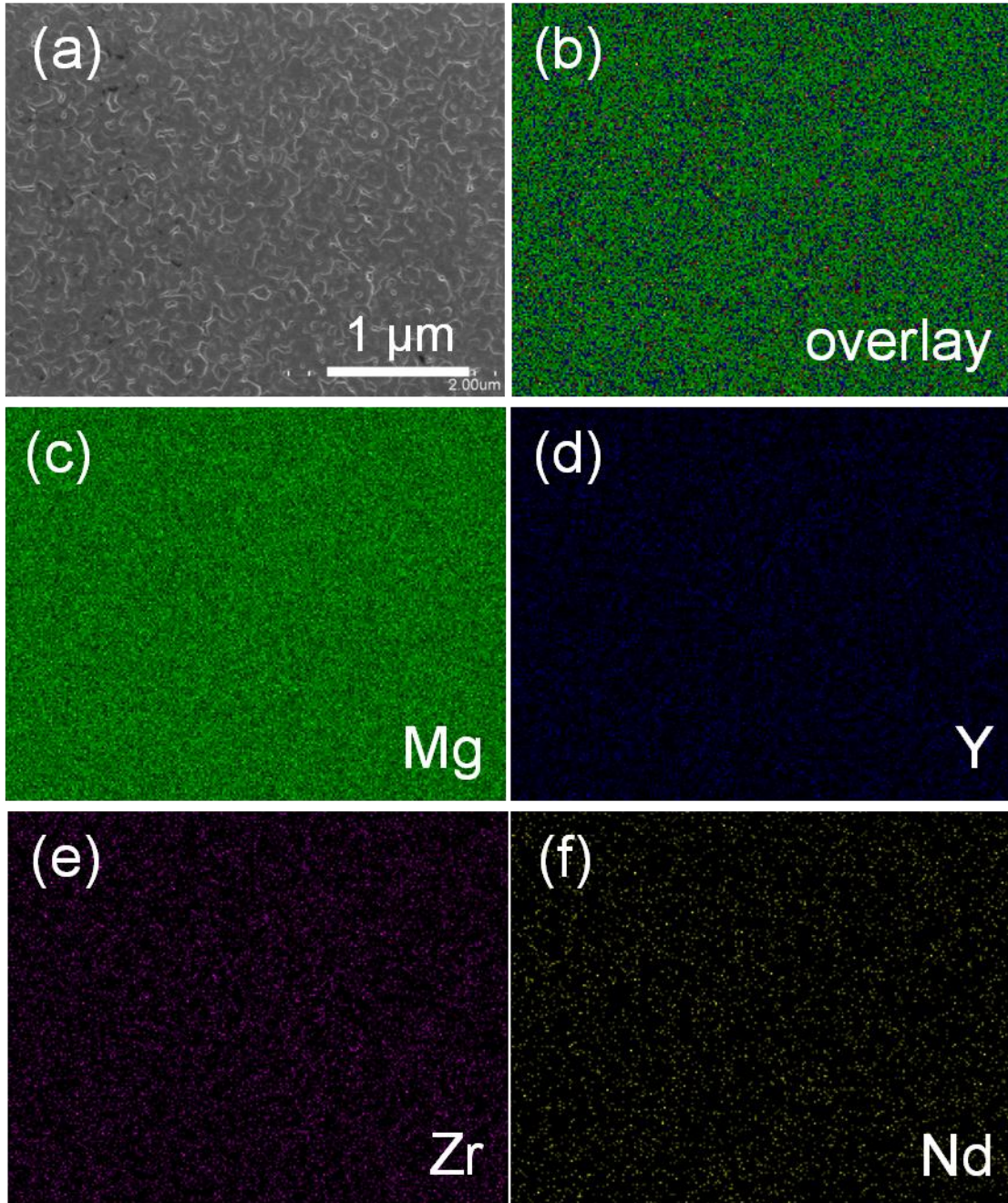
Figure 5.2 (a) Surface SEM image and the corresponding EDS element map of (b) all elements, (c) Mg, (d) Y, (e) Zr, and (f) Nd, obtained from as-deposited WE43 alloy.
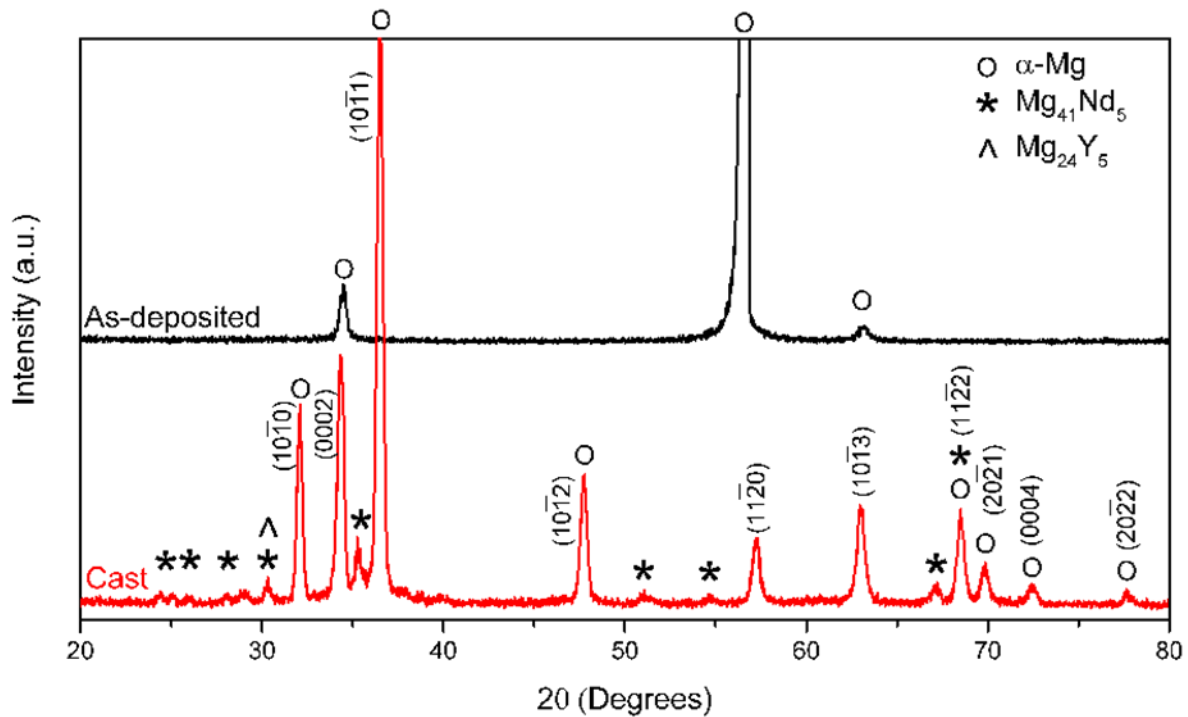
Figure 5.3 GIXRD of cast (red) and as-deposited (black) WE43 alloy.
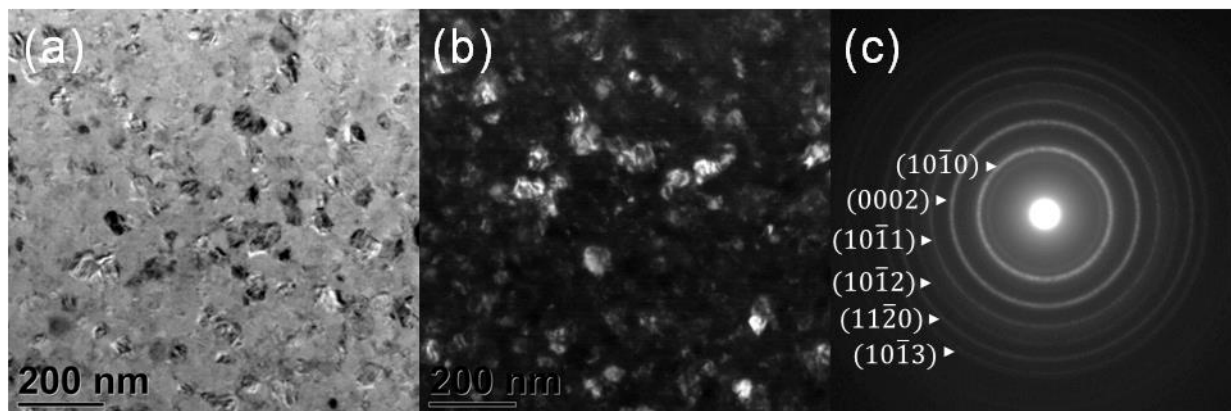
Figure 5.4 (a) Bright field (BF), (b) dark field (DF) TEM images, and (c) the corresponding SAD pattern of as-deposited WE43 thin film.
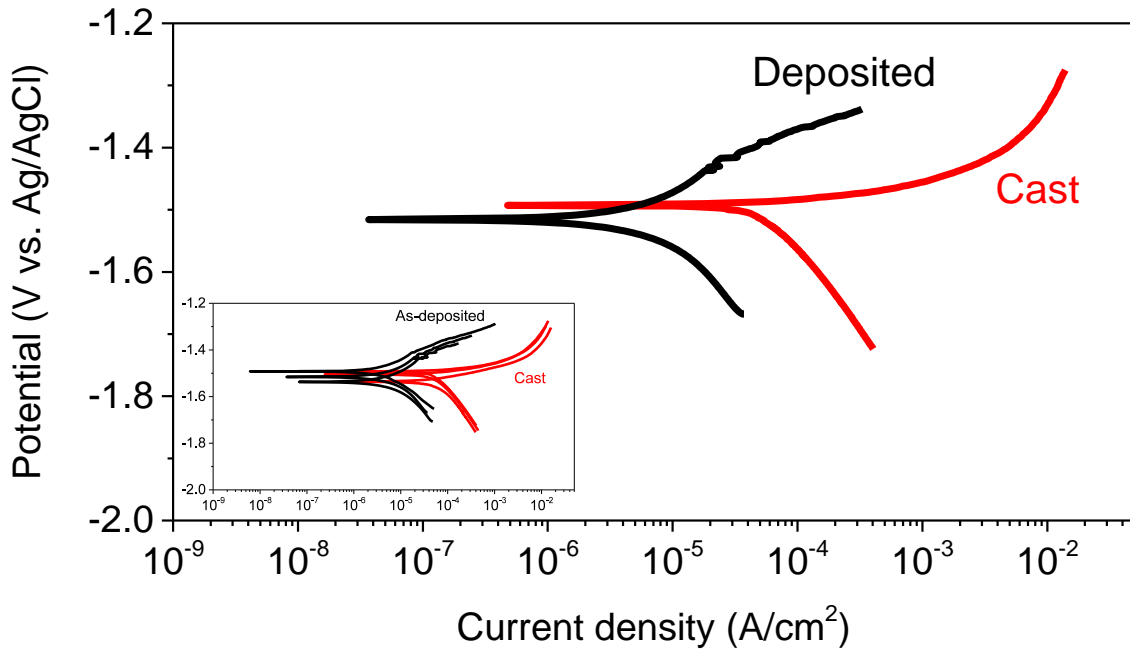
Figure 5.5 Tafel plots of cast and as-deposited WE43 alloy from PD tests after immersion in blood bank buffered saline for 20 min. Inset show PD results from three separate tests for each sample sets.
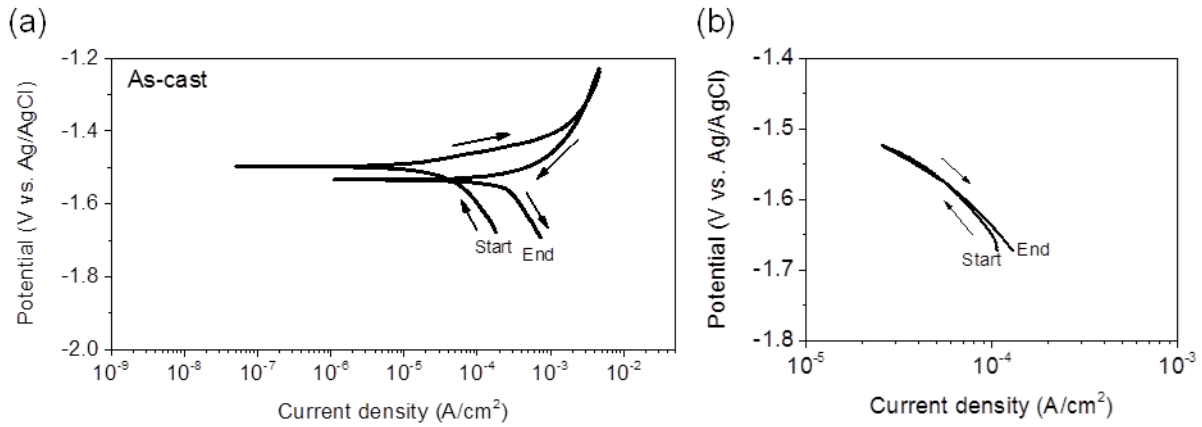
Figure 5.6 (a) Cyclic PD curve, and (b) cyclic cathodic polarization curve of cast WE43 alloy.
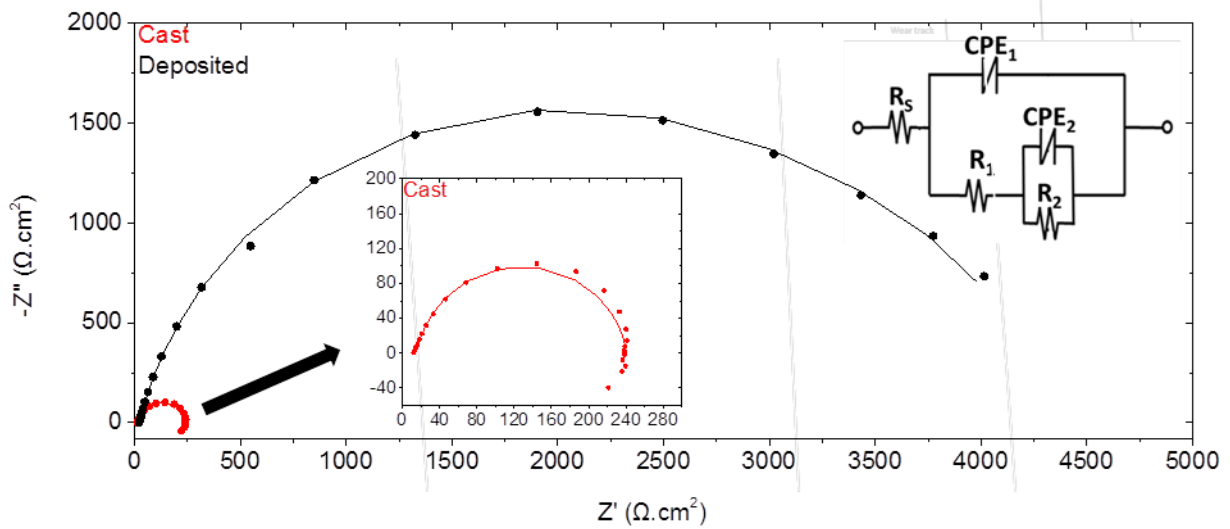
Figure 5.7 Nyquist plots (scattered data) of cast and as-deposited WE43 alloy conducted after EOC stabilization for 15 min in blood bank buffered saline. The top right inset shows the equivalent circuit model used to fit the experimental measurements, as represent
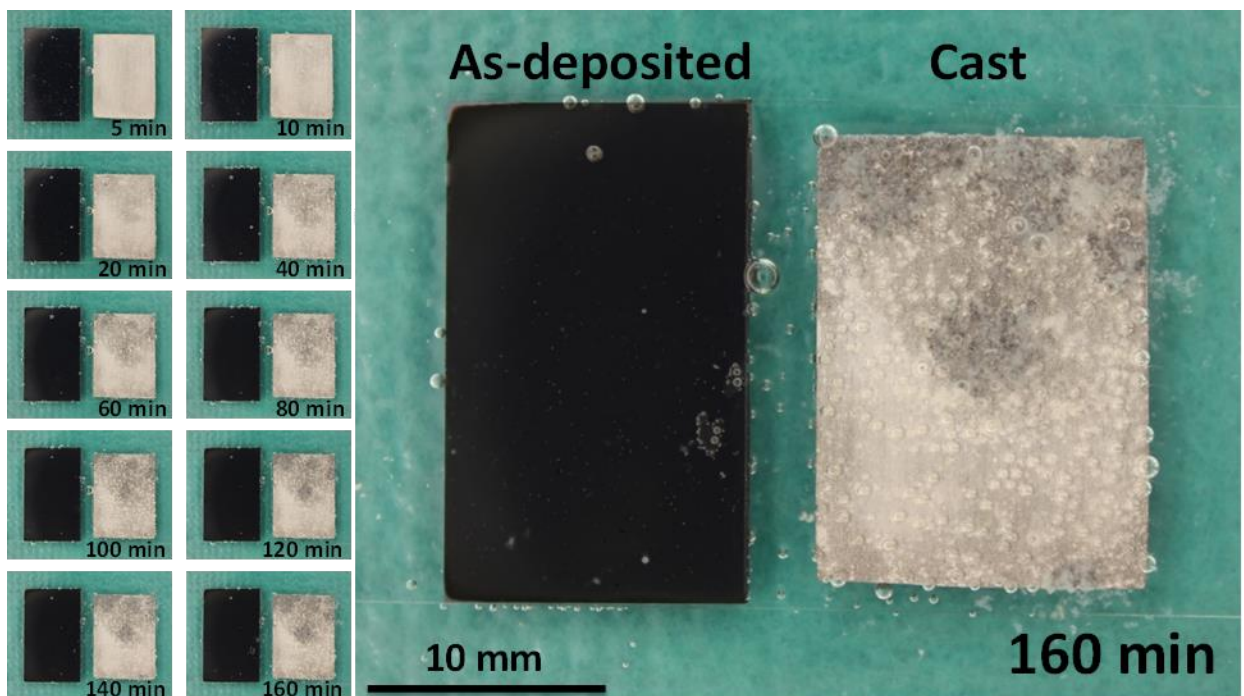
Figure 5.8 Photos taken during immersion tests of as-deposited and cast WE43 alloys up to 160 min in blood bank buffered saline.
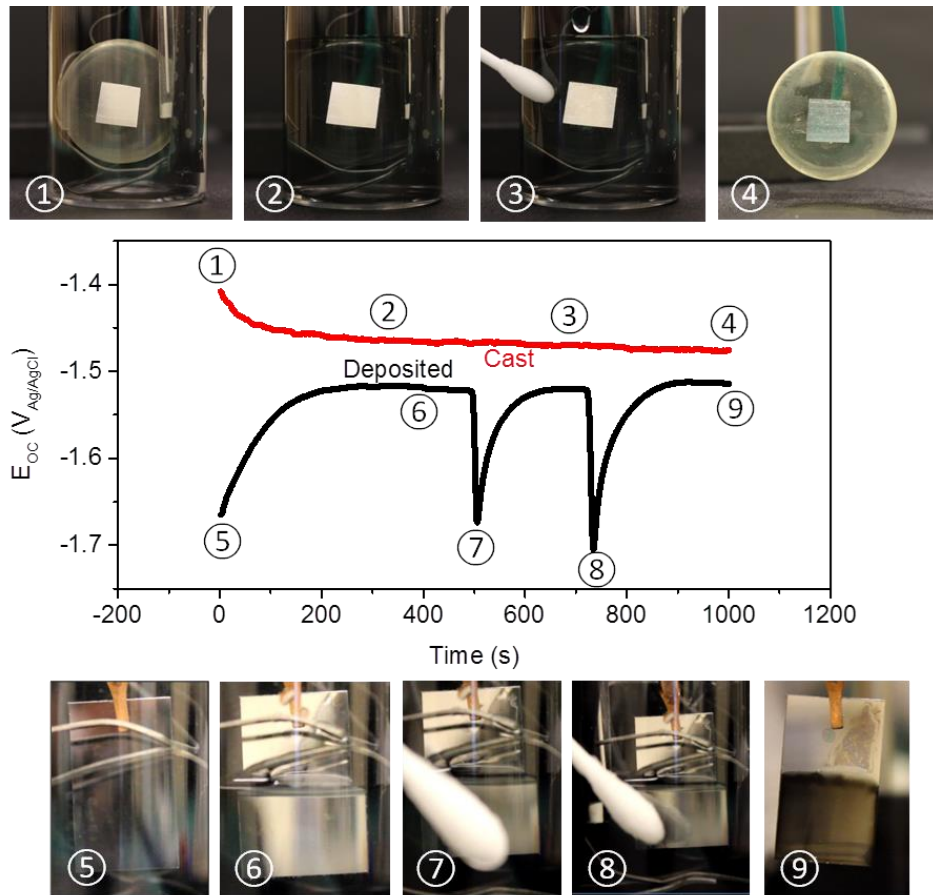
Figure 5.9 Evolution of E_{OC} during immersion test in blood bank buffered saline.
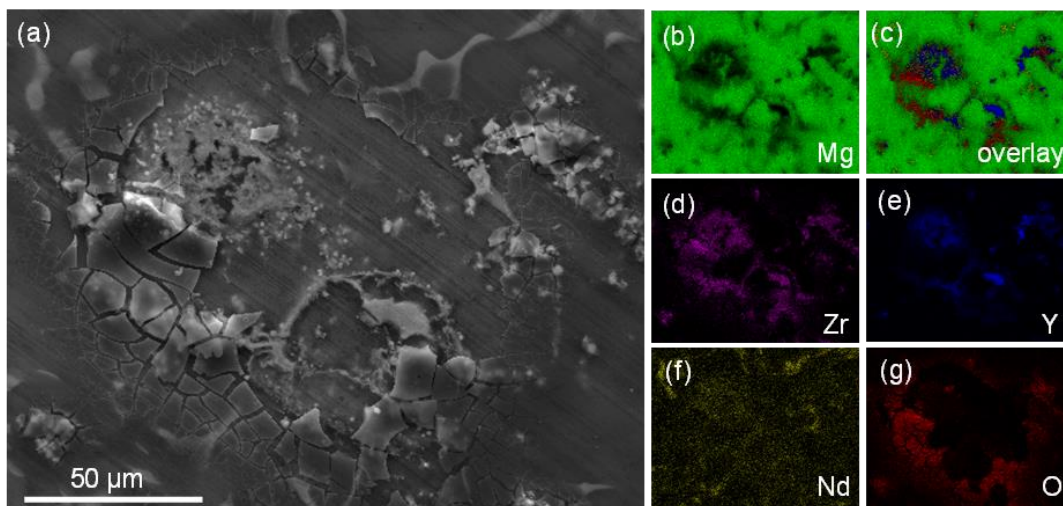
Figure 5.10 (a) Surface SEM image, and (b)-(g) the corresponding element maps of cast WE43 after immersion test for 4 hours. Image (c) is the overlay image including all elements from images (b), and (d)-(g).
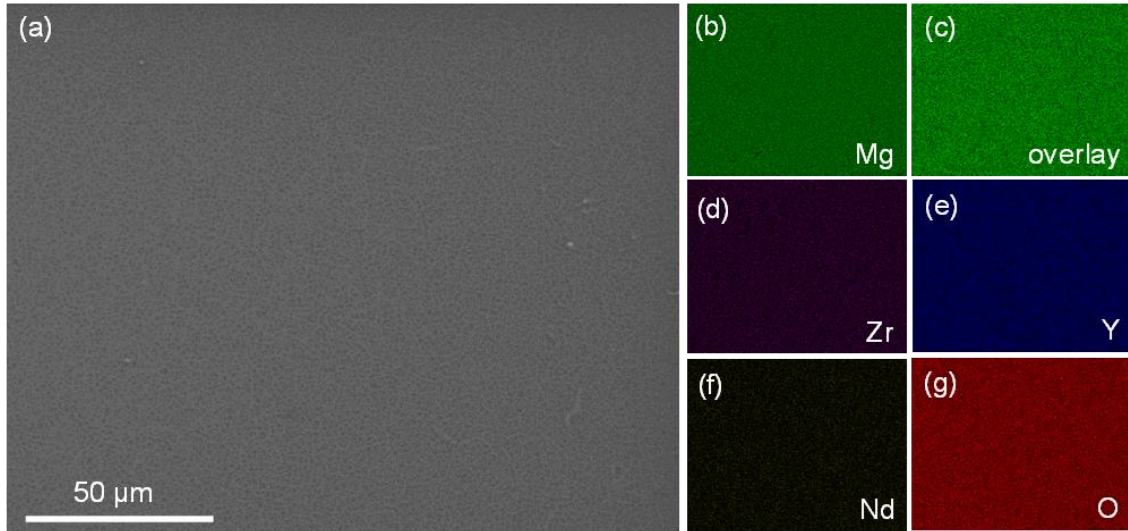
Figure 5.11 (a) Surface SEM image, and (b)-(g) the corresponding element maps of as-deposited WE43 after immersion test for 4 hours. Image (c) is the overlay image including all elements from images (b), and (d)-(g).
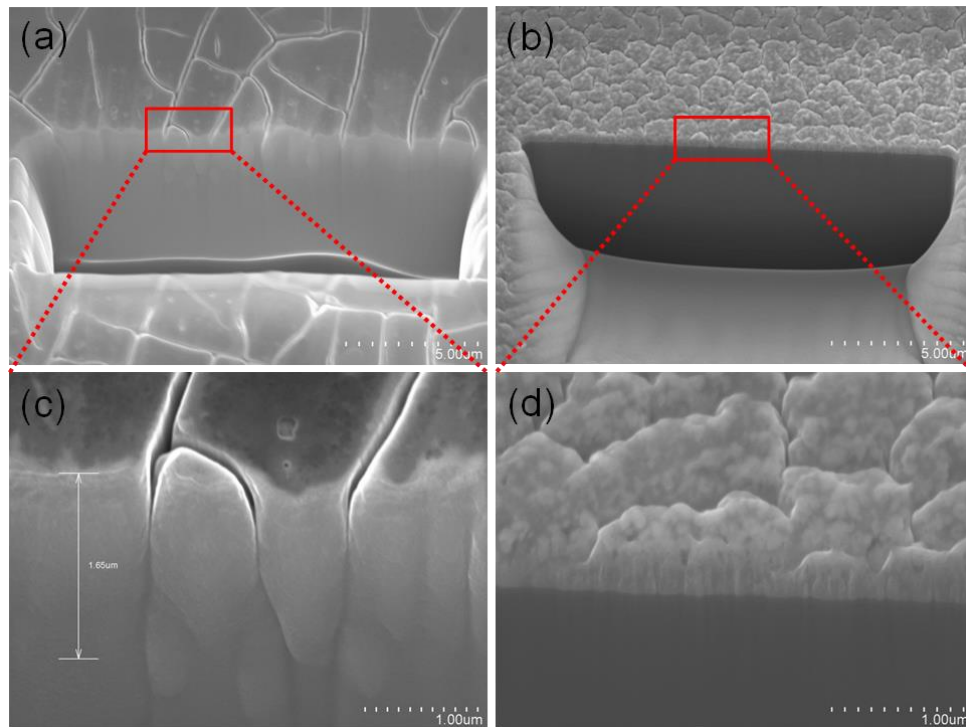
Figure 5.12 Cross-sectional SEM images of (a), (c) cast, and (b), (d) as-deposited WE43 after immersion test for 4 hours. Images (c) and (d) are enlarged from the box area in (a) and (b) respectively. In image (d), the bottom dark area corresponds to the Si substrate.

CHAPTER 6: CONCLUSION AND DIRECTIONS FOR FURTHER RESEARCH

6.1 Conclusions

In this dissertation, the roles of alloy concentration and microstructure on the corrosion and tribocorrosion resistance of two light weight Al and Mg alloys, representing predominantly passive and active dissolution behaviors, respectively, were investigated. Chemically homogeneous super saturated solid solutions of Al-Mn were fabricated under vacuum by magnetron sputtering. Increasing Mn concentration led to the formation of nanocrystalline (5.2 at.% Mn), dual phase (11.5 at.% Mn), and fully amorphous (20.5 at.% Mn) microstructures. The effect of alloy (Mn) concentration on the microstructure, surface morphology, hardness, corrosion, and tribocorrosion resistance was investigated. The pitting potential increased monotonically with increasing alloy concentration. Both, crystalline and amorphous alloys exhibited enhanced corrosion resistance compared to that of pure Al. The decrease in corrosion resistance observed for the dual phase alloy was ascribed to the micro-galvanic coupling between the two co-existent phases (crystalline and amorphous). The amorphous alloy exhibited the best corrosion resistance during short exposure period, while during prolonged exposure duration up to 108 hrs, the crystalline alloy was more stable. It was found that Mn addition enhanced the corrosion resistance of Al by forming a thicker and more compact passive film with less defect density.

Mn addition increased the hardness of Al by solid solution strengthening and structure refinement. Such hardness increment resulted in improved wear and tribocorrosion resistance.

110

The material response during tribocorrosion tests was controlled by the alloy hardness, quality of the passive film, and applied potential. Finally, the Al-Mn system studied here was found to be self-repairing; upon the removal of mechanical load, the depassivated area quickly repassivated, with faster repassivation kinetics at higher Mn content.

The effect of chemical homogeneity on the corrosion resistance of as-cast and magnetron sputtered WE43 Mg alloy was studied in a simulated physiological environment. The formation of chemically homogeneous single phase supper saturated solid solution of Mg-Zr-RE enhanced the corrosion resistance, likely by minimizing the undesirable micro-galvanic corrosion. Post-corrosion surface characterizations of the cast alloy revealed sites of severe corrosion enriched in Zr and Y elements. These sites exhibited a network of cracks (expected to result from dehydration), through which the corrosive medium could penetrate towards the interior of the sample. In contrast, the as-deposited alloy managed to maintain the chemical homogeneity of the pre-corrosion condition. Corrosion was found to proceed in a more uniform fashion in the deposited sample, apparently due to the formation of a protective surface layer.

6.2 Future Work

As discussed earlier, Mn was chosen as the alloying element for studying the effect of alloy concentration and microstructure on the corrosion and tribocorrosion resistance of binary Al alloys based on the following criteria: lubricity of the oxide film, grain boundary segregation enthalpy, and relative atomic radius compared to Al. It would be of great interest if other alloying elements are considered and their effects are compared to that of Mn. In addition to the selection criteria mentioned above, the H/E ratio, pitting potential and defect densities of the passive film should be considered. In tribocorrosion studies, the effects of tribological variables (normal load, sliding speed, alignment, and vibration) and electrochemical variables (applied

potential, ohmic resistance, electrolyte pH etc.) should be evaluated. Quantification of the repassivation rate and the studying of the exact origin of wear-corrosion synergy should be also considered.

The effect of chemical heterogeneity on the corrosion resistance of WE43 alloy was investigated using samples from two different metallurgical structure, cast and magnetron sputtered. This work can be extended by quantifying the effect of grain size and crystallographic texture on the corrosion resistance of WE43 alloy. It is also highly recommended to electrochemically test samples of commercially available biodegradable implants coated with the magnetron sputtered WE43 alloy. The effect of corrosive species such as Cl^- on coating stability and adhesion should be tested. The mechanical properties of both microstructures should be characterized by means of nano-indentation and compared to that of materials currently used. XPS analysis (composition, semiconducting properties, and thickness) of the passive film formed on the deposited alloy should be obtained.

REFERENCES

1.   Cole, G.S. and A.M. Sherman, *Light weight materials for automotive applications.* Materials Characterization, 1995. **35**(1): p. 3-9.
2.   Association, T.A. *Key Sustainability Performance Indicators for the Aluminum Can.* 2017 [cited 2017; Available from: http://www.aluminum.org/aluminum-can-advantage.
3.   Davis, J., *Aluminum and Aluminum Alloys.* 2013.
4.   Caporali, S., et al., *Aluminium electroplated from ionic liquids as protective coating against steel corrosion.* Corrosion Science, 2008. **50**(2): p. 534-539.
5.   Cheng, W.J. and C.J. Wang, *Growth of intermetallic layer in the aluminide mild steel during hot-dipping.* Surface & Coatings Technology, 2009. **204**(6-7): p. 824-828.
6.   Wu, G., X. Zeng, and G. Yuan, *Growth and corrosion of aluminum PVD-coating on AZ31 magnesium alloy.* Materials Letters, 2008. **62**(28): p. 4325-4327.
7.   Pardo, A., et al., *Corrosion protection of Mg/Al alloys by thermal sprayed aluminium coatings.* Applied Surface Science, 2009. **255**(15): p. 6968-6977.
8.   Mao, S., et al., *Corrosion properties of aluminium coatings deposited on sintered NdFeB by ion-beam-assisted deposition.* Applied Surface Science, 2011. **257**(13): p. 5581-5585.
9.   Bielawski, M., *Development of unbalanced magnetron sputtered Al–Mo coatings for cadmium replacement.* Surface and Coatings Technology, 2004. **179**(1): p. 10-17.
10.   Ghali, E., *Corrosion resistance of aluminum and magnesium alloys. [electronic resource] : understanding, performance, and testing.* Wiley series on corrosion. 2010: Hoboken, N.J. : Wiley, c2010.
11.   Survey, G., *Mineral Commodity Summaries 2016.* 2016: Government Printing Office.
12.   Kulekci, M.K., *Magnesium and its alloys applications in automotive industry.* The International Journal of Advanced Manufacturing Technology, 2008. **39**(9-10): p. 851-865.
13.   Eliezer, D., E. Aghion, and F.H. Froes, *Magnesium Science, Technology and Applications.* Advanced Performance Materials, 1998. **5**(3): p. 201-212.
14.   Friedrich, H. and S. Schumann, *Research for a "new age of magnesium" in the automotive industry.* Journal of Materials Processing Technology, 2001. **117**(3): p. 276-281.
15.   Dubé, L. and J.-C. Granry, *The therapeutic use of magnesium in anesthesiology, intensive care and emergency medicine: a review.* Canadian journal of anaesthesia, 2003. **50**(7): p. 732-746.
16.   Ding, Y., et al., *Effects of alloying elements on the corrosion behavior and biocompatibility of biodegradable magnesium alloys: a review.* Journal of materials chemistry B, 2014. **2**(14): p. 1912-1933.
17.   Witte, F., et al., *Degradable biomaterials based on magnesium corrosion.* Current Opinion in Solid State and Materials Science, 2008. **12**(5–6): p. 63-72.

18.   Witte, F., et al., *Biodegradable magnesium scaffolds: Part 1: appropriate inflammatory response.* Journal of biomedical materials research Part A, 2007. **81**(3): p. 748-756.

19.   Witte, F., et al., *Biodegradable magnesium scaffolds: Part II: Peri‐implant bone remodeling.* Journal of biomedical materials research Part A, 2007. **81**(3): p. 757-765.

20.   Brar, H.S., et al., *Magnesium as a biodegradable and bioabsorbable material for medical implants.* JOM, 2009. **61**(9): p. 31-34.

21.   Heublein, B., et al., *Biocorrosion of magnesium alloys: a new principle in cardiovascular implant technology?* Heart, 2003. **89**(6): p. 651-656.

22.   Di Mario, C., et al., *Drug‐eluting bioabsorbable magnesium stent.* Journal of Interventional Cardiology, 2004. **17**(6): p. 391-395.

23.   Waksman, R., et al., *Safety and efficacy of bioabsorbable magnesium alloy stents in porcine coronary arteries.* Catheterization and Cardiovascular Interventions, 2006. **68**(4): p. 607-617.

24.   Bosiers, M., et al., *First clinical application of absorbable metal stents in the treatment of critical limb ischemia: 12-month results.* Vasc Dis Manage, 2005. **2**(4): p. 86-91.

25.   Gellings, P.J., *Introduction to Corrosion Prevention and Control.* 1985: Delft University Press.

26.   Gerhardus H Koch, M.P.H.B., Neil G. Thompson, Y. Paul Virmani, J.H. Payer *Historical Congressional Study: Corrosion Costs and Preventative Strategies in the United States.* Materials Performance, 2002.

27.   Jacobson, G., *International Measures of Prevention, Application and Economics of Corrosion Technology (IMPACT).* Materilas Performance, 2016.

28.   Fontana, M. and N. Greene, *Corrosion engineering.* 1978.

29.   Perez, N., *Electrochemistry and corrosion science.* Vol. 412. 2004: Springer.

30.   Paital, S.R., et al., *Improved corrosion and wear resistance of Mg alloys via laser surface modification of Al on AZ31B.* Surface and Coatings Technology, 2012. **206**(8–9): p. 2308-2315.

31.   McCafferty, E., *Validation of corrosion rates measured by the Tafel extrapolation method.* Corrosion Science, 2005. **47**(12): p. 3202-3215.

32.   Hamdy, A.S., E. El-Shenawy, and T. El-Bitar, *Electrochemical impedance spectroscopy study of the corrosion behavior of some niobium bearing stainless steels in 3.5% NaCl.* International Journal of Electrochemical Science, 2006. **1**(4): p. 171-80.

33.   Macdonald, J.R. and E. Barsoukov, *Impedance spectroscopy: theory, experiment, and applications.* History, 2005. **1**(8).

34.   Mraied, H., W. Cai, and A.A. Sagüés, *Corrosion resistance of Al and Al–Mn thin films.* Thin Solid Films, 2016. **615**: p. 391-401.

35.   Davis, J.R., *Corrosion of aluminum and aluminum alloys.* 1999: Asm International.

36.   Moon, S.M. and S.I. Pyun, *The corrosion of pure aluminium during cathodic polarization in aqueous solutions.* Corrosion Science, 1997. **39**(2): p. 399-408.

37.   Szklarska-Smialowska, Z., *Pitting corrosion of aluminum.* Corrosion Science, 1999. **41**(9): p. 1743-1767.

38.   Hagyard, T. and J.R. Williams, *Potential of aluminium in aqueous chloride solutions. Part 1.* Transactions of the Faraday Society, 1961. **57**(0): p. 2288-2294.

39.   Frankenthal, R.P. and J. Kruger, *Passivity of metals.* 1978.

40.   Lepper, K., et al., *Sliding behavior of selected aluminum alloys.* Wear, 1997. **203**: p. 46-56.

41.   Vargel, C., *Corrosion of Aluminium*. 2004 Elsevier Science.

42.   Kim, Y. and R.G. Buchheit, *A characterization of the inhibiting effect of Cu on metastable pitting in dilute Al-Cu solid solution alloys*. Electrochimica Acta, 2007. **52**(7): p. 2437-2446.

43.   Kim, Y., R.G. Buchheit, and P.G. Kotula, *Effect of alloyed Cu on localized corrosion susceptibility of Al-Cu solid solution alloys-Surface characterization by XPS and STEM*. Electrochimica Acta, 2010. **55**(24): p. 7367-7375.

44.   Sanchette, F., et al., *Nanostructured aluminium based coatings deposited by electron-beam evaporative PVD*. Thin Solid Films, 2009. **518**(5): p. 1575-1580.

45.   Merl, D.K., P. Panjan, and I. Milosev, *Effect of tungsten content on properties of PVD sputtered Al-W-X alloys*. Surface Engineering, 2013. **29**(4): p. 281-286.

46.   Macdonald, D.D., *Passivity - the key to our metals-based civilization*. Pure and Applied Chemistry, 1999. **71**(6): p. 951-978.

47.   Crossland, A.C., et al., *Formation of manganese-rich layers during anodizing of Al-Mn alloys*. Corrosion Science, 1999. **41**(10): p. 2053-2069.

48.   E.H. Hollingsworth, H.H., *Metals Handbook*. ASM International. Vol. V.13. 1987. 583.

49.   Nis¸ancioğlu, K., *Electrochemical Behavior of Aluminum-Base Intermetallics Containing Iron*. Journal of The Electrochemical Society, 1990. **137**(1): p. 69-77.

50.   Mazurkiewicz, B. and A. Piotrowski, *The electrochemical behaviour of the Al2Cu intermetallic compound*. Corrosion Science, 1983. **23**(7): p. 697-707.

51.   Song, G.L. and A. Atrens, *Corrosion mechanisms of magnesium alloys*. Advanced engineering materials, 1999. **1**(1): p. 11-33.

52.   Makar, G. and J. Kruger, *Corrosion of magnesium*. International Materials Reviews, 1993. **38**(3): p. 138-153.

53.   Thomas, S., et al., *Corrosion mechanism and hydrogen evolution on Mg*. Current Opinion in Solid State and Materials Science, 2015. **19**(2): p. 85-94.

54.   Gusieva, K., et al., *Corrosion of magnesium alloys: the role of alloying*. International Materials Reviews, 2015. **60**(3): p. 169-194.

55.   Frankel, G.S., A. Samaniego, and N. Birbilis, *Evolution of hydrogen at dissolving magnesium surfaces*. Corrosion Science, 2013. **70**: p. 104-111.

56.   Gomberg, M., *The reducing effect of the binary system (MgX2 + Mg) upon organic compounds in anhydrous solvents*. Recueil des Travaux Chimiques des Pays-Bas, 1929. **48**(8): p. 847-851.

57.   Petty, R.L., A.W. Davidson, and J. Kleinberg, *The Anodic Oxidation of Magnesium Metal: Evidence for the Existence of Unipositive Magnesium1,2*. Journal of the American Chemical Society, 1954. **76**(2): p. 363-366.

58.   Samaniego, A., B.L. Hurley, and G.S. Frankel, *On the evidence for univalent Mg*. Journal of Electroanalytical Chemistry, 2015. **737**: p. 123-128.

59.   Song, G., et al., *The anodic dissolution of magnesium in chloride and sulphate solutions*. Corrosion Science, 1997. **39**(10–11): p. 1981-2004.

60.   Natta, M.G.L.-B., *Evidence of Two Anodic Processes in the Polarization Curves of Magnesium in Aqueous Media*. Corrosion, 2001. **57**(8): p. 712-720.

61.   Nordlien, J.H., et al., *Morphology and structure of oxide films formed on MgAl alloys by exposure to air and water*. Journal of The Electrochemical Society, 1996. **143**(8): p. 2564-2572.

62.   Phillips, R.C. and J.R. Kish, *Nature of Surface Film on Matrix Phase of Mg Alloy AZ80 Formed in Water.* Corrosion, 2013. **69**(8): p. 813-820.

63.   Danaie, M., et al., *The role of aluminum distribution on the local corrosion resistance of the microstructure in a sand-cast AM50 alloy.* Corrosion Science, 2013. **77**: p. 151-163.

64.   Jönsson, M., D. Persson, and R. Gubner, *The Initial Steps of Atmospheric Corrosion on Magnesium Alloy AZ91D.* Journal of The Electrochemical Society, 2007. **154**(11): p. C684-C691.

65.   Okamoto, H., *Phase diagrams for binary alloys.* ASM International, 2010. **44**.

66.   Südholz, A., et al., *Electrochemical properties of intermetallic phases and common impurity elements in magnesium alloys.* Electrochemical and Solid-State Letters, 2011. **14**(2): p. C5-C7.

67.   Kainer, K.U., et al., *3.09 - Corrosion of Magnesium and its Alloys A2 - Cottis, Bob*, in *Shreir's Corrosion*, M. Graham, et al., Editors. 2010, Elsevier: Oxford. p. 2011-2041.

68.   Liu, M., et al., *Calculated phase diagrams and the corrosion of die-cast Mg–Al alloys.* Corrosion Science, 2009. **51**(3): p. 602-619.

69.   Dargusch, M.S., et al., *The effect of aluminium content on the mechanical properties and microstructure of die cast binary magnesium-aluminium alloys.* MATERIALS TRANSACTIONS, 2006. **47**(4): p. 977-982.

70.   Hoyer, P., et al., *Influence of aluminium on the corrosion behaviour of binary magnesium–aluminium alloys in saline solutions.* Materials and Corrosion, 2014. **65**(1): p. 23-30.

71.   Song, G., et al., *Corrosion behaviour of AZ21, AZ501 and AZ91 in sodium chloride.* Corrosion Science, 1998. **40**(10): p. 1769-1791.

72.   Gusieva, K., et al., *Influence of Low Level Ag Additions on Mg-Alloy AZ91.* Advanced engineering materials, 2013. **15**(6): p. 485-490.

73.   Südholz, A.D., et al., *Corrosion behaviour of Mg-alloy AZ91E with atypical alloying additions.* Journal of Alloys and Compounds, 2009. **471**(1–2): p. 109-115.

74.   McNulty, R.E. and J.D. Hanawalt, *Some Corrosion Characteristics of High Purity Magnesium Alloys.* Transactions of The Electrochemical Society, 1942. **81**(1): p. 423-433.

75.   Rokhlin, L.L., *Magnesium alloys containing rare earth metals: structure and properties.* 2003: Crc Press.

76.   Seitz, J.M., et al., *Characterization of MgNd2 alloy for potential applications in bioresorbable implantable devices.* Acta Biomaterialia, 2012. **8**(10): p. 3852-3864.

77.   Wang, Q., et al., *Rare-earth-incorporated polymeric vector for enhanced gene delivery.* Biomaterials, 2014. **35**(1): p. 479-488.

78.   Zhang, T., et al., *Corrosion of hot extrusion AZ91 magnesium alloy. Part II: Effect of rare earth element neodymium (Nd) on the corrosion behavior of extruded alloy.* Corrosion Science, 2011. **53**(9): p. 2934-2942.

79.   Takenaka, T., et al., *Improvement of corrosion resistance of magnesium metal by rare earth elements.* Electrochimica Acta, 2007. **53**(1): p. 117-121.

80.   Arrabal, R., et al., *Corrosion behaviour of AZ91D and AM50 magnesium alloys with Nd and Gd additions in humid environments.* Corrosion Science, 2012. **55**: p. 351-362.

81.   Zhang, J., et al., *Effect of Nd on the microstructure, mechanical properties and corrosion behavior of die-cast Mg–4Al-based alloy.* Journal of Alloys and Compounds, 2008. **464**(1–2): p. 556-564.

82.   Feyerabend, F., et al., *Evaluation of short-term effects of rare earth and other elements used in magnesium alloys on primary cells and cell lines.* Acta Biomaterialia, 2010. **6**(5): p. 1834-1842.

83.   Kirkland, N.T., et al., *A survey of bio-corrosion rates of magnesium alloys.* Corrosion Science, 2010. **52**(2): p. 287-291.

84.   Wang, P.C., et al., *Effects of 2 mass% Li Addition on the AZ80 Mg Alloy.* MATERIALS TRANSACTIONS, 2008. **49**(5): p. 913-917.

85.   Balogh, L., et al., *The contributions of grain size, dislocation density and twinning to the strength of a magnesium alloy processed by ECAP.* Materials Science and Engineering: A, 2010. **528**(1): p. 533-538.

86.   Orlov, D., et al., *Enhanced corrosion resistance of Mg alloy ZK60 after processing by integrated extrusion and equal channel angular pressing.* Acta Materialia, 2011. **59**(15): p. 6176-6186.

87.   Birbilis, N., et al., *Grain character influences on corrosion of ECAPed pure magnesium.* Corrosion Engineering Science and Technology, 2010. **45**(3): p. 224-230.

88.   Liao, J., M. Hotta, and N. Yamamoto, *Corrosion behavior of fine-grained AZ31B magnesium alloy.* Corrosion Science, 2012. **61**: p. 208-214.

89.   Song, G., A. Atrens, and M. Dargusch, *Influence of microstructure on the corrosion of diecast AZ91D.* Corrosion Science, 1998. **41**(2): p. 249-273.

90.   Liao, J., et al., *Atmospheric corrosion of two field-exposed AZ31B magnesium alloys with different grain size.* Corrosion Science, 2013. **71**: p. 53-61.

91.   op't Hoog, C., N. Birbilis, and Y. Estrin, *Corrosion of Pure Mg as a Function of Grain Size and Processing Route.* Advanced engineering materials, 2008. **10**(6): p. 579-582.

92.   Argade, G.R., S.K. Panigrahi, and R.S. Mishra, *Effects of grain size on the corrosion resistance of wrought magnesium alloys containing neodymium.* Corrosion Science, 2012. **58**: p. 145-151.

93.   Ralston, K.D., G. Williams, and N. Birbilis, *Effect of pH on the Grain Size Dependence of Magnesium Corrosion.* Corrosion, 2012. **68**(6): p. 507-517.

94.   Fu, B.-Q., W. Liu, and Z.-L. Li, *Calculation of the surface energy of hcp-metals with the empirical electron theory.* Applied Surface Science, 2009. **255**(23): p. 9348-9357.

95.   Landolt, D. and S. Mischler, *Tribocorrosion of passive metals and coatings*. 2011: Elsevier.

96.   Landolt, D., S. Mischler, and M. Stemp, *Electrochemical methods in tribocorrosion: a critical appraisal.* Electrochimica Acta, 2001. **46**(24–25): p. 3913-3929.

97.   Mischler, S., *Sliding tribo-corrosion of passive metals: mechanisms and modeling*, in *Tribo-Corrosion: Research, Testing, and Applications*. 2013, ASTM International.

98.   *ASTM G40-10b, Standard Terminology Relating to Wear and Erosion*. Annual Book of ASTM Standards. Vol. 03.02. 2010, West Conshohocken, PA: ASTM International.

99.   Dearnley, P.A. and G. Aldrich-Smith, *Corrosion–wear mechanisms of hard coated austenitic 316L stainless steels.* Wear, 2004. **256**(5): p. 491-499.

100.   Wolf, D., et al., *Deformation of nanocrystalline materials by molecular-dynamics simulation: relationship to experiments?* Acta Materialia, 2005. **53**(1): p. 1-40.

101.   Rupert, T.J. and C.A. Schuh, *Sliding wear of nanocrystalline Ni–W: Structural evolution and the apparent breakdown of Archard scaling.* Acta Materialia, 2010. **58**(12): p. 4137-4148.

102. Oltra, R., *Electrochemical aspects of localized depassivation during abrasion of passive iron-based alloys in acidic media*. Wear-Corrosion Interactions in Liquid Media, ed. A. Sagüés and E. Meletis. 1991, Warrandale, PA: The Minerals, Metals and Materiasl Society.

103. Asmussen, R.M., *The Influence of Microstructure on the Corrosion of Magnesium Alloys*, 2014, The University of Western Ontario.

104. Kainer, K.U., *Magnesium alloys and technology*. 2003: John Wiley & Sons.

105. Kek Merl, D., P. Panjan, and J. Kovač, *Corrosion and surface study of sputtered Al–W coatings with a range of tungsten contents*. Corrosion Science, 2013. **69**: p. 359-368.

106. Creus, J., A. Billard, and F. Sanchette, *Corrosion behaviour of amorphous Al–Cr and Al–Cr–(N) coatings deposited by dc magnetron sputtering on mild steel substrate*. Thin Solid Films, 2004. **466**(1–2): p. 1-9.

107. Creus, J., et al., *Reactivity classification in saline solution of magnetron sputtered or EBPVD pure metallic, nitride and Al-based alloy coatings*. Corrosion Science, 2012. **57**: p. 162-173.

108. Perez, A., et al., *Influence of metallurgical states on the corrosion behaviour of Al–Zn PVD coatings in saline solution*. Corrosion Science, 2013. **74**: p. 240-249.

109. Frankel, G.S., et al., *On the Pitting Resistance of Sputter-Deposited Aluminum Alloys*. Journal of The Electrochemical Society, 1993. **140**(8): p. 2192-2197.

110. Metikoš-Huković, M., et al., *Corrosion resistance of amorphous aluminium–molybdenum alloys in an acidic chloride environment*. Corrosion Science, 2010. **52**(2): p. 352-359.

111. Frankel, G.S., et al., *Pitting of Sputtered Aluminum Alloy Thin Films*. Journal of The Electrochemical Society, 1989. **136**(4): p. 1243-1244.

112. Shaw, B., et al., *The influence of tungsten on the pitting of aluminum films*. Journal of The Electrochemical Society, 1990. **137**(4): p. 1317-1318.

113. Yun, J.H. and S.W. Rhee, *Effect of carrier gas on metal-organic chemical vapour deposition of aluminium from dimethylethylamine alane*. Journal of Materials Science-Materials in Electronics, 1998. **9**(1): p. 1-4.

114. Creus, J., et al., *Corrosion behaviour of Al/Ti coating elaborated by cathodic arc PVD process onto mild steel substrate*. Thin Solid Films, 1999. **346**(1–2): p. 150-154.

115. Murray, J.L., et al., *Stable and Metastable Phase-Equilibria in the Al-Mn System*. Metallurgical Transactions a-Physical Metallurgy and Materials Science, 1987. **18**(3): p. 385-392.

116. Ruan, S. and C.A. Schuh, *Electrodeposited Al–Mn alloys with microcrystalline, nanocrystalline, amorphous and nano-quasicrystalline structures*. Acta Materialia, 2009. **57**(13): p. 3810-3822.

117. Grushko, B. and G. Stafford, *Phase formation in electrodeposited and thermally annealed Al-Mn alloys*. Metallurgical Transactions A, 1990. **21**(11): p. 2869-2879.

118. Moffat, T.P., G.R. Stafford, and D.E. Hall, *Pitting Corrosion of Electrodeposited Aluminum-Manganese Alloys*. Journal of The Electrochemical Society, 1993. **140**(10): p. 2779-2786.

119. Zhang, J., et al., *Corrosion behaviors of Zn/Al–Mn alloy composite coatings deposited on magnesium alloy AZ31B (Mg–Al–Zn)*. Electrochimica Acta, 2009. **55**(2): p. 560-571.

120. Reffass, M., et al., *Corrosion behaviour of magnetron-sputtered Al1-x-Mn-x coatings in neutral saline solution*. Corrosion Science, 2010. **52**(11): p. 3615-3623.

121. Liu, X.J., et al., *Thermodynamic assessment of the Aluminum-Manganese (Al-Mn) binary phase diagram.* Journal of Phase Equilibria, 1999. **20**(1): p. 45-56.

122. Ruan, S. and C.A. Schuh, *Mesoscale structure and segregation in electrodeposited nanocrystalline alloys.* Scripta Materialia, 2008. **59**(11): p. 1218-1221.

123. Cai, W. and C.A. Schuh, *Tuning nanoscale grain size distribution in multilayered Al–Mn alloys.* Scripta Materialia, 2012. **66**(3–4): p. 194-197.

124. Akhoondan, M. and A.A. Sagues, *Corrosion Mechanism of Aluminized Steel in Limestone Backfill.* Corrosion, 2013. **69**(12): p. 1147-1157.

125. Stern, M. and A.L. Geary, *Electrochemical Polarization: I . A Theoretical Analysis of the Shape of Polarization Curves.* Journal of The Electrochemical Society, 1957. **104**(1): p. 56-63.

126. Jones, D.A., *Principles and prevention of corrosion.* 1992: New York : Macmillan Pub. Co. ; Toronto : Collier Macmillan Canada ; New York : Maxwell Macmillan International Pub. Group, c1992.

127. Sagüés, A.A., S.C. Kranc, and E.I. Moreno, *The time-domain response of a corroding system with constant phase angle interfacial component: Application to steel in concrete.* Corrosion Science, 1995. **37**(7): p. 1097-1113.

128. Scully, J.R., D.C. Silverman, and M.W. Kendig, *Electrochemical impedance : analysis and interpretation*. STP: 1188. 1993: Philadelphia : ASTM, c1993.

129. González, J.A., et al., *Characterization of porous aluminium oxide films from a.c. impedance measurements.* Journal of Applied Electrochemistry, 1999. **29**(2): p. 229-238.

130. Mccafferty, E., *The Electrode-Kinetics of Pit Initiation on Aluminum.* Corrosion Science, 1995. **37**(3): p. 481-492.

131. Sweitzer, J.E., G.J. Shiflet, and J.R. Scully, *Localized corrosion of Al90Fe5Gd5 and Al87Ni8.7Y4.3 alloys in the amorphous, nanocrystalline and crystalline states: resistance to micrometer-scale pit formation.* Electrochimica Acta, 2003. **48**(9): p. 1223-1234.

132. Li, W., H.L. Su, and J. Yue, *Effects of crystallization on corrosion resistance and electron work function of Zr65Al7.5Cu17.5Ni10 amorphous alloys.* Philosophical Magazine Letters, 2013. **93**(3): p. 130-137.

133. Ruan, S.Y., et al., *Gallium-enhanced phase contrast in atom probe tomography of nanocrystalline and amorphous Al-Mn alloys.* Ultramicroscopy, 2011. **111**(8): p. 1062-1072.

134. Meng, G.Z., et al., *Effect of microcrystallization on pitting corrosion of pure aluminium.* Corrosion Science, 2009. **51**(9): p. 2151-2157.

135. Matsui, I., et al., *Fabrication of bulk nanocrystalline Al electrodeposited from a dimethylsulfone bath.* Materials Science and Engineering: A, 2012. **550**: p. 363-366.

136. Macdonald, D.D., *Passivity–the key to our metals-based civilization.* Pure and Applied Chemistry, 1999. **71**(6): p. 951-978.

137. Pokhmurs'kyi, V.I. and V.M. Dovhunyk, *Tribocorrosion of stainless steels (Review).* Materials Science, 2010. **46**(1): p. 87-96.

138. Landolt, D., *Electrochemical and materials aspects of tribocorrosion systems.* Journal of Physics D: applied physics, 2006. **39**(15): p. 3121.

139. Watson, S.W., et al., *Methods of measuring wear-corrosion synergism.* Wear, 1995. **181**: p. 476-484.

140. Williams, J.A., *Engineering tribology.* 1994: Oxford ; New York : Oxford University Press, 1994.

141.   Jemmely, P., S. Mischler, and D. Landolt, *Electrochemical modeling of passivation phenomena in tribocorrosion.* Wear, 2000. **237**(1): p. 63-76.

142.   Vargel, C., *Corrosion of aluminium. [electronic resource].* 2004: Amsterdam ; Boston : Elsevier, 2004.1st ed.

143.   Archard, J.F., *Contact and Rubbing of Flat Surfaces.* Journal of Applied Physics, 1953. **24**(8): p. 981-988.

144.   Rupert, T.J., W. Cai, and C.A. Schuh, *Abrasive wear response of nanocrystalline Ni–W alloys across the Hall–Petchbreakdown.* Wear, 2013. **298–299**: p. 120-126.

145.   Alizadeh, A., A. Abdollahi, and H. Biukani, *Creep behavior and wear resistance of Al 5083 based hybrid composites reinforced with carbon nanotubes (CNTs) and boron carbide (B 4 C).* Journal of Alloys and Compounds, 2015. **650**: p. 783-793.

146.   Yuvaraj, N. and S. Aravindan, *Fabrication of Al5083/B 4 C surface composite by friction stir processing and its tribological characterization.* Journal of materials research and technology, 2015. **4**(4): p. 398-410.

147.   Soleymani, S., A. Abdollah-Zadeh, and S. Alidokht, *Microstructural and tribological properties of Al5083 based surface hybrid composite produced by friction stir processing.* Wear, 2012. **278**: p. 41-47.

148.   Rana, R., R. Purohit, and S. Das, *Tribological behaviour of AA 5083/Micron and Nano SiC composites fabricated by ultrasonic assisted stir casting process.*

149.   Deepak, D., R.S. Sidhu, and V. Gupta, *Preparation of 5083 Al-SiC surface composite by friction stir processing and its mechanical characterization.* International Journal of Mechanical Engineering ISSN, 2013: p. 2277-7059.

150.   Gurcan, A. and T. Baker, *Wear behaviour of AA6061 aluminium alloy and its composites.* Wear, 1995. **188**(1-2): p. 185-191.

151.   Palacios, M., et al., *Influence of severe shot peening on wear behaviour of an aluminium alloy.* Fatigue & Fracture of Engineering Materials & Structures, 2014. **37**(7): p. 821-829.

152.   Mindivan, H., E.S. Kayali, and H. Cimenoglu, *Tribological behavior of squeeze cast aluminum matrix composites.* Wear, 2008. **265**(5): p. 645-654.

153.   How, H. and T. Baker, *Dry sliding wear behaviour of Saffil-reinforced AA6061 composites.* Wear, 1997. **210**(1-2): p. 263-272.

154.   Lahiri, D., et al., *Cold sprayed aluminum based glassy coating: Synthesis, wear and corrosion properties.* Surface and Coatings Technology, 2013. **232**: p. 33-40.

155.   Kumar, A.N., R. Srinivasu, and J.B. Rao, *Dry sliding wear behavior of pure Aluminium and Al-Cu alloys*, in *Advanced Tribology*. 2009, Springer. p. 422-425.

156.   Nuruzzaman, D.M. and M.A. Chowdhury, *Friction coefficient and wear rate of copper and aluminum sliding against mild steel.* International Transaction Journal of Engineering, Management, & Applied Sciences & Technologies, 2012. **4**(1): p. 29-40.

157.   Feyzullahoğlu, E. and N. Şakiroğlu, *The tribological behaviours of aluminium-based materials under dry sliding.* Industrial Lubrication and Tribology, 2011. **63**(5): p. 350-358.

158.   Venkataraman, B. and G. Sundararajan, *Correlation between the characteristics of the mechanically mixed layer and wear behaviour of aluminium, Al-7075 alloy and Al-MMCs.* Wear, 2000. **245**(1): p. 22-38.

159.   Yamanoglu, R., et al., *Effect of nickel on microstructure and wear behaviour of pure aluminium against steel and alumina counterfaces.* International Journal of Cast Metals Research, 2013. **26**(5): p. 289-295.

160. Chuang, M.-H., et al., *Microstructure and wear behavior of AlxCo 1.5 CrFeNi 1.5 Tiy high-entropy alloys.* Acta Materialia, 2011. **59**(16): p. 6308-6317.

161. Wu, J.-M., et al., *Adhesive wear behavior of Al x CoCrCuFeNi high-entropy alloys as a function of aluminum content.* Wear, 2006. **261**(5): p. 513-519.

162. Kim, Y. and R.G. Buchheit, *A characterization of the inhibiting effect of Cu on metastable pitting in dilute Al–Cu solid solution alloys.* Electrochimica Acta, 2007. **52**(7): p. 2437-2446.

163. Kim, Y., R.G. Buchheit, and P.G. Kotula, *Effect of alloyed Cu on localized corrosion susceptibility of Al–Cu solid solution alloys—Surface characterization by XPS and STEM.* Electrochimica Acta, 2010. **55**(24): p. 7367-7375.

164. Merl, D.K., P. Panjan, and I. Milošev, *Effect of tungsten content on properties of PVD sputtered Al–WX alloys.* Surface Engineering, 2013. **29**(4): p. 281-286.

165. Chuang, M.-H., et al., *Microstructure and wear behavior of AlxCo1.5CrFeNi1.5Tiy high-entropy alloys.* Acta Materialia, 2011. **59**(16): p. 6308-6317.

166. Wu, J.-M., et al., *Adhesive wear behavior of AlxCoCrCuFeNi high-entropy alloys as a function of aluminum content.* Wear, 2006. **261**(5–6): p. 513-519.

167. Lin, C.-M. and H.-L. Tsai, *Evolution of microstructure, hardness, and corrosion properties of high-entropy Al0.5CoCrFeNi alloy.* Intermetallics, 2011. **19**(3): p. 288-294.

168. Car, T., et al., *Correlation between hardness and stress in Al–(Nb, Mo, Ta) thin films.* Thin Solid Films, 2009. **517**(16): p. 4605-4609.

169. Gudić, S., I. Smoljko, and M. Kliškić, *The effect of small addition of tin and indium on the corrosion behavior of aluminium in chloride solution.* Journal of Alloys and Compounds, 2010. **505**(1): p. 54-63.

170. Reffass, M., et al., *Corrosion behaviour of magnetron-sputtered Al1−x–Mnx coatings in neutral saline solution.* Corrosion Science, 2010. **52**(11): p. 3615-3623.

171. Murdoch, H.A. and C.A. Schuh, *Estimation of grain boundary segregation enthalpy and its role in stable nanocrystalline alloy design.* Journal of Materials Research, 2013. **28**(16): p. 2154-2163.

172. Huang, T.-Y., et al., *Grain boundary segregation in Al–Mn electrodeposits prepared from ionic liquid.* Journal of Materials Science, 2015. **51**(1): p. 438-448.

173. Erdemir, A., *A crystal chemical approach to the formulation of self-lubricating nanocomposite coatings.* Surface and Coatings Technology, 2005. **200**(5–6): p. 1792-1796.

174. Murray, J.L., et al., *Stable and metastable phase equilibria in the Al-Mn system.* Metallurgical Transactions A, 1987. **18**(3): p. 385-392.

175. Oliver, W.C. and G.M. Pharr, *An improved technique for determining hardness and elastic modulus using load and displacement sensing indentation experiments.* Journal of Materials Research, 1992. **7**(06): p. 1564-1583.

176. Mischler, S., *Triboelectrochemical techniques and interpretation methods in tribocorrosion: A comparative evaluation.* Tribology International, 2008. **41**(7): p. 573-583.

177. Cai, W. and C.A. Schuh, *Microstructure and mechanical properties of electrodeposited Al1−xMnx/Al1−yMny nanostructured multilayers.* Journal of Materials Research, 2014. **29**(18): p. 2229-2239.

178. Wang, W.Y., et al., *Power law scaled hardness of Mn strengthened nanocrystalline AlMn non-equilibrium solid solutions.* Scripta Materialia, 2016. **120**: p. 31-36.

179.   Leyland, A. and A. Matthews, *Design criteria for wear-resistant nanostructured and glassy-metal coatings.* Surface and Coatings Technology, 2004. **177–178**: p. 317-324.

180.   Carranza, R.M. and J.R. Galvele, *Repassivation kinetics in stress corrosion cracking—I. Type AISI 304 stainless steel in chloride solutions.* Corrosion Science, 1988. **28**(3): p. 233-249.

181.   Akhoondan, M. and A.A. Sagüés, *Corrosion Mechanism of Aluminized Steel in Limestone Backfill.* Corrosion, 2013. **69**(12): p. 1147-1157.

182.   Li, L. and A.A. Sagüés, *Chloride Corrosion Threshold of Reinforcing Steel in Alkaline Solutions—Open-Circuit Immersion Tests.* Corrosion, 2001. **57**(1): p. 19-28.

183.   Zhang, B., Y. Li, and F. Wang, *Electrochemical corrosion behaviour of microcrystalline aluminium in acidic solutions.* Corrosion Science, 2007. **49**(5): p. 2071-2082.

184.   Martin, F.J., et al., *Impedance studies of the passive film on aluminium.* Corrosion Science, 2005. **47**(12): p. 3187-3201.

185.   de Oliveira, M.C.L., et al., *Correlation between the corrosion resistance and the semiconducting properties of the oxide film formed on AZ91D alloy after solution treatment.* Corrosion Science, 2013. **69**: p. 311-321.

186.   Jinlong, L. and L. Hongyun, *Comparison of corrosion properties of passive films formed on phase reversion induced nano/ultrafine-grained 321 stainless steel.* Applied Surface Science, 2013. **280**: p. 124-131.

187.   Bockris, J.O.M. and Y. Kang, *The protectivity of aluminum and its alloys with transition metals.* Journal of Solid State Electrochemistry, 1997. **1**(1): p. 17-35.

188.   Azumi, K., T. Ohtsuka, and N. Sato, *Mott-Schottky Plot of the Passive Film Formed on Iron in Neutral Borate and Phosphate Solutions.* Journal of The Electrochemical Society, 1987. **134**(6): p. 1352-1357.

189.   Wang, D.P., S.L. Wang, and J.Q. Wang, *Relationship between amorphous structure and corrosion behaviour in a Zr–Ni metallic glass.* Corrosion Science, 2012. **59**: p. 88-95.

190.   Chao, C.Y., L.F. Lin, and D.D. Macdonald, *A Point Defect Model for Anodic Passive Films: I . Film Growth Kinetics.* Journal of The Electrochemical Society, 1981. **128**(6): p. 1187-1194.

191.   Vieira, A.C., et al., *Mechanical and electrochemical deterioration mechanisms in the tribocorrosion of Al alloys in NaCl and in NaNO3 solutions.* Corrosion Science, 2012. **54**: p. 26-35.

192.   Ponthiaux, P., et al., *Electrochemical techniques for studying tribocorrosion processes.* Wear, 2004. **256**(5): p. 459-468.

193.   Zhang, Y., et al., *Influence of microstructure evolution on tribocorrosion of 304SS in artificial seawater.* Corrosion Science, 2014. **88**: p. 423-433.

194.   Pina, V.G., et al., *Tribocorrosion behavior of beta titanium biomedical alloys in phosphate buffer saline solution.* Journal of the Mechanical Behavior of Biomedical Materials, 2015. **46**: p. 59-68.

195.   Papageorgiou, N. and S. Mischler, *Electrochemical Simulation of the Current and Potential Response in Sliding Tribocorrosion.* Tribology Letters, 2012. **48**(3): p. 271-283.

196.   Sun, Y. and E. Haruman, *Effect of electrochemical potential on tribocorrosion behavior of low temperature plasma carburized 316L stainless steel in 1 M H2SO4 solution.* Surface and Coatings Technology, 2011. **205**(17–18): p. 4280-4290.

197.   Akonko, S.B., et al., *Effects of K3[Fe(CN)6] slurry's pH value and applied potential on tungsten removal rate for chemical–mechanical planarization application.* Wear, 2005. **259**(7–12): p. 1299-1307.

198.   Tao, S. and D.Y. Li, *Investigation of corrosion–wear synergistic attack on nanocrystalline Cu deposits.* Wear, 2007. **263**(1–6): p. 363-370.

199.   Assi, F. and H. Böhni, *Study of wear–corrosion synergy with a new microelectrochemical technique1.* Wear, 1999. **233–235**: p. 505-514.

200.   Zhang, Y., et al., *Influence of potentials on the tribocorrosion behavior of 304SS in artificial seawater.* RSC Advances, 2014. **4**(99): p. 55752-55759.

201.   Stack, M.M. and K. Chi, *Mapping sliding wear of steels in aqueous conditions.* Wear, 2003. **255**(1–6): p. 456-465.

202.   Stack, M.M. and N. Pungwiwat, *Erosion–corrosion mapping of Fe in aqueous slurries: some views on a new rationale for defining the erosion–corrosion interaction.* Wear, 2004. **256**(5): p. 565-576.

203.   Mathew, M.T., et al., *TiCxOy thin films for decorative applications: Tribocorrosion mechanisms and synergism.* Tribology International, 2008. **41**(7): p. 603-615.

204.   Jiang, J., M.M. Stack, and A. Neville, *Modelling the tribo-corrosion interaction in aqueous sliding conditions.* Tribology International, 2002. **35**(10): p. 669-679.

205.   Stemp, M., S. Mischler, and D. Landolt, *The effect of mechanical and electrochemical parameters on the tribocorrosion rate of stainless steel in sulphuric acid.* Wear, 2003. **255**(1–6): p. 466-475.

206.   Priya, R., C. Mallika, and U.K. Mudali, *Wear and tribocorrosion behaviour of 304L SS, Zr-702, Zircaloy-4 and Ti-grade2.* Wear, 2014. **310**(1–2): p. 90-100.

207.   Mischler, S., A. Spiegel, and D. Landolt, *The role of passive oxide films on the degradation of steel in tribocorrosion systems.* Wear, 1999. **225–229, Part 2**: p. 1078-1087.

208.   Mischler, S. and A.I. Muñoz, *Wear of CoCrMo alloys used in metal-on-metal hip joints: A tribocorrosion appraisal.* Wear, 2013. **297**(1–2): p. 1081-1094.

209.   Waksman, R., et al., *Safety and efficacy of bioabsorbable magnesium alloy stents in porcine coronary arteries.* Catheterization and Cardiovascular Interventions, 2006. **68**(4): p. 607-617.

210.   Jin, W., et al., *Improvement of corrosion resistance and biocompatibility of rare-earth WE43 magnesium alloy by neodymium self-ion implantation.* Corrosion Science, 2015. **94**: p. 142-155.

211.   Witte, F., et al., *In vitro and in vivo corrosion measurements of magnesium alloys.* Biomaterials, 2006. **27**(7): p. 1013-1018.

212.   Castellani, C., et al., *Bone–implant interface strength and osseointegration: Biodegradable magnesium alloy versus standard titanium control.* Acta Biomaterialia, 2011. **7**(1): p. 432-440.

213.   Weiler, A., et al., *Biodegradable Implants in Sports Medicine: The Biological Base.* Arthroscopy: The Journal of Arthroscopic & Related Surgery, 2000. **16**(3): p. 305-321.

214.   Staiger, M.P., et al., *Magnesium and its alloys as orthopedic biomaterials: A review.* Biomaterials, 2006. **27**(9): p. 1728-1734.

215.   Zhao, Y., et al., *Improved surface corrosion resistance of WE43 magnesium alloy by dual titanium and oxygen ion implantation.* Thin Solid Films, 2013. **529**: p. 407-411.

216. Jin, W., et al., *Improved corrosion resistance of Mg-Y-RE alloy coated with niobium nitride.* Thin Solid Films, 2014. **572**: p. 85-90.

217. Liu, N., et al., *Electrochemical corrosion behavior of Mg–5Al–0.4Mn–xNd in NaCl solution.* Corrosion Science, 2009. **51**(6): p. 1328-1333.

218. Zhao, Y., et al., *Enhanced antimicrobial properties, cytocompatibility, and corrosion resistance of plasma-modified biodegradable magnesium alloys.* Acta Biomaterialia, 2014. **10**(1): p. 544-556.

219. Song, G., *Control of biodegradation of biocompatable magnesium alloys.* Corrosion Science, 2007. **49**(4): p. 1696-1701.

220. Xin, Y., T. Hu, and P.K. Chu, *In vitro studies of biomedical magnesium alloys in a simulated physiological environment: A review.* Acta Biomaterialia, 2011. **7**(4): p. 1452-1459.

221. Atrens, A., M. Liu, and N.I. Zainal Abidin, *Corrosion mechanism applicable to biodegradable magnesium implants.* Materials Science and Engineering B: Solid-State Materials for Advanced Technology, 2011. **176**(20): p. 1609-1636.

222. Kirkland, N.T., G. Williams, and N. Birbilis, *Observations of the galvanostatic dissolution of pure magnesium.* Corrosion Science, 2012. **65**: p. 5-9.

223. Witte, F., et al., *In vivo corrosion of four magnesium alloys and the associated bone response.* Biomaterials, 2005. **26**(17): p. 3557-3563.

224. Zhao, Y., et al., *Improved corrosion resistance and cytocompatibility of magnesium alloy by two-stage cooling in thermal treatment.* Corrosion Science, 2012. **59**: p. 360-365.

225. Wu, G., et al., *Self-protection against corrosion of aged magnesium alloy in simulated physiological environment.* Corrosion Science, 2013. **68**: p. 279-285.

226. Liu, C., et al., *Influence of heat treatment on degradation behavior of bio-degradable die-cast AZ63 magnesium alloy in simulated body fluid.* Materials Science and Engineering: A, 2007. **456**(1–2): p. 350-357.

227. Wu, G., et al., *Effects of surface alloying on electrochemical corrosion behavior of oxygen-plasma-modified biomedical magnesium alloy.* Surface and Coatings Technology, 2012. **206**(14): p. 3186-3195.

228. Liu, C., et al., *Corrosion behavior of AZ91 magnesium alloy treated by plasma immersion ion implantation and deposition in artificial physiological fluids.* Thin Solid Films, 2007. **516**(2–4): p. 422-427.

229. Jamesh, M.I., et al., *Effects of zirconium and nitrogen plasma immersion ion implantation on the electrochemical corrosion behavior of Mg–Y–RE alloy in simulated body fluid and cell culture medium.* Corrosion Science, 2014. **86**: p. 239-251.

230. Jamesh, M., et al., *Effects of silicon plasma ion implantation on electrochemical corrosion behavior of biodegradable Mg–Y–RE Alloy.* Corrosion Science, 2013. **69**: p. 158-163.

231. Song, Y., et al., *Electrodeposition of Ca-P coatings on biodegradable Mg alloy: In vitro biomineralization behavior.* Acta Biomaterialia, 2010. **6**(5): p. 1736-1742.

232. Huang, C.A., C.K. Lin, and Y.H. Yeh, *Increasing the wear and corrosion resistance of magnesium alloy (AZ91D) with electrodeposition from eco-friendly copper- and trivalent chromium-plating baths.* Surface and Coatings Technology, 2010. **205**(1): p. 139-145.

233. Wu, G., et al., *The effect of interlayer on corrosion resistance of ceramic coating/Mg alloy substrate in simulated physiological environment.* Surface and Coatings Technology, 2012. **206**(23): p. 4892-4898.

234. Wu, G., et al., *Formation of a novel nanocrystalline coating on AZ31 magnesium alloy by bias sputtering.* Materials Letters, 2007. **61**(19–20): p. 4019-4022.

235. Dziuba, D., et al., *Long-term in vivo degradation behaviour and biocompatibility of the magnesium alloy ZEK100 for use as a biodegradable bone implant.* Acta Biomaterialia, 2013. **9**(10): p. 8548-8560.

236. Arrabal, R., et al., *Corrosion resistance of WE43 and AZ91D magnesium alloys with phosphate PEO coatings.* Corrosion Science, 2008. **50**(6): p. 1744-1752.

237. Li, M., et al., *Surface characteristics and corrosion behaviour of WE43 magnesium alloy coated by SiC film.* Applied Surface Science, 2012. **258**(7): p. 3074-3081.

238. Jin, W.H., et al., *Improvement of corrosion resistance and biocompatibility of rare-earth WE43 magnesium alloy by neodymium self-ion implantation.* Corrosion Science, 2015. **94**: p. 142-155.

239. Jin, W.H., et al., *Improved corrosion resistance of Mg-Y-RE alloy coated with niobium nitride.* Thin Solid Films, 2014. **572**: p. 85-90.

240. Zhao, Y., et al., *Improved surface corrosion resistance of WE43 magnesium alloy by dual titanium and oxygen ion implantation.* Thin Solid Films, 2013. **529**: p. 407-411.

241. Liu, P., et al., *Al2O3-ZrO2 ceramic coatings fabricated on WE43 magnesium alloy by cathodic plasma electrolytic deposition.* Materials Letters, 2012. **70**: p. 16-18.

242. Li, M., et al., *Plasma enhanced chemical vapor deposited silicon coatings on Mg alloy for biomedical application.* Surface & Coatings Technology, 2013. **228**: p. S262-S265.

243. Ye, C.H., et al., *In vitro corrosion and biocompatibility of phosphating modified WE43 magnesium alloy.* Transactions of Nonferrous Metals Society of China, 2013. **23**(4): p. 996-1001.

244. Jamesh, M.I., et al., *Effects of zirconium and nitrogen plasma immersion ion implantation on the electrochemical corrosion behavior of Mg-Y-RE alloy in simulated body fluid and cell culture medium.* Corrosion Science, 2014. **86**: p. 239-251.

245. Jiang, H.S., et al., *Microstructure and mechanical properties of WE43 magnesium alloy fabricated by direct-chill casting.* Materials Science and Engineering: A, 2017. **684**: p. 158-164.

246. Mezbahul-Islam, M., A.O. Mostafa, and M. Medraj, *Essential Magnesium Alloys Binary Phase Diagrams and Their Thermochemical Data.* Journal of Materials, 2014. **2014**: p. 33.

247. Wang, C., et al., *Improvement in grain refinement efficiency of Mg–Zr master alloy for magnesium alloy by friction stir processing.* Journal of Magnesium and Alloys, 2014. **2**(3): p. 239-244.

248. Rzychoń, T. and A. Kiełbus, *Microstructure of WE43 casting magnesium alloys.* Journal of Achievements in Materials and Manufacturing Engineering, 2007. **21**(1): p. 31-34.

249. Schlüter, K., et al., *Corrosion performance and mechanical properties of sputter-deposited MgY and MgGd alloys.* Corrosion Science, 2014. **78**: p. 43-54.

250. Blawert, C., et al., *Corrosion properties of supersaturated magnesium alloy systems*, in *Materials Science Forum* 2007. p. 1679-1684.

251. Garces, G., et al., *Texture of magnesium alloy films growth by physical vapour deposition (PVD).* Journal of Alloys and Compounds, 2000. **309**(1-2): p. 229-238.

252. Sudholz, A.D., et al., *Electrochemical behaviour and corrosion of Mg–Y alloys.* Corrosion Science, 2011. **53**(6): p. 2277-2282.

253. Bland, L.G., et al., *Assessing the Corrosion of Commercially Pure Magnesium and Commercial AZ31B by Electrochemical Impedance, Mass-Loss, Hydrogen Collection, and Inductively Coupled Plasma Optical Emission Spectrometry Solution Analysis.* Corrosion, 2015. **71**(2): p. 128-145.

254. Birbilis, N., et al., *Poisoning the corrosion of magnesium.* Electrochemistry Communications, 2013. **34**: p. 295-298.

255. Cain, T., et al., *A compilation of corrosion potentials for magnesium alloys.* Corrosion, 2014. **70**(10): p. 1043-1051.

256. Curioni, M., et al., *Correlation between electrochemical impedance measurements and corrosion rate of magnesium investigated by real-time hydrogen measurement and optical imaging.* Electrochimica Acta, 2015. **166**: p. 372-384.

257. Bland, L.G., K. Gusieva, and J.R. Scully, *Effect of Crystallographic Orientation on the Corrosion of Magnesium: Comparison of Film Forming and Bare Crystal Facets using Electrochemical Impedance and Raman Spectroscopy.* Electrochimica Acta.

258. King, A.D., N. Birbilis, and J.R. Scully, *Accurate Electrochemical Measurement of Magnesium Corrosion Rates; a Combined Impedance, Mass-Loss and Hydrogen Collection Study.* Electrochimica Acta, 2014. **121**: p. 394-406.

259. Pardo, A., et al., *Electrochemical Estimation of the Corrosion Rate of Magnesium/Aluminium Alloys.* International Journal of Corrosion, 2010. **2010**.

260. Wu, Y.J., et al., *Stifling magnesium corrosion via a novel anodic coating.* RSC Advances, 2016. **6**(49): p. 43408-43417.

261. Chu, P.W. and E.A. Marquis, *Linking the microstructure of a heat-treated WE43 Mg alloy with its corrosion behavior.* Corrosion Science, 2015. **101**: p. 94-104.

262. Fleck, N.A., V.S. Deshpande, and M.F. Ashby, *Micro-architectured materials: past, present and future.* Proceedings of the Royal Society a-Mathematical Physical and Engineering Sciences, 2010. **466**(2121): p. 2495-2516.

263. Kolodziejska, J.A., et al., *Research Update: Enabling ultra-thin lightweight structures: Microsandwich structures with microlattice cores.* Apl Materials, 2015. **3**(5).

264. Xiong, J., et al., *Advanced Micro-Lattice Materials.* Advanced Engineering Materials, 2015: p. 1-12.

265. Tian, J., et al., *The effects of topology upon fluid-flow and heat-transfer within cellular copper structures.* International Journal of Heat and Mass Transfer, 2004. **47**(14-16): p. 3171-3186.

266. Lu, T.J., L. Valdevit, and A.G. Evans, *Active cooling by metallic sandwich structures with periodic cores.* Progress in Materials Science, 2005. **50**(7): p. 789-815.

267. Roper, C.S., *Multiobjective optimization for design of multifunctional sandwich panel heat pipes with micro-architected truss cores.* International Journal of Heat and Fluid Flow, 2011. **32**(1): p. 239-248.

268. Gu, W.X. and J.R. Greer, *Ultra-strong architected Cu meso-lattices.* Extreme Mechanics Letters, 2015. **2**: p. 7-14.

269. McCormack, T.M., et al., *Failure of sandwich beams with metallic foam cores.* International Journal of Solids and Structures, 2001. **38**(28-29): p. 4901-4920.

270. Shuaeib, F.M. and P.D. Soden, *Indentation failure of composite sandwich beams.* Composites Science and Technology, 1997. **57**(9-10): p. 1249-1259.

271. Shen, Y., et al., *The Mechanical Properties of Sandwich Structures Based on Metal Lattice Architectures.* Journal of Sandwich Structures & Materials, 2010. **12**(2): p. 159-180.

272. Wadley, H.N.G., N.A. Fleck, and A.G. Evans, *Fabrication and structural performance of periodic cellular metal sandwich structures.* Composites Science and Technology, 2003. **63**(16): p. 2331-2343.

273. Yin, S., et al., *Hybrid truss concepts for carbon fiber composite pyramidal lattice structures.* Composites Part B-Engineering, 2012. **43**(4): p. 1749-1755.

274. Meza, L.R., S. Das, and J.R. Greer, *Strong, lightweight, and recoverable three-dimensional ceramic nanolattices.* Science, 2014. **345**(6202): p. 1322-1326.

275. Ruan, S.Y. and C.A. Schuh, *Electrodeposited Al-Mn alloys with microcrystalline, nanocrystalline, amorphous and nano-quasicrystalline structures.* Acta Materialia, 2009. **57**(13): p. 3810-3822.

276. Ruan, S.Y. and C.A. Schuh, *Towards electroformed nanostructured aluminum alloys with high strength and ductility.* Journal of Materials Research, 2012. **27**(12): p. 1638-1651.

277. Olson, J., et al., *Vivid, full-color aluminum plasmonic pixels.* Proceedings of the National Academy of Sciences of the United States of America, 2014. **111**(40): p. 14348-14353.

278. Cheah, S.K., et al., *Self-Supported Three-Dimensional Nanoelectrodes for Microbattery Applications.* Nano Letters, 2009. **9**(9): p. 3230-3233.

279. Oltean, G., L. Nyholm, and K. Edstrom, *Galvanostatic electrodeposition of aluminium nano-rods for Li-ion three-dimensional micro-battery current collectors.* Electrochimica Acta, 2011. **56**(9): p. 3203-3208.

280. Deshpande, V.S. and N.A. Fleck, *High strain rate compressive behaviour of aluminium alloy foams.* International Journal of Impact Engineering, 2000. **24**(3): p. 277-298.

281. Mukai, T., et al., *Experimental study of energy absorption in a close-celled aluminum foam under dynamic loading.* Scripta Materialia, 1999. **40**(8): p. 921-927.

282. Verdieck, R.G. and L.F. Yntema, *The electrochemistry of baths of fused aluminum halides I Aluminum as a reference electrode.* Journal of Physical Chemistry, 1942. **46**(3): p. 344-352.

283. Tsuda, T., C.L. Hussey, and G.R. Stafford, *Electrodeposition of Al-Mo-Mn ternary alloys from the Lewis acidic AlCl3-EtMeImCl molten salt.* Journal of the Electrochemical Society, 2005. **152**(9): p. C620-C625.

284. Su, C.J., et al., *Electrodeposition of aluminum wires from the Lewis acidic AlCl3/trimethylamine hydrochloride ionic liquid without using a template.* Electrochemistry Communications, 2013. **34**: p. 170-173.

285. Uchida, J., et al., *Electroplating of Amorphous Aluminum Manganese Alloy from Molten-Salts.* Isij International, 1993. **33**(9): p. 1029-1036.

286. Stafford, G.R. and C.L. Hussey, *Electrodeposition of Transition Metal-Aluminum Alloys from Chloroaluminate Molten Salts*, in *Advances in Electrochemical Science and Engineering*. 2001, Wiley-VCH Verlag GmbH: Weinheim. p. 313-328.

287. Boon, J.A., et al., *Friedel Crafts Reactions in Ambient-Temperature Molten-Salts.* Journal of Organic Chemistry, 1986. **51**(4): p. 480-483.

288. Li, Q.F., et al., *Electrochemical Deposition and Dissolution of Aluminum in Naalcl4 Melts - Influence of Mncl2 and Sulfide Addition.* Journal of the Electrochemical Society, 1990. **137**(9): p. 2794-2798.

289. Huo, S. and W. Schwarzacher, *Anomalous scaling of the surface width during Cu electrodeposition.* Physical Review Letters, 2001. **86**(2): p. 256-259.

290. Dammers, A.J. and S. Radelaar, *2-Dimensional Computer Modeling of Polycrystalline Film Growth.* Textures and Microstructures, 1991. **14**: p. 757-762.

291. Tian, M.L., et al., *Electrochemical growth of single-crystal metal nanowires via a two-dimensional nucleation and growth mechanism.* Nano Letters, 2003. **3**(7): p. 919-923.

292. Lewandowski, J.J., W.H. Wang, and A.L. Greer, *Intrinsic plasticity or brittleness of metallic glasses.* Philosophical Magazine Letters, 2005. **85**(2): p. 77-87.

APPENDIX A: FABRICATION AND DEFORMATION OF ALUMINUM-MANGANESE MICROSANDWICH STRUCTURE

A.1 Introduction

Micro-architectured materials including microlattices and microsandwiches have emerged recently as promising structural and functional frameworks for small-scale multifunctional devices [262-264]. Their open architecture not only leads to low areal density and high damage tolerance, but also provides channels for heat/fluid flow, which is critical to multifunctional devices such as high-capacity batteries, insect-like robots, and micro-air vehicles [265-268]. A sandwich structure exhibits higher bending rigidity than lattices by effectively redistributing the mass to the outer surfaces (instead of the core), similar to natural cellular materials found in insects and plants [262, 269]. The stiff face sheets carry bending and in-plane stresses during deformation, while the low-density core bears transverse shear stresses [270]. Such superior property has led to extensive study on the structural design of sandwiches, mostly with core size above tens of millimeters. The damage tolerance of sandwiches is highly dependent on the density, strength, and geometry of the core [271]. It was found that the periodic sandwich core can be optimized to sustain loads at much lower relative densities than stochastic foams [272]. Further improvement of mechanical properties may also be achieved by hybridizing the core material [273].

Existing fabrication procedures for large-scale sandwich structures typically involve welding or adhesive bonding of the face sheets and the core. These techniques become challenging as core size decreases to the nano- or micro-meter scale. Recently, there have been

129

several successful attempts to create microlattice and microsandwich structures from polymers [263], ceramics [274], and metals [268]. Kolodziejska et al. [263] demonstrated the synthesis of an ultra-thin lightweight polymer micosandwich by using a self-propagating photopolymer waveguide. Meza et al. [274] developed energy-absorbing ceramic microlattices with high compression ductility by combing photon lithography, atomic layer deposition, focused ion beam microscopy, and oxygen plasma etching. Recently, the same group [268] combined the template fabrication procedure with aqueous electrodeposition (ED) to produce Cu octet microlattice. Despite these progresses, the fabrication processes reported above often are complicated (involve multiple steps) or limited to specific material type [263], a simple fabrication technique for a metallic microsandwich structure still is lacking. Here, a one-step ED procedure was reported to fabricate an Al-based microsandwich structure by using a commercial polycarbonate (PC) template and two anodes simultaneously. Mn is chosen to refine the microstructure and improve the strength of Al, as demonstrated in electrodeposited Al-Mn thin films by Ruan and Schuh [275, 276]. The presented approach offers an opportunity to create Al alloy structures with low density, open architecture, high specific strength, and damage tolerance, which may find potential applications as plasmonic pixels in color displays [277], anodes for Li ion batteries [278, 279], and energy adsorbers [280, 281] etc.

A.2 Experimental Procedure

Track-etched PC membranes (Cyclopre) with an average nominal pore diameter of 5 μm were sputtered (CRC sputter coater, 99.99% argon, 5mTorr) with a thin Cu layer of ~ 250 nm thickness on both sides prior to ED. The ED experiments were performed at room temperature using a three-electrode setup inside an Ar-filled glovebox (Mbraun Labstar, $O_2 < 1$ ppm, $H_2O < 1$ ppm). Al wire (99.99%, Alfa Aesar) was used as the reference electrode. The Cu-coated PC

membrane (working electrode) was placed in the middle of two parallel Al anodes (99.99%, Alfa Aesar), allowing Al-Mn to be deposited from both ends of the pore, as illustrated in Fig. A.1. The ionic liquid electrolyte was made by mixing $AlCl_3$ (anhydrous, 99.999%, Alfa Aesar) and 1-ethyl-3-methyl-imidazolium chloride (EMIC, >98%, iolitec) in 2:1 molar ratio. As-received EMIC was dried under vacuum at 60 °C for at least 24 hours prior to mixing. The electrolyte was then purified using an Al plate under agitation until a vanish yellow color was achieved. $MnCl_2$ (98%, GFS Chemicals) was added to the electrolyte in different molarities and agitated for 24 hrs. Galvanostatic electrodeposition was performed using Gamry Reference 600 potentiostat/galvanostat at 10 mA/cm^2 for 1 hr. Finally, free-standing microsandwiches were obtained by dissolving the PC membrane using dichloromethane.

Cyclic voltammetry experiments were performed on tungsten wire (~ 1 mm diameter) working electrode at a scan rate of 20 mV/s. The deposited structures were characterized using X-ray diffraction (XRD, PANalytical X'Pert PRO), scanning electron microscopy (SEM, Hitachcai SU-70), and energy-dispersive X-ray spectroscopy (EDS, EDAX-Phoenix). Cross-sections of the microsandwiches were obtained by ion milling using focused ion beam microscopy (FIB, FEI Quanta 200). Special care was taken to minimize Ga contamination by using reduced current density during the final milling steps. Nanoindentation of the deposits was performed using a triboindenter (Hysitron, Ti900) with a diamond Berkovich tip (~125 nm radius) at 7 mN maximum load, 1.4 mN/s loading/unloading rate, and 2 s holding time. Finally, to investigate the mechanical behavior of sandwich structures exposed to localized point loads, micro-indentation (UMT-2, CETR) tests were performed using an alumina ball (4 mm diameter) tip under a constant normal load (varied from 20 to 25 N).

A.3 Results and Discussion

A.3.1 Cyclic Voltammogram

Fig. A.2 shows the typical cyclic voltammograms recored at W electrodes in 66.7–33.3 mol% AlCl3-EMIC electrolyte containing 0.05 and 0.25 M [Mn^{2+}]. The scan started from 2 V vs. Al/Al^{3+} and was reversed at – 0.5 V vs. Al/Al^{3+}. Mn is nobler than Al in an aqueous solution, but in acidic chloroaluminate electrolyte (with molar fraction of AlCl3 > 0.5), the deposition potential for Mn is slightly more negative than that for Al [282]. The forward scan in Fig. 2 is similar to that reported for pure Al [283, 284], showing no obvious reduction wave associated with [Mn^{2+}]. This indicates that Mn co-deposited with Al at potentials is lower than ∼ −0.1 V vs. Al/Al^{3+} in the ionic liquid with 0.05 M [Mn^{2+}]. The overall reduction of Al-Mn occurred by the following reactions [285]:

$$Mn^{2+} + 2e^- \leftrightarrow Mn \tag{A.1}$$

$$4Al_2Cl_7^- + 3e^- \leftrightarrow Al + 7AlCl_4^- \tag{A.2}$$
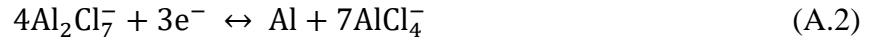
In the reverse scan, Al-Mn dissolution occurred at potentials higher than ∼ 0.3 V vs. Al/Al^{3+}. Increasing [Mn^{2+}] in the electrolyte shifted the reduction potential in the anodic direction and the dissolution potential in the cathodic direction. In addition, the current densities decreased by ∼ 40% as [Mn^{2+}] increased from 0.05 to 0.25 M. This is similar to that reported by Tsuda et al. [283], who found that the addition of [Mn^{2+}] inhibits the nucleation of Al. EDS (EDAX-Phoenix) analysis showed that increasing [Mn^{2+}] from 0.05 to 0.25 M increased the Mn concentration in the deposits from 9.0 ± 0.3 at.% to 26.2 ± 0.4 at.%. During co-deposition of Al and Mn, the alloy composition is mainly governed by the concentrations of the electroactive species $Al_2Cl_7^-$ and Mn^{2+} [286]. [$Al_2Cl_7^-$] strongly depends on the acidity of the electrolyte. Under Lewis base conditions (molar fraction of AlCl$_3$ < 0.5), [$Al_2Cl_7^-$] is close to zero (<10^{-7} M) [287].

Thus, maintaining a Lewis acid electrolyte is necessary for the deposition of Al-Mn binary alloy. It also should be noted that this condition is not necessary for Al-Mn deposition in inorganic chloroaluminate electrolyte systems where the deposition can take place involving the discharge of $AlCl^{-4}$ in a basic solution [288].

A.3.2 Microstructure of Al-Mn Microsandwich

Al-Mn microsandwiches were successfully electrodeposited from acidic $AlCl_3$-EMIC-$MnCl_2$ electrolyte containing 0.05 M [Mn^{2+}], following the procedure illustrated in Fig. A.1. Galvanostatic control was chosen to better control the size of the deposited structures. Fig. A.3.(a) shows the SEM image of the microsandwich with ~ 11 µm thick face sheets separated by 27.6 ± 0.6 µm tall pillars, which resembles the ancient Temple of Athena Nike. Fig. A.3.(b) shows the cross-section of the microsandwich prepared by FIB, where Cu coating (light contrast) and Al-Mn pillar (dark contrast) can be seen clearly. Occasionally, porosity can be found in the center of the pillars, probably due to the development of high surface roughness after the extended deposition time.

To evaluate the sandwich growth kinetics, selected ED was carried out for 3 and 10 min using one Al plate as an anode. The deposited structures were freestanding micro-tubes with various wall thicknesses. Typical SEM images of the micro-tubes are shown in Fig. A.3(c) and (d). The tubes were completely hollow, with an average height of 9.8 ± 0.9 µm. Increasing the deposition time from 3 to 10 min led to thickening of the tube wall from 670 ± 100 nm to 1.2 ± 0.4 µm without affecting the tube length. The inset in Fig. A.3(d) shows a closeup of the tube after 10 min deposition. It can be seen that the deposition advanced in the radial direction of the pore, and the inner-tube surface roughness increased with deposition time. During ED, kinetic roughening often is observed following a power law $\langle w \rangle \propto t^\beta$ [289, 290], where w represents the

surface width, i.e., the average edge length projected on the substrate, and t is the deposition time. The power exponent β typically varies from 0.2–0.5, depending on deposition parameters such as the current density and electrolyte concentration [289, 290]. Measurements of the inner-tube surfaces indicate ~ 36% increase of the surface width as the deposition time increased from 3 to 10 min, giving a power exponent β ≈ 0.25 in the present study.

XRD results of the micro-tubes and microsandwiches are presented in Fig. A.4. At 0.05 M [Mn^{2+}], the XRD pattern of the micro-tubes and microsandwich exhibited a single set of fcc peaks (lattice constant ≈ 4.00 Å) in addition to Cu (111), indicating the formation of a supersaturated solid solution of Al-Mn. This Mn concentration (9.0 at.%) is significantly higher than the equilibrium solubility of Mn in Al at room temperature (~ 0.62 at.%) [121]. For the microsandwich, a pronounced <111> fiber texture developed along the pillar direction, similar to that observed in other fcc metallic nanowires [291]. At 0.25 M [Mn^{2+}], the XRD pattern of the microsandwich indicated the formation of a complete amorphous phase (with possible local ordering [275]), as represented by the diffuse peak at 2θ ≈ 42°. These results indicate that Mn, which has a Goldschmidt radius ~ 11% smaller than Al, is substitutionally incorporated into the Al lattice. Further increasing alloy content frustrates the ordered structure and leads to the formation of amorphous phase.

A.3.3 Mechanical Properties

To evaluate the mechanical properties of the microsandwiches, nanohardness of Al-Mn was measured using Oliver–Pharr method on sandwich face sheets [175]. The maximum indentation for the crystalline (9 at.% Mn) and amorphous (26 at.% Mn) Al-Mn was ~250 and ~200 nm, respectively. The hardness of the crystalline and amorphous deposits is 2.59 ± 0.21 GPa and 6.14 ± 0.35 GPa, respectively. These values are consistent with those reported in

monolithic Al-Mn thin films electrodeposited from the same electrolyte at similar deposition current density [275, 276]. Ruan and Schuh [275] showed that Mn is highly effective in refining the microstructure of Al; increasing Mn% up to ~ 13 at.% reduces the grain size of Al by more than three orders of magnitude. Thus the high hardness of Al-Mn is likely the combined effects of Hall-Petch and solid solution strengthening. Given the low density of Al alloys ($\rho_{Al-9Mn} \approx 3.12$ g/cm^3 and $\rho_{Al-26Mn} \approx 3.94$ g/cm^3) and the open architecture (relative density $\bar{\rho} = \rho_{sandwich}/\rho_{solid} = 0.48$), the density of the microsandwiches is estimated to be ~ 1.50 g/cm^3 and 1.89 g/cm^3 for the crystalline and amorphous structure, respectively. The estimated specific strength of the sandwiches are between 277 and 520 kN•m/kg, well in excess of Al alloys used in commercial Al foams [269]. The relative density of the deposit can be tailored by adjusting the geometry of the membrane (e.g. pore density, pore diameter, membrane thickness) or controlling the deposition time (to form hollow instead of solid cores). For commercial PC membrane with void volume ranges between 4 and 20%, a relative density in the range of ~ 20% - 50% can be potentially achieved using the current method.

While sandwiches are efficient lightweight structures with high bending rigidity, they are notoriously sensitive to failure by the application of localized external loading [270]. To evaluate their resistance to quasi-static impact, the crystalline and amorphous microsandwiches (ca. 1×1 cm^2) were indented by a 4 mm diameter alumina ball under 20 to 25 N normal load. A top face crack started to develop in the crystalline microsandwich at loads larger than ~ 22 N. On the other hand, large-scale cracks were observed on the top face of the amorphous microsandwiches under all loads investigated. Fig. A.5(a)–(d) show typical SEM images of the surface of the microsandwiches indented at 21 and 22 N. The failure modes were similar to those reported for macroscale sandwich structures [270]. The crystalline microsandwich mainly failed by pillar

(core) compression (Fig. A.5(e)), with minimal deformation of the upper face (skin). The height of the deformed pillars beneath the indent was ~ 8.3 ± 0.5 μm, corresponding to a local compressive strain of ~ 70%. An arc-shaped crack was developed near the edge of the contact area under 22 N (Fig. A.5(c)), characteristic of ductile intergranular fracture. The failure mode of the amorphous microsandwich (FIG. A.5(b) and (d)) was mainly the brittle fracture and collapse of the upper face, whereas the pillars underneath retained their original shape (FIG. A.5(f)). Debonding between the top faces and the core was observed in both samples.

During indentation of a sandwich structure, the core yield load (P_1) can be estimated as [270]:

$$P_1 = 1.52\sigma_c bt(\frac{E_c}{E_f}\frac{c}{t})^{1/4} \tag{A.3}$$

where the core yield strength (σ_c, listed in Table 1) is calculated from nanoindentation hardness assuming a Tabor factor of 3, the skin thickness t is 11 μm, sample width b is 1 mm, core thickness c is 27.6 μm, and the core to face elastic modulus ratio $\frac{E_c}{E_f} \approx 1$. The load for the top skin fracture (P_2) and the plastic zone size (2s, as defined in Fig. 3 in [270]) can be solved numerically from equations (2) and (3) [270]:

$$\left(\frac{3\lambda}{2\sigma_c b}\right)P_2 = \frac{2z^3(\sinh^2 z' + \sin^2 z') + 3(\sinh z' \cosh z' - \sin z' \cos z')(2z^2 - 1) - 6z}{z^2(\sinh^2 z' + \sin^2 z') + 2z(\sinh z' \cosh z' - \sin z' \cos z') - (\cosh^2 z' + \cos^2 z')} \tag{A.4}$$

and

$$\left(\frac{\lambda}{\sigma_c b}\right)P_2 = \frac{\frac{\lambda^2 t^2 \sigma_f}{3\sigma_c} + z^2 + 2zA + B}{z + A} \tag{A.5}$$

where $z = \lambda s$, $z' = \lambda s'$, $\lambda = (\frac{3E_f}{E_c c t^3})^{1/4}$, $A = \frac{\sinh z' \cosh z' - \sin z' \cos z'}{\sinh^2 z' + \sin^2 z'}$ and $B = \frac{\sinh^2 z' - \sin^2 z'}{\sinh^2 z' + \sin^2 z'}$. The calculated results are listed in Table 1. For the crystalline microsandwich, the predicted skin fracture load is 23.4 N, very close to the crack initiation load measured experimentally (~ 22 N).

This load is also larger than the core yield load (18.2 N). Thus, extensive core compression occurred prior to surface crack formation. In addition, the predicted plastic zone size (300 μm) agrees well with the experimentally-measured fracture size (dashed arc in Fig. A.5(c)). For the amorphous microsandwich, the predicted core yield load (43.1 N) is much higher than the applied loads. Thus, no core compression was expected in this case. On the other hand, the brittle fracture of the top face, despite a high skin fracture load (55.6 N), is likely related to the near-zero tensile ductility of amorphous metals, which lacks sufficient intrinsic micromechanisms to mitigate high stress concentrations at crack tips [292].

To gain further understanding of the failure mechanism of the microsandwiches, finite element analysis (FEA) was performed using Ansys Workbench over an area of 70×70 μm^2 with pillars separated 10 μm apart. The dimensions of the microsandwich were taken from experimental measurements. Both Al-9 at.% Mn and Al-26 at.% Mn were assumed to be elastic-perfectly plastic (due to the lack of reliable stress-strain data) with material properties listed in Table 1. The sandwiches were loaded at 0.81 N and subsequently unloaded to reproduce the experimentally-measured displacement. The FEA results are shown in Fig. A.6. Under the same load, the crystalline sandwiches were plastically deformed with large displacement (Fig. 6(a)), while the amorphous one experienced only elastic deformation (mainly on top face, as shown in Fig. A.6(b)). In both structures, the maximum equivalent stress and the critical shear strains always appear near the face-core interface, in agreement with the pillar delamination location observed experimentally. Finally, the absorption energy per unit volume of the crystalline microsandwich is estimated to be ~ 43.2 MJ/m^3, much higher than that of conventional aluminum foams and new lattice structures under similar strain (e.g. ~ 1−4 MJ/m^3 for ALPORAS

[281], ~ 12 MJ/m^3 for aluminum honeycomb foam [133], and 1 - 20 MJ/m^3 for stainless steel square and diamond lattice [133, 275]).

A.4 Conclusions

In summary, Al-Mn microsandwiches with nominal core pillar size of 5 μm were successfully electrodeposited using a PC template from acidic chloroaluminate electrolyte containing 0.05 and 0.25 M [Mn^{2+}]. The crystallinity and mechanical properties of the deposits can be tuned by controlling [Mn^{2+}] in the electrolyte. Microsandwiches were found to grow along the radial direction of the template pore with tunable wall thickness by the deposition time. Alloying with Mn significantly increased the strength and damage tolerance of the microsandwich. Given the flexibility and scalability of the ED process, the methods demonstrated here present an interesting future direction for designing ultra-lightweight energy adsorbers with open architecture, high strength, and damage resistance.

A.5 References

1.   Fleck, N.A., V.S. Deshpande, and M.F. Ashby, *Micro-architectured materials: past, present and future.* P Roy Soc a-Math Phy, 2010. **466**(2121): p. 2495-2516.
2.   Kolodziejska, J.A., C.S. Roper, S.S. Yang, W.B. Carter, and A.J. Jacobsen, *Research Update: Enabling ultra-thin lightweight structures: Microsandwich structures with microlattice cores.* Apl Mater, 2015. **3**(5).
3.   Xiong, J., R. Mines, R. Ghosh, A. Vaziri, L. Ma, A. Ohrndorf, H. Christ, and L. Wu, *Advanced Micro-Lattice Materials.* Advanced Engineering Materials, 2015: p. 1-12.
4.   Tian, J., T. Kim, T.J. Lu, H.P. Hodson, D.T. Queheillalt, D.J. Sypeck, and H.N.G. Wadley, *The effects of topology upon fluid-flow and heat-transfer within cellular copper structures.* Int J Heat Mass Tran, 2004. **47**(14-16): p. 3171-3186.
5.   Lu, T.J., L. Valdevit, and A.G. Evans, *Active cooling by metallic sandwich structures with periodic cores.* Prog Mater Sci, 2005. **50**(7): p. 789-815.
6.   Roper, C.S., *Multiobjective optimization for design of multifunctional sandwich panel heat pipes with micro-architected truss cores.* Int J Heat Fluid Fl, 2011. **32**(1): p. 239-248.
7.   Gu, W.X. and J.R. Greer, *Ultra-strong architected Cu meso-lattices.* Extreme Mechanics Letters, 2015. **2**: p. 7-14.
8.   McCormack, T.M., R. Miller, O. Kesler, and L.J. Gibson, *Failure of sandwich beams with metallic foam cores.* Int J Solids Struct, 2001. **38**(28-29): p. 4901-4920.

9.   Shuaeib, F.M. and P.D. Soden, *Indentation failure of composite sandwich beams.* Compos Sci Technol, 1997. **57**(9-10): p. 1249-1259.

10.   Shen, Y., S. McKown, S. Tsopanos, C.J. Sutcliffe, R.A.W. Mines, and W.J. Cantwell, *The Mechanical Properties of Sandwich Structures Based on Metal Lattice Architectures.* J Sandw Struct Mater, 2010. **12**(2): p. 159-180.

11.   Wadley, H.N.G., N.A. Fleck, and A.G. Evans, *Fabrication and structural performance of periodic cellular metal sandwich structures.* Compos Sci Technol, 2003. **63**(16): p. 2331-2343.

12.   Yin, S., L.Z. Wu, L. Ma, and S. Nutt, *Hybrid truss concepts for carbon fiber composite pyramidal lattice structures.* Compos Part B-Eng, 2012. **43**(4): p. 1749-1755.

13.   Meza, L.R., S. Das, and J.R. Greer, *Strong, lightweight, and recoverable three-dimensional ceramic nanolattices.* Science, 2014. **345**(6202): p. 1322-1326.

14.   Ruan, S.Y. and C.A. Schuh, *Electrodeposited Al-Mn alloys with microcrystalline, nanocrystalline, amorphous and nano-quasicrystalline structures.* Acta Mater, 2009. **57**(13): p. 3810-3822.

15.   Ruan, S.Y. and C.A. Schuh, *Towards electroformed nanostructured aluminum alloys with high strength and ductility.* J Mater Res, 2012. **27**(12): p. 1638-1651.

16.   Olson, J., A. Manjavacas, L. Liu, W. Chang, B. Foerster, N.S. King, M.W. Knight, P. Nordlander, N.J. Halas, and S. Link, *Vivid, full-color aluminum plasmonic pixels.* P Natl Acad Sci USA, 2014. **111**(40): p. 14348-14353.

17.   Cheah, S.K., E. Perre, M. Rooth, M. Fondell, A. Harsta, L. Nyholm, M. Boman, T. Gustafsson, J. Lu, P. Simon, and K. Edstrom, *Self-Supported Three-Dimensional Nanoelectrodes for Microbattery Applications.* Nano Lett, 2009. **9**(9): p. 3230-3233.

18.   Oltean, G., L. Nyholm, and K. Edstrom, *Galvanostatic electrodeposition of aluminium nano-rods for Li-ion three-dimensional micro-battery current collectors.* Electrochim Acta, 2011. **56**(9): p. 3203-3208.

19.   Deshpande, V.S. and N.A. Fleck, *High strain rate compressive behaviour of aluminium alloy foams.* Int J Impact Eng, 2000. **24**(3): p. 277-298.

20.   Mukai, T., H. Kanahashi, T. Miyoshi, M. Mabuchi, T.G. Nieh, and K. Higashi, *Experimental study of energy absorption in a close-celled aluminum foam under dynamic loading.* Scripta Mater, 1999. **40**(8): p. 921-927.

21.   Verdieck, R.G. and L.F. Yntema, *The electrochemistry of baths of fused aluminum halides I Aluminum as a reference electrode.* J Phys Chem-Us, 1942. **46**(3): p. 344-352.

22.   Tsuda, T., C.L. Hussey, and G.R. Stafford, *Electrodeposition of Al-Mo-Mn ternary alloys from the Lewis acidic AlCl3-EtMeImCl molten salt.* J Electrochem Soc, 2005. **152**(9): p. C620-C625.

23.   Su, C.J., Y.T. Hsieh, C.C. Chen, and I.W. Sun, *Electrodeposition of aluminum wires from the Lewis acidic AlCl3/trimethylamine hydrochloride ionic liquid without using a template.* Electrochem Commun, 2013. **34**: p. 170-173.

24.   Uchida, J., T. Tsuda, Y. Yamamoto, H. Seto, M. Abe, and A. Shibuya, *Electroplating of Amorphous Aluminum Manganese Alloy from Molten-Salts.* Isij Int, 1993. **33**(9): p. 1029-1036.

25.   Stafford, G.R. and C.L. Hussey, *Electrodeposition of Transition Metal-Aluminum Alloys from Chloroaluminate Molten Salts*, in *Advances in Electrochemical Science and Engineering*. 2001, Wiley-VCH Verlag GmbH: Weinheim. p. 313-328.

26. Boon, J.A., J.A. Levisky, J.L. Pflug, and J.S. Wilkes, *Friedel Crafts Reactions in Ambient-Temperature Molten-Salts.* J Org Chem, 1986. **51**(4): p. 480-483.

27. Li, Q.F., H.A. Hjuler, R.W. Berg, and N.J. Bjerrum, *Electrochemical Deposition and Dissolution of Aluminum in Naalcl4 Melts - Influence of Mncl2 and Sulfide Addition.* J Electrochem Soc, 1990. **137**(9): p. 2794-2798.

28. Huo, S. and W. Schwarzacher, *Anomalous scaling of the surface width during Cu electrodeposition.* Phys Rev Lett, 2001. **86**(2): p. 256-259.

29. Dammers, A.J. and S. Radelaar, *2-Dimensional Computer Modeling of Polycrystalline Film Growth.* Texture Microstruct, 1991. **14**: p. 757-762.

30. Liu, X.J., I. Ohnuma, R. Kainuma, and K. Ishida, *Thermodynamic assessment of the aluminum-manganese (Al-Mn) binary phase diagram.* J Phase Equilib, 1999. **20**(1): p. 45-56.

31. Tian, M.L., J.U. Wang, J. Kurtz, T.E. Mallouk, and M.H.W. Chan, *Electrochemical growth of single-crystal metal nanowires via a two-dimensional nucleation and growth mechanism.* Nano Lett, 2003. **3**(7): p. 919-923.

32. Oliver, W.C. and G.M. Pharr, *An improved technique for determining hardness and elastic modulus using load and displacement sensing indentation experiments.* Journal of Materials Research, 1992. **7**(06): p. 1564-1583.

33. Lewandowski, J.J., W.H. Wang, and A.L. Greer, *Intrinsic plasticity or brittleness of metallic glasses.* Phil Mag Lett, 2005. **85**(2): p. 77-87.

34. Ruan, S.Y., K.L. Torres, G.B. Thompson, and C.A. Schuh, *Gallium-enhanced phase contrast in atom probe tomography of nanocrystalline and amorphous Al-Mn alloys.* Ultramicroscopy, 2011. **111**(8): p. 1062-1072.

35. Cardarelli, F., *Materials Handbook: A Concise Desktop Reference*. 2nd edition ed. 2008, London: Springer-Verlag.

Table A.1 Summary of composition and properties of microsandwiches. Elastic constants were estimated from rule of mixture [143]. Plastic zone size, core yield and skin fracture loads were calculated from eqns. (A.3)-(A.5).

Microsandwich composition	Elastic modulus (GPa)	Poisson's ratio	Yield strength (MPa)	Plastic zone size (μm)	Core yield load (N)	Skin fracture load (N)
Al-9 at.%Mn	81.1	0.34	863	300	18.2	23.4
Al-26 at.%Mn	101.6	0.32	2,050	300	43.1	55.6
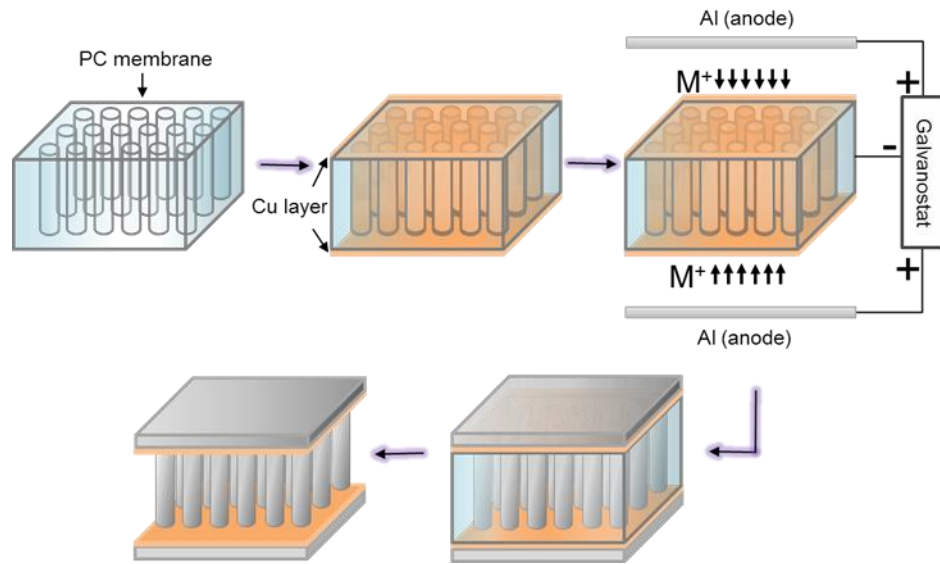
Figure A.1 Schematic illustration of electrodeposition procedures for microsandwiches.
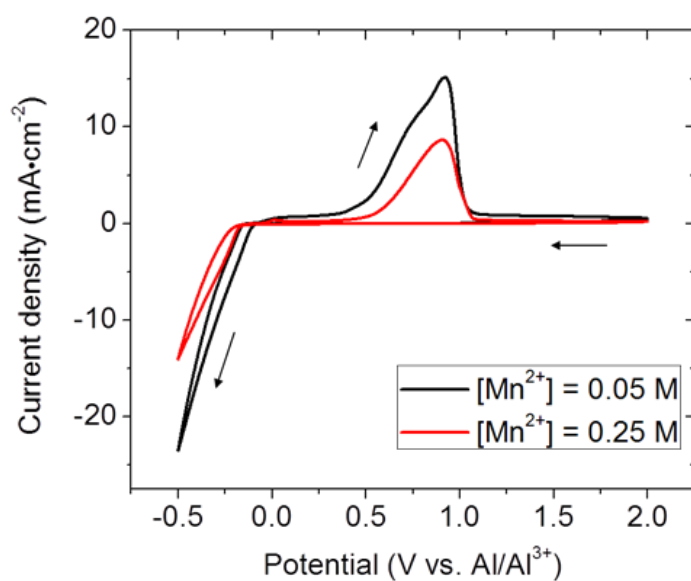
Figure A.2 Cyclic voltammograms recorded in AlCl$_3$-EMIC electrolyte containing 0.05 and 0.25 M [Mn^{2+}].
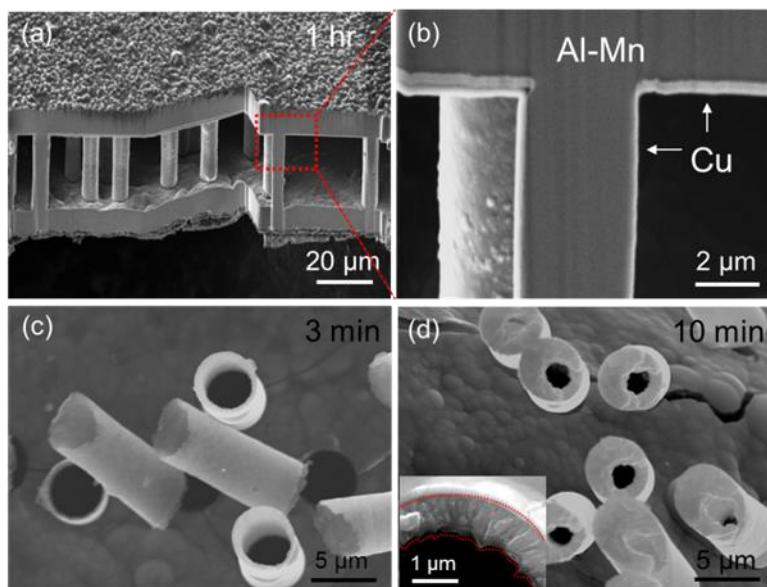
Figure A.3 SEM images of (a)–(b) microsandwich, (c)–(d) micro-tubes deposited from acidic AlCl$_3$-EMIC electrolyte containing 0.05 M [Mn^{2+}].
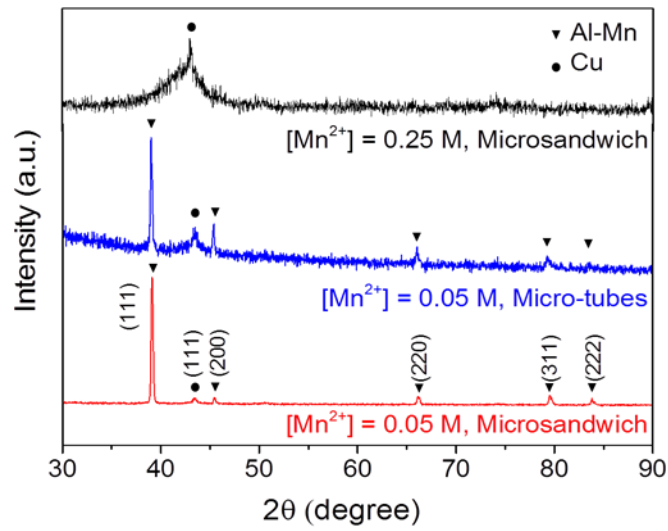
Figure A.4 XRD 2θ scans of micro-tubes and microsandwiches
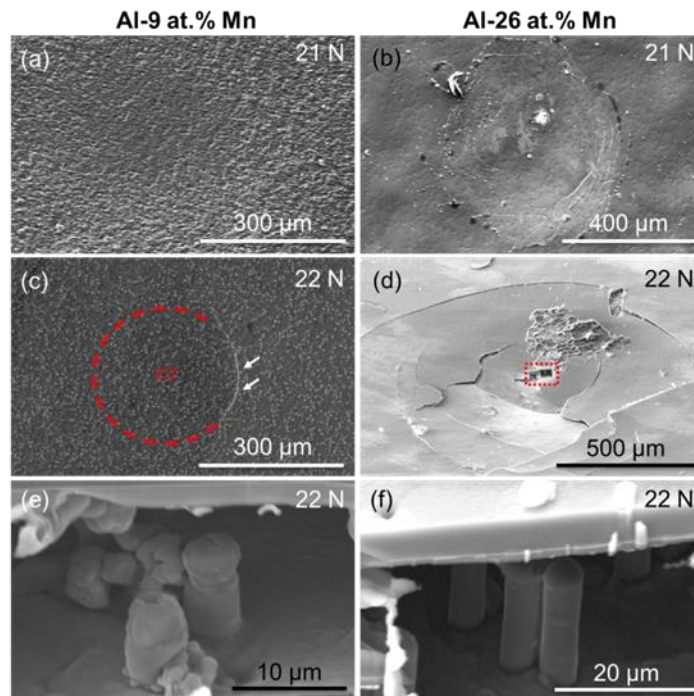
Figure A.5 SEM images of (a)-(b) surface and (c)-(d) cross-section of Al-9 at.% Mn and Al-26 at.% Mn microsandwiches after micro-indentation. Images (e) and (f) are taken from the box areas in (c) and (d), respectively
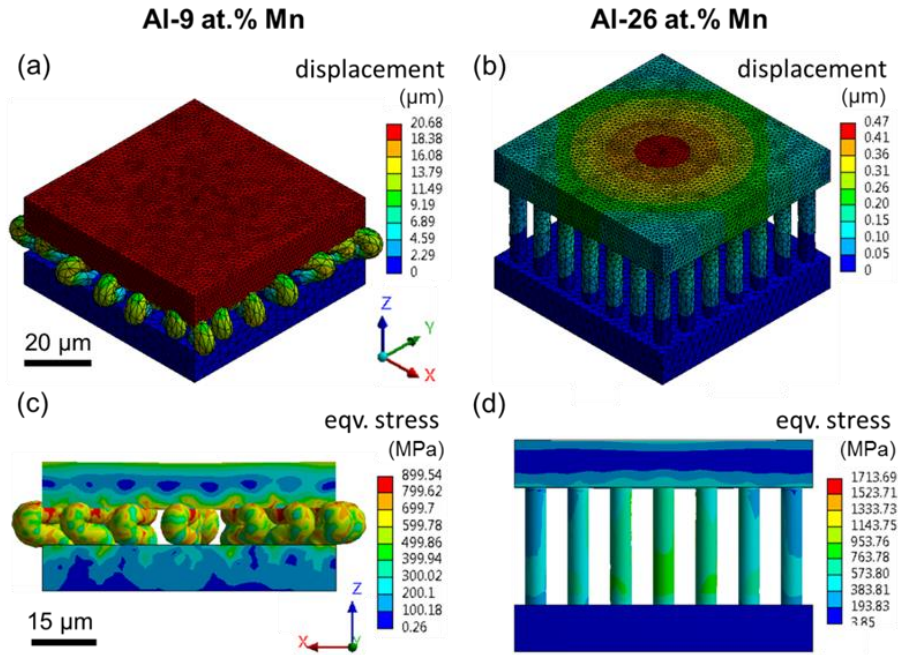
Figure A.6 FEA predicted (a)-(b) displacement, and (c)-(d) equivalent stress of Al-9 at.% Mn and Al-26 at.% Mn microsandwiches after micro-indentation

APPENDIX B: COPYRIGHT PERMISSIONS

The permission to use published articles of chapter 3 is shown below.

The permission to use published articles of Appendix A is shown below.

The copyright permission for figure 2.13 is shown below.